

3D Reconstruction of Plant Roots from MRI Images to Advance Root-Soil Systems Modelling

Dissertation

zur Erlangung des Grades

Doktor der Agrarwissenschaften (Dr. agr.)

der Landwirtschaftlichen Fakultät
der Rheinischen Friedrich-Wilhelms-Universität Bonn

von

Tobias Selzner

aus Siegburg

Bonn 2024

Referent: Prof. Dr. Andrea Schnepf

Korreferent: Prof. Dr. Wulf Amelung

Tag der mündlichen Prüfung: 01.07.2024

Angefertigt mit Genehmigung der Landwirtschaftlichen Fakultät der Universität Bonn

Abstract

Background and Motivation: Roots are of particular interest for the efficient use of nutrients and water by plants. Therefore, the optimization of root system architecture (RSA) offers large potential in finding more sustainable agricultural practices. Magnetic resonance imaging (MRI) is one of the few phenotyping methods that allows us to observe the 3D RSA in opaque soil. Such volumetric data are essential to investigate favorable RSA traits with functional-structural root architecture models (FSRMs). However, the processing of MRI images and their integration into FSRMs is challenging and limits the use of the data to this day. In this work, we investigated how MRI images of plant roots and related experimental data can be processed more efficiently, and how their meaningful use in FSRMs can be optimized.

Material and Methods: To alleviate the bottleneck in MRI image processing, we deployed a novel approach for automated root system reconstruction. The approach combines a semantic segmentation of raw MRI images into roots and soil with a root reconstruction algorithm. We evaluated the results by comparing them with state-of-the-art manual expert reconstructions. In the next step, we investigated if the current soil process descriptions in FSRMs are adequate to derive realistic root water uptake (RWU) predictions for RSAs derived from MRI images. We performed a soil grid convergence study of our default modelling approach in CPlantBox and implemented an alternative approach for RWU calculation. The results were evaluated by comparing them to a numerical reference solution. Finally, we explored new methods for the virtual replication of MRI experiments in FSRMs. We devised a novel parameterization method for mimicking root growth based on MRI time series. By combining the measured root growth with additional experimental data, we performed a virtual repetition of an MRI experiment.

Results: We observed that the U-Net segmentation improved reconstruction performance in manual and automated workflows of root system reconstruction and allowed us to process MRI images more efficiently. Furthermore, the segmentation enabled the application of the automated reconstruction algorithm for MRI images with a low contrast-to-noise ratio. The soil grid convergency study highlighted that root system scale models are not able to spatially resolve the steep soil water potential gradients near plant roots during water uptake. This

resulted in large errors in simulated RWU for dry soil conditions. The implemented alternative approach for RWU calculation showed the best agreement with the reference solution, while the computational cost was kept low. Mimicking root growth based on MRI time-series data with the novel parameterization method allowed us to derive time-dependent root system metrics and to create a functional representation of growing root systems. By combining this functional representation of growing root systems with additional experimental data, we have created a parameterization framework that allows a data-driven replication of the observed RWU in CPlantBox.

Conclusions: We were able to improve several aspects of the 3D reconstruction of plant roots from MRI images and their integration into root-soil-system models. The improvements to manual and automated workflows for RSA reconstruction will facilitate the parameterization of RSA submodels with MRI data. In addition, the ability to derive RSAs from low CNR images broadens the general scope of MRI experiments. The grid convergence study raised awareness for errors related to current RWU modelling paradigms under drought conditions. Using the alternative approach for RWU calculation makes it possible to bring the level of detail of FSRMs closer to that of MRI-based RSAs. The novel parameterization method for virtual replication of MRI experiments facilitates the parameterization of RSA submodels based on time-dependent root system metrics. Furthermore, the parameterization method refines our ability to validate the mechanisms and assumptions underlying RWU in FSRMs.

Zusammenfassung

Hintergrund und Motivation: Wurzeln sind für die effiziente Nutzung von Nährstoffen und Wasser durch Pflanzen von besonderem Interesse. Die Optimierung der Wurzelsystemarchitektur (engl.: root system architecture, RSA) bietet daher großes Potenzial für die Entwicklung nachhaltigerer landwirtschaftlicher Praktiken. Magnetresonanztomographie (engl.: magnetic resonance imaging, MRI) ist eine der wenigen Phänotypisierungsmethoden mit der wir die 3D RSA in opaken Böden beobachten können. Solche volumetrischen Daten sind unerlässlich, um vorteilhafte Eigenschaften der RSA mit funktionell-strukturellen Wurzelarchitekturmodellen (engl.: functional-structural root architecture models, FSRMs) zu untersuchen. Die Verarbeitung von MRI-Bildern und deren Integration in FSRMs ist jedoch herausfordernd und schränkt die Nutzung der Daten bisher ein. In dieser Arbeit haben wir untersucht, wie MRI-Bilder von Wurzeln und zugehörige experimentellen Daten effizienter verarbeitet, und sinnvoller in FSRMs integriert werden können.

Material und Methoden: Um den Engpass bei der Verarbeitung von MRI-Bildern zu beseitigen, haben wir einen neuartigen Ansatz zur automatischen Rekonstruktion von Wurzelsystemen angewandt. Der Ansatz kombiniert eine semantische Segmentierung von MRI-Rohdaten in Wurzeln und Boden mit einem Algorithmus zur Wurzelrekonstruktion. Wir bewerteten die Ergebnisse mittels Vergleiches zu manuellen Expertenrekonstruktionen. Darüber hinaus haben wir untersucht, ob die derzeitigen Beschreibungen der Bodenprozesse in FSRMs ausreichend sind, um realistische Vorhersagen der Wurzelwasseraufnahme (engl.: root water uptake, RWU) für MRI-basierte RSAs zu treffen. Wir haben eine Bodengitterkonvergenzstudie unseres Standardmodellierungsansatzes in CPlantBox durchgeführt und implementierten einen alternativen Ansatz für die RWU-Berechnung. Die Ergebnisse wurden durch den Vergleich mit einer numerischen Referenzlösung bewertet. Schließlich untersuchten wir neue Methoden für die virtuelle Replikation von MRI-Experimenten in FSRMs. Wir entwickelten eine neue Parametrisierungsmethode für die Nachahmung von Wurzelwachstum auf Grundlage von MRI-Zeitreihen. Indem wir das gemessene Wurzelwachstum mit anderen

experimentellen Daten kombinierten, führten wir eine virtuelle Wiederholung eines MRI-Experiments durch.

Ergebnisse: Wir stellten fest, dass die U-Net-Segmentierung die Rekonstruktionsleistung von manuellen und automatisierten Arbeitsabläufen der Wurzelsystemrekonstruktion verbesserte und es uns ermöglichte, MRI-Bilder effizienter zu verarbeiten. Darüber hinaus ermöglichte die Segmentierung die Anwendung des automatisierten Rekonstruktionsalgorithmus bei MRI-Bildern mit geringen Kontrast-zu-Rausch-Verhältnissen (engl.: contrast-to-noise ratios, CNRs). Die Bodengitterkonvergenzstudie zeigte, dass Modelle auf der Wurzelsystemskala nicht in der Lage sind, die steilen Gradienten des Bodenwasserpotenzials in der Nähe der Pflanzenwurzeln räumlich aufzulösen. Dies führte zu großen Fehlern der simulierten RWU bei trockenen Bodenbedingungen. Der alternative Ansatz für die RWU-Berechnung zeigte die beste Übereinstimmung mit der Referenzlösung, während die Rechenkosten niedrig gehalten werden konnten. Die Nachahmung des Wurzelwachstums, auf Grundlage von MRI-Zeitreihen, ermöglichte es uns zeitabhängige Wurzelmetriken und eine funktionale Beschreibung wachsender Wurzelsysteme abzuleiten. Durch die Kombination dieser funktionalen Beschreibung wachsender Wurzelsysteme mit weiteren experimentellen Daten, haben wir einen Parametrisierungsrahmen geschaffen, der eine datengesteuerte Replikation der beobachteten RWU in CPlantBox ermöglicht.

Schlussfolgerungen: Wir konnten mehrere Aspekte der 3D-Rekonstruktion von Pflanzenwurzeln aus MRI-Bildern, und deren Integration in Wurzel-Boden-System-Modelle verbessern. Die Verbesserungen der manuellen und automatisierten Arbeitsabläufe, für die RSA-Rekonstruktion, werden die Parametrisierung von RSA-Submodellen mit MRI-Daten erleichtern. Darüber hinaus erweitert die Möglichkeit, RSAs aus Bildern mit niedrigem CNR abzuleiten, den allgemeinen Anwendungsbereich von MRI-Experimenten. Die Studie zur Gitterkonvergenz hat das Bewusstsein für Fehler im Zusammenhang mit den derzeitigen RWU-Modellierungsparadigmen unter Trockenheitsbedingungen geschärft. Die Verwendung des alternativen Ansatzes für die RWU-Berechnung ermöglicht es, den Detaillierungsgrad von FSRMs näher an den von MRI-basierten RSAs heranzuführen. Die neue Parametrisierungsmethode zur virtuellen Replikation von MRI-Experimenten erleichtert die Parametrisierung von RSA-Submodellen auf Grundlage von zeitabhängigen

Wurzelsystemmetriken. Darüber hinaus verbessert die Parametrisierungsmethode unsere Fähigkeit, die Mechanismen und Annahmen zu validieren, die der RWU in FSRMs zugrunde liegen.

Table of Contents

Abstract	I
Zusammenfassung	III
Table of Contents	VI
List of Figures	IX
List of Tables	XIV
List of Abbreviations	XVI
1 General Introduction	1
1.1 Optimization of Root System Architecture - an Untapped Potential	4
1.2 Measuring the Hidden Half – Methods of Root System Phenotyping	5
1.3 Volumetric Image Segmentation – the Virtual Excavation of the Root System	6
1.4 Root System Reconstruction – from Segmented Images to Root System Architecture	7
1.5 The Effect of Root Hydraulic Architecture on Root Water Uptake from Soil	9
1.6 Unravelling Root Water Uptake with Functional-Structural-Plant Models	12
1.7 Aims and Objectives	16
1.8 Thesis Outline	17
2 3D U-Net Segmentation Improves Root System Reconstruction from 3D MRI Images in Automated and Manual Virtual Reality Workflows	19
2.1 Introduction	20
2.2 Material and Methods	24

2.2.1	Experimental Design	24
2.2.2	MRI Measurements	25
2.2.3	Root Reconstruction Methods	26
2.2.3.1	Two-step Workflow for MRI Image Segmentation and Root Tracing	26
2.2.3.2	Manual Tracing in Virtual Reality	29
2.2.4	Measures to Determine Success	31
2.2.4.1	Visual Comparison of Tracings	31
2.2.4.2	Quantitative Measures	32
2.2.4.3	Statistical Analysis	33
2.3	Results	35
2.3.1	Visual Comparison of Tracings	35
2.3.2	Quantitative Measures	39
2.4	Discussion	42
2.5	Conclusions	48
3	Root System Scale Models Significantly Overestimate Root Water Uptake at Drying Soil Conditions	50
3.1	Introduction	51
3.2	Material and Methods	52
3.2.1	Benchmark Scenario C1.2	52
3.2.2	Model Description	53
3.2.3	Impact of Grid Size	54
3.3	Results	55
3.4	Discussion	57
4	Parameterizing In-silico Replications of MRI Experiments	61
4.1	Introduction	62
4.2	MRI Experiment and Gathered Data	63

4.3 Model Parameterization	70
4.4 Model Outputs	78
5 Conclusions and Outlook	84
5.1 Conclusions	85
5.2 Outlook	87
Appendix A	90
Appendix B	104
Appendix C	108
Acknowledgements	109
Bibliography	110

List of Figures

Fig. 2.1: Maximum intensity projection of a MRI scan of a 14-day old lupine root system grown in sand after dewarping and stitching (resolution $0.27 \times 0.27 \times 1 \text{ mm}^3$)..... 26

Fig. 2.2: Exemplary visualization of data used for training the U-Net. (a): rendering of manual reconstruction, (b): virtual soil data, (c): synthetic root system, (d): real slice of pure MRI soil. 27

Fig. 2.3: Largest-connected-component extraction with gap closing. (a): segmented input in intensity, (b): voxel cost, (c): adapted cost-map for gap closing, (d): extracted largest-connected component. © [2021] IEEE. Reprinted from Horn et al. (2021). 28

Fig. 2.4: Manual root system reconstruction workflows based on images from the VR application. Shown are the marching cubes isosurfaces of an MRI scan at different signal thresholds (gray) and manual tracings with color-coded root orders at different reconstruction stages. (a): raw image of MRI scan as displayed in VR, (b): threshold adjustment for improved visibility of roots, drawing and adjusting the radius of the first tap root segment, (c): reconstructing the tap root while creating nodes at potential branching points, (d): reconstruction of laterals from bottom to top, (e): finalized manual tracing, (f): U-Net segmentation in VR. Workflow M is based on (a), M+ and A are based on segmented images (f)..... 30

Fig. 2.5: Manual tracings M (left), manual tracings after segmentation M+ (middle) and automated tracings A (right) of four *Lupinus albus* root systems (a-d) grown in sand derived by MRI scans. Reconstructions are cropped to show areas of interest. Colors display root orders, root segments are scaled by their respective radius. Age of the root systems is between 8 and 14 days (see Table 2.1)..... 36

Fig. 2.6: Manual tracings M (left), manual tracings after segmentation M+ (middle) and automated tracings A (right) of four *Lupinus albus* root systems (a-d) grown in soil derived by MRI scans. Reconstructions are cropped to show areas of interest. Colors display root orders,

root segments are scaled by their respective radius. Age of the root systems is between 8 and 15 days (see Table 2.1)..... 37

Fig. 3.1: (a): Cumulative transpiration of the numerical reference solution (dotted), the multi-scale model (dashed), and the root system scale (RSS) model at different soil resolutions (solid) for the loamy soil scenario benchmark C1.2 at initial $\psi_{s,top} = -659.8$ cm. Values in parentheses indicate the relative error (RE), numbers above lines indicate the wall-clock time required to compute the respective simulation. (b): Equivalent soil water potential, $\psi_{s,eq}$, (dashed) for the reference solution (black), and for RSS (blue), and multi-scale model (red) while using a bulk soil resolution of 1 cm. Blue and red solid lines show the mean bulk soil water potential, $\psi_{s,bulk}$, of the soil domain in RSS and multi-scale model, $\psi_{s,bulk}$ of the reference solution is shown with a black dotted line. 55

Fig. 3.2 Cumulative transpiration at different soil grid resolutions for the root system scale (RSS) model (solid) and the multi-scale model (dashed). (a): Sand at $\psi_{s,top} = -100$ cm, (b): Loam at $\psi_{s,top} = -659.8$ cm, and (c): Clay at $\psi_{s,top} = -659.8$ cm..... 56

Fig. 4.1: Dimensions of the soil substrates in the experimental containers. 63

Fig. 4.2: Volumetric soil water content in the five containers of the MRI_{sand} subgroup over the course of the experiment. Points indicate measurements. Increases in soil water content are caused by irrigation. 65

Fig. 4.3: Volumetric soil water content in the eight containers of the MRI_{soil} subgroup over the course of the experiment. Points indicate measurements. Increases in soil water content are caused by irrigation. 65

Fig. 4.4: Irrigation schedule for the experimental subgroup MRI_{sand}. 67

Fig. 4.5: Irrigation schedule for the experimental subgroup MRI_{soil}..... 67

Fig. 4.6: Transpiration rates of plants in the MRI_{sand} treatment over the course of the experiment. 68

Fig. 4.7: Transpiration rates of plants in the MRI _{soil} treatment over the course of the experiment.	69
Fig. 4.8: Schematic representation of manual root system reconstructions derived from MRI time-series data at four different root system ages $t_a - t_d$. Root segments are scaled by their respective radius.	70
Fig. 4.9: Manual reconstructions of 13 root systems based on MRI time-series. Data includes age information that is interpolated between the respective measurement dates (see Table 4.1). Root segments are scaled by their respective radius and color-coded based on the interpolated age.	71
Fig. 4.10: Root system architecture of plant 10 derived by two manual reconstructions of MRI scans. Shown is the segment age (age_{sim}) at simulation times (t_{sim}) of 0.1, 7 and 14 days. Root segments are scaled by their respective radius.	72
Fig. 4.11: Order and age-dependent root hydraulic conductivity functions used for parameterization.	73
Fig. 4.12: Root system architecture of plant 10 derived by two manual annotations of MRI time-series scans. Shown is the axial conductivity as a function of root system age at simulation times (t_{sim}) of 0.1, 7 and 14 days. Root segments are scaled by their respective radius.	74
Fig. 4.13: Root system architecture of plant 10 derived by two manual annotations of MRI time-series scans. Shown is the radial conductivity as a function of root system age at simulation times (t_{sim}) of 0.1, 7 and 14 days. Root segments are scaled by their respective radius.	74
Fig. 4.14: Soil water retention curves of the soil substrates used in the experiment. The used retention curve of sand was adapted to the observed bulk density (Sand, adapted).	75
Fig. 4.15: (a): Top and side-view of the hybrid grid used to discretize the cylindrical soil domain, (b): root system of plant 10 embedded in soil domain, (c): initial soil water content distribution at the beginning of the simulation.....	76

Fig. 4.16: Root system metrics derived from manual reconstructions of MRI time-series scans for the subgroup MRI _{sand}	78
Fig. 4.17: Root system metrics derived from manual reconstructions of MRI time-series scans for the subgroup MRI _{soil}	79
Fig. 4.18: Potential transpiration (T_{pot}), actual transpiration (T_{act}) and cumulative transpiration (T_{cum}) of plant 10 grown in soil.....	80
Fig. 4.19: Simulated root collar potential for plant 10 grown in soil.....	81
Fig. 4.20: Xylem water potential of all root segments of plant 10 during peak transpiration at day 3.5 (upper left), 7.5 (upper right), 13.5 (lower left) and during the night of day 14 (lower right).....	82
Fig. A.1: Age-distribution used to assign age-dependent root hydraulic conductivities to manual tracings M (left), manual tracings based on segmented images M+ (middle), and automated tracings A (right). Shown is an exemplary 14-day old <i>Lupinus albus</i> root system of the MRI dataset.....	97
Fig. A.2: Age-dependent root hydraulic conductivities applied in the variable simulation scenario.....	97
Fig. A.3: Manual tracings M (left), manual tracings after segmentation M+ (middle) and automated tracings A (right) of four <i>Lupinus albus</i> root systems (a-d) grown in sand derived by MRI scans. Colors display root orders, root segments are scaled by their respective radius. Age of the root systems is between 8 and 14 days (see Table 2.1).....	98
Fig. A.4: Manual tracings M (left), manual tracings after segmentation M+ (middle) and automated tracings A (right) of four <i>Lupinus albus</i> root systems (a-d) grown in soil derived by MRI scans. Colors display root orders, root segments are scaled by their respective radius. Age of the root systems is between 8 and 15 days (see Table 2.1).....	99

Fig. A.5: Manual tracings M (left), manual tracings after segmentation M+ (middle), and automated tracings A (right) of four <i>Lupinus albus</i> root systems (a-d) grown in sand derived by MRI scans. Age of the root systems is between 8 and 14 days (see Table 2.1). Shown is the root water potential (cm) of the constant simulation scenario, scaled to the maximal and minimal potentials observed for the three root systems shown in each subfigure. Root segments are scaled by their respective radius.....	100
Fig. A.6: Manual tracings M (left), manual tracings after segmentation M+ (middle), and automated tracings A (right) of four <i>Lupinus albus</i> root systems (a-d) grown in soil derived by MRI scans. Age of the root systems is between 8 and 15 days (see Table 2.1). Shown is the root water potential (cm) of the constant simulation scenario, scaled to the maximal and minimal potentials observed for the three root systems shown in each subfigure. Root segments are scaled by their respective radius.....	101
Fig. B.1: Root system architecture of a static 8-day old lupine plant. Red refers to the taproot, purple shows 1 st order laterals.	105
Fig. B.2: Edge-lengths of the grid elements used in the reference solution (black) and the multi-scale model (red) against cumulative volume covered by a certain edge-length.	105
Fig. B.3: Equivalent soil water potential, $\psi_{s,eq}$, (dashed) and mean bulk soil water potential, $\psi_{s,bulk}$, (solid) for multi-scale and root system scale (RSS) model at different soil resolutions in the clay scenario at initial $\psi_{s,top} = -659.8$ cm.	106
Fig. B.4: Cumulative transpiration of the reference solution (dotted) and the multi-scale model at different soil resolutions (solid) for the loamy soil scenario of benchmark C1.2 at initial $\psi_{s,top} = -659.8$ cm.	107

List of Tables

Table 2.1: Properties of soil-grown <i>Lupinus albus</i> plants at time of MRI scan.....	25
Table 2.2: Characteristic root system measures.	32
Table 2.3: Comparison of root measures for <i>Lupinus albus</i> tracings derived by MRI scans. MRI _{sand} gives the mean values of the four root systems grown in sand (see Table A.1), MRI _{soil} gives the mean values of the four systems grown in Kaldenkirchener soil (see Table A.2). M denotes manual tracings derived using unaltered MRI images, M+ denotes manual tracings performed on the U-Net segmentations, A denotes tracings derived by the two-step automated workflow. Superscript lowercase letters denote statistically significant differences between the mean values of the reconstruction types M, M+ and A within the dataset MRI _{sand} and MRI _{soil} , as determined by repeated measures ANOVAs and located between the mean values of the groups by two-sided t-tests. Superscript uppercase letters indicate significant differences between the mean values as determined by Friedman tests and located between the mean values of the groups by two-sided t-tests. If no letter is specified, the mean values are statistically indifferent (see Section 2.2.4.3). Descriptions of the quantitative measures are given in Section 2.2.4.2, equations of measures and descriptions of the constant and variable simulation scenarios are given in Section A3. Note that K_{rs} and zSUF are simulated and not measured quantities (see Eq. A4 - Eq. A6).....	39
Table 4.1: Overview of plants used to derive time-series scans of RSA.	64
Table 4.2: Soil hydraulic properties of the used soil substrates.	75
Table A.1: Comparison of root measures for <i>Lupinus albus</i> tracings derived by MRI scans. MRI _{sand} is comprised of the four root systems grown in sand. M denotes manual tracings derived using unaltered MRI images, M+ denotes manual tracings performed on the U-Net segmentations, A denotes tracings derived by the two-step automated workflow. Descriptions of the quantitative measures are given in Section 2.2.4.2 , equations of measures and	

descriptions of the constant and variable simulation scenarios are given in Section A3. Note that K_{rs} and zSUF are simulated and not measured quantities (see Eq. A4 – Eq. A6). 102

Table A.2: Comparison of root measures for *Lupinus albus* tracings derived by MRI scans. MRI_{soil} is comprised of the four root systems grown in Kaldenkirchen soil. M denotes manual tracings derived using unaltered MRI images, M+ denotes manual tracings performed on the U-Net segmentations, A denotes tracings derived by the two-step automated workflow. Descriptions of the quantitative measures are given in Section 2.2.4.2, equations of measures and descriptions of the constant and variable simulation scenarios are given in Section A3. Note that K_{rs} and zSUF are simulated and not measured quantities (see Eq. A4 – Eq. A6). 103

Table B.1: Soil hydraulic parameters. θ_r is the residual water content, θ_s is the saturated water content, α , and k are the van Genuchten parameters, K_s is the saturated soil hydraulic conductivity and λ is the van Genuchten-Mualem parameter..... 104

Table B.2: Different soil resolutions and their corresponding soil voxel sizes. VS_x , VS_y , and VS_z refer to the soil voxel sizes in x-, y-, and z- direction respectively. VS gives an approximated soil voxel size as used in the manuscript for simplicity..... 104

List of Abbreviations

μ CT	X-ray micro-computed tomography
A	Automated tracing
CNR	Contrast-to-noise-ratio
DAP	Days after planting
FSRM	Functional-structural root architecture model
k_{soil}	Soil hydraulic conductivity
M	Manual tracing based on raw MRI images
M+	Manual tracing based on segmented MRI images
MRI	Magnetic resonance imaging
MRI _{sand}	MRI dataset of plants grown in natural sand
MRI _{soil}	MRI dataset of plants grown in Kaldenkirchener soil
NT	Neutron tomography
RE	Relative error
RSA	Root system architecture
RSI	Root-soil interface
RSML	Root system markup language
RSS	Root system scale
RWU	Root water uptake
SPAC	Soil-plant-atmosphere continuum
SUF	Standard uptake fraction
T_{act}	Actual transpiration
T_{cum}	Cumulative transpiration

T_{pot}	Potential transpiration
VR	Virtual reality
ψ	Water potential
ψ_{collar}	Water potential at the root collar
ψ_{RSI}	Water potential at the root-soil interface
ψ_s	Soil water potential
$\psi_{s,bulk}$	Average water potential of all soil elements within the soil domain
$\psi_{s,eq}$	Equivalent soil water potential
$\psi_{s,top}$	Soil water potential at the soil surface

Chapter I

General Introduction

In the 20th century, agricultural crop production transformed radically due to the “Green Revolution”. Breeding of high-yielding crop varieties, increased land use, as well as the general intensification of agricultural production by increasing the inputs of mineral fertilizers, pesticides, machinery and irrigation, enabled unprecedented crop yields on a global scale. This transformation of agricultural production offered us food security, and enabled us to cope with the ever-rising demand for food from a growing global population (Evenson & Gollin, 2003; Pingali, 2012).

The achieved gains in agricultural productivity can undoubtedly be considered a major achievement from a humanitarian point of view (Borlaug, 2007; Burney et al., 2010). However, these gains were realized by using methods whose suitability for agriculture were predominantly evaluated using a short-term, yield-focused definition of agricultural productivity. Little attention has been paid to ensuring that the resource use and environmental impact of the methods implemented are sustainable over time (Patel, 2013).

For the environment, the intensification of agriculture eventually culminated in a cascade of devastating impacts. At the current state, 33% of the global soil resources are moderately to highly degraded and at risk of further deterioration by human activities (FAO & ITPS, 2015). Erosion, loss of soil organic matter, and nutrient imbalances are the major drivers of anthropogenic soil degradation. They are exacerbated by the widespread use of soil-turning tillage practices (Baumhardt et al., 2015; Lal, 2009; Lal et al., 2004; Montgomery, 2007). This degradation of soils does not only limit their agricultural productivity, and thus our ability to achieve global food security, but also their ability to provide ecosystem services in general (FAO & ITPS, 2015).

Excessive and misguided fertilizer application caused the relocation of massive phosphorus and nitrogen quantities from agricultural fields to their uncultivated surroundings. Rivers and lakes were polluted by soil erosion (via surface water runoff), which resulted in widespread eutrophication of aquatic ecosystems (Brady & Weil, 2016; FAO & ITPS, 2015; Le et al., 2010; Vaccari, 2009). Groundwater, one of the main sources of drinking water, accumulated nitrate concentrations that may render it unfit for human consumption (Ward et al., 2018), as large fractions of nitrogen inputs are leaching from agricultural soils (Grizzetti et al., 2011; Hansen et al., 2017). Moreover, the application of mineral and organic nitrogen fertilizers in excess of the crop requirements is the main source of anthropogenic emissions of the potent climate gas N₂O (FAO, 2022; Reay et al., 2012).

Over time, more and more natural landscapes were dedicated towards food production. At present, agricultural land covers approximately 35-40% of the global land surface (FAO, 2020; Foley et al., 2005). This dominant role of agriculture in global land-use change, from natural landscapes to homogeneous monocultures (Campbell et al., 2017), has also made it the largest cause of habitat destruction, leading to unprecedented declines in biodiversity (Benton et al., 2021).

The systemic shift towards high-input cropping systems, which rely on large amounts of imported phosphate fertilizers, also made agriculture subject to geopolitical relationships. Approximately 95% of the world's phosphate rock reserves are located in just five countries (Cordell & White, 2011). Therefore, global food security is threatened in the long term, not only by the general uncertainty about the remaining quantity of this non-renewable resource (Cordell et al., 2009; Elser & Bennett, 2011), but also by the political intentions of the exporting nations. As shown in the past, protectionist tendencies (e.g. China) and political conflicts between import and export countries (e.g. Syria) can heavily influence the trade of this commodity (de Ridder et al., 2012).

As Benton et al. (2021) aptly noted, our pursuit of cheap and abundant food has led us down a path where we achieved productivity gains by externalizing the true production cost of food onto the environment. Confronted with the consequences of our actions, we slowly started to develop environmental awareness – in some cases, even an environmental conscience. We began to rethink and set out to find a better, more sustainable agriculture. Developed countries,

in particular, started to implement statutory regulations to mitigate environmental damages (Latacz-Lohmann & Hodge, 2003), e.g. by setting maximum levels for nitrate concentrations in water (EU directive EEC/91/676), limiting the amount and timing of fertilizer application, and by controlling the approval of plant protection products (EU regulation No 1107/2009) and their sustainable use (EU directive 2009/128/EC). Many countries have also created incentives for the voluntary adoption of environmentally friendly practices through subsidies (Biffi et al., 2021). Similarly, the United Nations recently integrated agriculture into their Sustainable Development Goals of the Agenda 2030 to stipulate and guide self-imposed efforts of the members at the global scale (UN, 2015).

Although considerable progress towards a more sustainable intensification of agriculture has been made, we have reached a stage at which we require more and more in-depth knowledge to match the increasing complexity of unresolved problems, and to find appropriate solutions for them. Especially in the wake of the anticipated changes in climatic conditions, and the increase in extreme weather events, like droughts and floods (FAO, 2021; Schmidhuber & Tubiello, 2007), this quest will become even more difficult.

The roots, representing the "hidden half" of plants, are of particular interest in the search for more holistic approaches to crop production. To breed or select crop varieties that use nutrients and water efficiently, while delivering high yields under unfavourable climatic conditions, we need to know which root traits define their performance. The phenotype of a root system, expressed through the interaction of its genetic code with the surrounding environmental conditions, is a key factor in deciphering its performance. When plants are grown in opaque soil, direct observation and measurement of root system phenotypes are hardly possible. Although there are methods to retrieve indicative measures of root system phenotypes (e.g. rhizotrons), they are not able to capture the explicit architecture and connectivity of root systems. Recent advances in 3D imaging methods now enable us to derive such explicit root system architectures (RSAs), but they require a large amount of manual labour.

This thesis deals with improving root system reconstruction workflows from magnetic resonance imaging (MRI) images, and the consecutive use of the reconstructed RSAs in functional-structural root architecture models (FSRM), to advance our knowledge of root water uptake (RWU).

1.1 Optimization of Root System Architecture - an Untapped Potential

Roots serve as anchorage for plants and enable them to access the soil and its resources. They are the plants' primary organ of nutrient and water uptake. Roots are therefore essential for plant growth, agricultural productivity (Fitter, 1987) and – on a larger scale – for global food security.

The RSA is commonly defined as the 3D spatial configuration and shape of an entire root system in the form of a continuous geometry. It is an important descriptor in root system phenotyping, as all architectural root traits are intrinsic to this geometry (Lynch, 1995; Osmont et al., 2007). Some exemplary architectural root traits subordinate to the RSA are: root system length, volume, topology (i.e. number of roots per root order), branching angles, radii and its convex hull (Schnepf et al., 2018a).

Although the basic RSA of a plant is defined by its genotype (e.g. taproot or fibrous root system, shallow or deep growth), even genetically identical plants will exhibit a wide range of phenotypes. Phenotypic variation results from interactions between genetically predefined growth with environmental conditions (Malamy, 2005). The ability of plants to include environmental information and signals in order to direct root growth and RSA development, is referred to as plasticity (Rellán-Álvarez et al., 2016). Important triggers of RSA plasticity are the soil water status (Fromm, 2019) and the composition, concentration and distribution of plant nutrients in the soil (Gruber et al., 2013; Hodge, 2004; Linkohr et al., 2002). While a particular soil environment may stimulate specific changes in the RSA of one plant species, it may have different or only minor effects on the RSA of another species (Campbell et al., 1991; Fry et al., 2018; Grime & Mackey, 2002). Thus, the extent to which plastic responses alter RSA is therefore not solely defined by its soil environment, but also by the plant's ability to sense, interpret, and respond to environmental cues (Gruber et al., 2013).

There is a consensus that optimizing RSA represents a large, untapped potential for sustainable crop production, and has been rather neglected in previous breeding efforts. However, the precise role of root system plasticity in this process seems to be less defined (Correa et al., 2019; Giehl & von Wirén, 2018; Herder et al., 2010; Lynch, 2013, 2019; Schneider & Lynch, 2020). Should we breed varieties with low plasticity, whose root growth follows a rather narrow

blueprint designed for a particular set of environmental conditions? Or should we breed highly plastic varieties that can adapt as good as possible to a wide range of environments?

Despite the unclear role of root plasticity as a breeding target, defining root traits that are beneficial for plant growth and plant fitness requires us to measure the RSA. A major obstacle to identifying beneficial root traits is root phenotyping: the opaqueness of soil makes the observation of RSA in natural soil substrates a challenge (Lynch, 2022).

1.2 Measuring the Hidden Half – Methods of Root System Phenotyping

To date, a large variety of root phenotyping methods have been developed and applied. The available invasive methods allow measurements of plants that are grown in natural soil substrate or under field conditions. However, the methods are either based on labour-intensive excavation and rinsing off soil of the root systems, or on destructive subsampling procedures. Invasive measurements therefore only examine a fraction of the root system, or they can only be performed once. Common methods include: “shovelomics” (Trachsel et al., 2011), soil coring (Buczko et al., 2008), and the complete excavation of the root systems (Tracy et al., 2012).

Frequently used methods to derive non-destructive measurements of RSA are: rhizotrons (Nagel et al., 2012), rhizotubes (Cai et al., 2016), hydroponics (Lequeux et al., 2010), rhizoponics (Mathieu et al., 2015), growth pouches (Atkinson et al., 2015), transparent growth mediums (Baghyalakshmi et al., 2020) and agar cultures (Gruber et al., 2013). These methods are well suited to measure many root systems multiple times with reasonable effort. However, they either compromise on realistic growing conditions (e.g., by using artificial growth media), or on capturing the entire RSA in 3D.

Recently, the use of promising non-invasive phenotyping methods has increased. MRI, X-ray micro-computed tomography (μ CT) and neutron tomography (NT), 3D volumetric image acquisition techniques widely applied in medicine, have been used to image soil-grown root systems (Mooney et al., 2012; Pohlmeier et al., 2013, 2018; Tötze et al., 2021). All three imaging methods have been shown to produce high quality 3D images of root systems grown in opaque soil (Metzner et al., 2015; Tötze et al., 2021). The methods can measure not only the full 3D RSA of soil-grown plants, but also their evolution over time.

Although the volumetric imaging techniques offer excellent possibilities for measuring RSA development, they also have drawbacks. First, the dimension of experimental containers that can be used is rather small, which in turn restricts the size and the age of root systems that can be studied. Second, processing the volumetric data is challenging and labour-intensive, which severely limits data throughput.

1.3 Volumetric Image Segmentation – the Virtual Excavation of the Root System

The presence of non-root signals (e.g. soil, water, and organic material) in volumetric imaging data represents a significant challenge. Before the RSA of soil-grown plants can be retrieved, it is necessary to segment the roots from the surrounding soil substrate and other noise. This segmentation requires non-trivial pattern recognition and image processing techniques. Due to overlap in the X-ray attenuation density of roots and the soil environment, μ CT images always need to be segmented (Mooney et al., 2012). The segmentation of NT images poses similar challenges (Mawodza et al., 2020; Rudolph-Mohr et al., 2021). For both methods, the segmentation relies on shape-based methods and requires high quality inputs (high spatial resolution), as well as attenuation corrections (Gao et al., 2019; Gerth et al., 2021; Mairhofer et al., 2012; Mawodza et al., 2020; Phalempin et al., 2021). MRI images, on the other hand, do not necessarily require segmentation. Root detection is based on the difference in signal decay between water in the roots and water in the soil (Metzner et al., 2015). In favourable soil substrates, the contrast between roots and soil can be so high that water in soil is effectively invisible (Pflugfelder et al., 2017; Rascher et al., 2011). In such cases, segmentation is not required, or it can be accomplished by applying a single global signal threshold that excludes the small portions of soil signal (noise) present in the MRI data (van Dusschoten et al., 2016). Nevertheless, MRI images, as well as μ CT and NT images, are adversely affected by high soil water contents and certain soil textures, which greatly reduce the contrast between roots and soil and make segmentation difficult (Pflugfelder et al., 2017; Rudolph-Mohr et al., 2021; Zappala et al., 2013).

A popular strategy to circumvent poor root-soil contrast, is to optimize the experimental conditions in favour of image acquisition. Scanning at low soil water content (Mooney et al., 2012; Rudolph-Mohr et al., 2021; van Dusschoten et al., 2016; Zappala et al., 2013) and

selecting appropriate natural or artificial soil substrates (Pflugfelder et al., 2017; Teramoto et al., 2020), greatly facilitates segmentation.

Although optimizing image quality at the image acquisition stage is very effective in simplifying the segmentation task, it severely restricts our ability to investigate RSA and plastic responses to a large set of environmental conditions (i.e., different natural soil textures and associated water regimes). A possible solution for the efficient use of volumetric data with suboptimal image quality, is to employ sophisticated image processing methods. Recently, artificial neural networks have become the state-of-the-art in image segmentation tasks. The U-Net (Ronneberger et al., 2015), a commonly used network architecture for semantic segmentation tasks of 2D images, has been applied to segment roots from soil in rhizotron images with high success (Bauer et al., 2022; Smith et al., 2020). However, the network architecture has limited capabilities in segmenting volumetric data. Çiçek et al. (2016) later proposed the 3D U-Net. In comparison to the 2D network architecture, the 3D U-Net can contextualize spatial information on the vertical axis for global feature extraction. The 3D U-Net showed excellent performance in 3D image segmentation, and has become extremely popular to segment MRI and CT images in the medical field (Kamnitsas et al., 2017; Milletari et al., 2016). An additional benefit of neural networks in segmentation is their excellent ability in image upsampling. The networks can be trained to derive super-resolution outputs (Uzman et al., 2019). This offers a significant advantage during segmentation, particularly for MRI images which inherently suffer from low resolution. Recently, a 3D U-Net has also been successfully applied to segment roots from volumetric MRI images of soil-grown plants in super-resolution (Zhao et al., 2020). A similar approach was used by Soltaninejad et al. (2020), to improve the segmentation performance of CT images.

1.4 Root System Reconstruction – from Segmented Images to Root System Architecture

Root system reconstruction refers to the derivation of a continuous, fully connected geometry (RSA), from the segmented volumetric images. The objective is to obtain a tree graph structure, also known as the root skeleton, which ideally contains: the geometry, the topology (i.e. root orders), and the functional parameters (i.e. root segment radii) of the root nodes, that together, represent the RSA (Lobet et al., 2015). Such reconstructions are the basis for the calculation of

root system phenotyping traits from volumetric images (McKay Fletcher et al., 2020; Rascher et al., 2011; van Dusschoten et al., 2016). Furthermore, using the reconstructions as direct geometries for simulations in FRSMs, allows us to explore the relationship between RSA and hydraulic behavior (Daly et al., 2018; Koch et al., 2019; Stingaciu et al., 2013; Tötze et al., 2021; Zarebanadkouki et al., 2013, 2016).

An important contribution to the field of root system reconstruction was made by Stingaciu et al. (2013). The authors utilized an early iteration of virtual reality (VR) hardware, consisting of a stereoscopic display and a 3D mouse, to perform manual root system reconstructions from 3D MRI images. In addition, the authors were amongst the first to develop and deploy a fully automated root reconstruction approach to 3D image material (Schulz et al., 2013; Stingaciu et al., 2013). Although both methods produced adequate reconstructions on image material of high quality, the study also highlighted the fundamental challenges that are associated with root system reconstruction.

A common problem encountered in the reconstruction process, is the presence of gaps in the roots. Ferro- and paramagnetic particles in the soil can lead to local signal loss in MRI images (Menzel et al., 2007). On the other hand, gaps are also frequently the result of inaccurate segmentation. Low contrast-to-noise ratios (CNRs), between root and non-root signals, can result in under-segmentation. For MRI images, fractions of the root system may be lost, as finding signal thresholds that sufficiently suppress the soil signal and other noise is challenging (Stingaciu et al., 2013; van Dusschoten et al., 2016). For CT images, low CNRs between experimental containers and roots, tend to result in inaccurate container removal. Hence, roots that are in direct contact with the containers are removed during segmentation and result in gaps (Alle et al., 2023; Metzner et al., 2015; Phalempin et al., 2021).

The fragmented nature of the segmented root system makes the subsequent reconstruction difficult. In manual workflows, the gaps require the reconstructor to spend large amounts of time on manual gap closing (Selzner et al., 2023). Since manual reconstruction in itself is a highly time-consuming process, gaps exacerbate the bottleneck in data throughput. Likewise, the gaps hinder automated approaches, which becomes particularly problematic in combination with other detrimental image attributes, such as low resolution and low CNR (Horn et al., 2021; Schulz et al., 2013; Selzner et al., 2023). Hence, volumetric data is often still reconstructed

manually (Koch et al., 2019; Koebernick et al., 2015; Stingaciu et al., 2013), or the reconstruction requires a high amount of manual interference (Gerth et al., 2021; Pflugfelder et al., 2021; Rudolph-Mohr et al., 2021; van Dusschoten et al., 2016).

In conclusion, volumetric imaging has great potential to help us in our quest to decipher the precise functioning of the root system. The importance of the various methods has long been recognized by the plant science community, which is reflected in several projects that derive large amounts of volumetric data (e.g. SPP Rhizosphere and Rhizo4Bio). At present, there is still a gap between our ability to collect such data and its efficient use. We need to advance the methods for automated segmentation, as well as for automated reconstruction, to alleviate the data processing bottleneck.

1.5 The Effect of Root Hydraulic Architecture on Root Water Uptake from Soil

To understand RSA and its hydraulic behavior in the root-soil system, we need to integrate it into the broader context of the soil-plant-atmosphere continuum (SPAC). The continuous water flow, from soil through plants and into the atmosphere, is referred to as the SPAC. In this continuum, water movement is driven by differences in water potential, and flows along the potential gradient: from high potential (soil) to low potential (atmosphere). Transpiration, the diffusion of water vapour from the substomatal cavities of leaves into the atmosphere, induces the evaporation of water from the leaf cells. Due to the resultant reduction of water potential in the leaf cells, water is drawn from the roots to the leaves, and from the soil into the roots. Hence, plants act as a connector between water in the soil and water in the atmosphere (Taiz & Zeiger, 2010).

Although plants generally absorb large quantities of water, only a small fraction is directly used for growth. The largest fraction (> 95%), simply passes through the plants, and is transpired (Kramer, 1973). Intriguingly, insufficient water supply is nevertheless one of the main factors reducing crop yields (Boyer, 1982; Dawson, 1993; FAO, 2021). This contradiction can be explained by the basic anatomy of plants, which has been evolutionarily optimized for high rates of photosynthesis, rather than efficient water use. The stomata must be open, so plants can absorb sufficient levels of CO₂ for photosynthesis, but open stomata also cause the inevitable

loss of large amounts of water (Kramer, 1973). Due to this trade-off between CO₂ uptake and transpiration, crop growth is ultimately highly proportional to the amount of transpired water (Arkley, 1963).

The transpiration rate itself, is a function of plant parameters and environmental factors, which follows a characteristic diurnal pattern. The most important environmental factors are: the atmospheric evaporative demand (which is dependent on the relative humidity of air), air temperature, wind speed, radiation, and the water supply from the soil (Gates, 1968; Vicente-Serrano et al., 2020). When the water supply of the soil is ample, and the rate of RWU is in balance with the evaporative demand of the atmosphere, the transpiration rate is at its potential maximum. If the evaporative demand surpasses the amount of water that roots can absorb from the soil and transport to the leaves, stomata are closed, and the transpiration rate is lowered. The reduced transpiration is a sign of water stress, which limits growth, and can also lead to heat stress, as transpiration is a key mechanism in cooling plant tissues (Farooq et al., 2009).

To satisfy their transpirational demand, agricultural crops can potentially access the uppermost meters of unsaturated soil. However, plant available water is not merely defined by the amount of water present in this soil region, but also by soil texture, soil porosity, pore size distribution, and the resultant soil hydraulic properties. Depending on the hydraulic properties, the soil retains water with varying force. The amount of energy required to extract water from the soil matrix determines whether or not it is accessible to plants (Jury & Horton, 2004). Hence, the relationship between soil matric potential and soil water content, is an important characteristic of agricultural soils. A common method to determine this highly nonlinear relationship, is based on measuring the hydraulic properties of a soil and using them to calculate soil-water-retention curves. These retention curves offer a continuous description of the soil moisture characteristic (van Genuchten, 1980). Two prominent points on the curves approximate the amount of plant available water, and may be used to estimate it: the water content of the soil at ≈ -60 cm pressure head (field capacity), and the water content of the soil at ≈ -15.000 cm pressure head (permanent wilting point) (Amelung et al., 2018). At water potentials above field capacity (e.g. after rainfall), water drains or evaporates from the soil relatively quickly, and is therefore largely unavailable to plants. At water potentials below the permanent wilting point, water is conventionally considered to be too tightly bound to the soil matrix to be extracted by plants

(Cassel & Nielsen, 1986). Such estimates are useful to evaluate plant-available water at static soil conditions but offer little insight into the water flow from soil to plant itself.

By combining the van Genuchten model with the Mualem model for unsaturated soil hydraulic conductivity (Mualem, 1976), water movement in unsaturated soil can be described by the Richards equation (Richards, 1931). When water is removed from soil pores, it is replaced by air. The more air that is present in the soil, the stronger the water will be constrained to flow through paths of high tortuosity. This sharp decrease in water flow is described by the unsaturated soil hydraulic conductivity, which is a nonlinear function of the water content or matric potential (Jury & Horton, 2004). The removal of water from the soil, therefore, is always accompanied by a simultaneous decrease in hydraulic conductivity and matric potential. When soil becomes dry, due to continuous removal of water, these soil properties consequently reduce the maximal rate of water flow in the soil. (Amelung et al., 2018).

The reduction in soil conductivity has important implications for the water movement from the soil into the plants (i.e. RWU). In wet soil, RWU is largely limited by the movement of water from the root surface into the xylem (North & Nobel, 1996). Nevertheless, the root system conductance is usually sufficient to meet the transpirational demand. In dry soil, the situation differs: when a soil is dry, or becomes dry due to continuous RWU, soil hydraulic conductivity can drop by several orders, and may become lower than the radial conductivity of the roots. Hence, water flow through the soil becomes so slow, that it represents the limiting factor of RWU (Passioura, 1988).

The RSA (i.e. the dimension, the spatial arrangement, and the connectivity of the root system), is therefore especially important, when the water uptake is temporarily limited from the soil-side. It determines from which locations in the soil, water will be extracted (Lobet et al., 2014). The locations and rates of water uptake, however, are not uniformly distributed over the root system. On the one hand, this is due to soil heterogeneity, in terms of water content and soil texture. On the other hand, this is due to varying hydraulic properties of the roots that constitute the root system (Doussan et al., 1998a). Radial conductivity and axial conductance have been shown to vary, depending on root type and root age (Meunier et al., 2018). Furthermore, there is considerable variability between species. Depending on these properties, similar RSAs may result in vastly different rates of water uptake and water uptake patterns (Draye et al., 2010).

The need to characterize root system function, not only by architectural, but also hydraulic properties, is addressed by the concept of root hydraulic architecture (Doussan et al., 1998b). This concept breaks down the RSA to the single root level and allows local information on axial and radial conductivity to be assigned over the root trajectory. Based on the resulting hydraulic architecture, RWU can then be evaluated from the single root to the root system level.

1.6 Unravelling Root Water Uptake with Functional-Structural-Plant Models

The fundamental rules and factors, that govern water flow through the SPAC, are well known. However, experimental studies are typically constrained to measure single determinants of water flow, for a limited set of environmental conditions. Such fragmented information are very important, but difficult to link (Lobet et al., 2014).

In recent years, computational models have emerged as a vital tool for integrating information on water flow in the root-soil system. The increase in computing power has made it possible to delve deeper into the realm of computationally intensive 3D models, which enable the explicit consideration of the 3D RSA (Dunbabin et al., 2013; Schnepf et al., 2020, 2023). An important contribution to the field was made by Doussan et al. (1998b) with the hydraulic tree model. This was the first model to combine a RSA model with equations describing root water flow in 3D. Based on a given spatial distribution of soil water potentials at the root-soil interface (RSI), a water flux or flow at the root collar, and a set of root hydraulic properties, it allowed the calculation of xylem water potentials, uptake and movement of water at any position of a given root system. The model was later extended to include a soil module that calculates water flow in a 3D soil domain. By coupling the soil and root domains, Doussan et al. (2006) realized a 3D water flow model that simulates water flow in soil and roots along water potential gradients. An important novelty of this approach is that the soil is dynamic, and that the soil water potential at the RSI is not prescribed, but a result of the coupled model itself.

As such mechanistic approaches to modelling the SPAC enabled the study of local root-soil interactions and their influence on RWU with unprecedented detail, they became increasingly popular. The approaches combine measured or generated 3D root structures (RSAs), with functional properties of the roots and soil (i.e. hydraulic properties), to simulate the functional

behavior of the coupled root-soil system in RWU (Dunbabin et al., 2006; Javaux et al., 2008). Models that are based on these governing principles, are therefore, commonly categorized as FSRMs (Passot et al., 2019; Schnepf et al., 2020). To date, a variety of FSRM have been developed by different groups in the plant science community. Prominent models include: R-SWMS (Javaux et al., 2008), OpenSimRoot (Postma et al., 2017), DuMu^X (Koch et al., 2018, 2021), SRI (Beudez et al., 2013) and CPlantBox (Giraud et al., 2023; Schnepf et al., 2018b; Zhou et al., 2020). For an excellent overview of the underlying coupling and numerical approaches used in the above mentioned models, the interested reader is referred to Schnepf et al. (2023). Here, we focus on giving a brief overview of CPlantBox-DuMu^X, the modelling framework used in this thesis.

CPlantBox-DuMu^X is a FSRM that simulates water flow in the root-soil system. The model consists of two coupled submodels: CPlantBox (Schnepf et al., 2018b), solves the subproblem of water flow in roots, and DuMu^X (Koch et al., 2021), solves the subproblem of water flow in soil. In CPlantBox, the RSA is represented by a discrete root axis network (tree graph), consisting of linear 1D root segments. The root axis network can either be a generated and dynamic output of CPlantBox, or a predefined network that is derived from measurements (i.e. MRI images). Each root segment in this network contains information about its 3D spatial coordinates, its radius, and its axial and radial conductance. To solve the root subproblem, CPlantBox utilizes the numerical solution of the Doussan model (Doussan et al., 1998b), or the hybrid-analytical solution of Meunier et al. (2017). Based on a transpiration rate, that is prescribed as Neumann boundary condition at the root collar, a no-flux boundary at the root tips, and an initial soil water potential distribution at the RSI, xylem matric potential and RWU for all root segments that together constitute the RSA, are calculated. Note that the Neumann boundary condition is switched to Dirichlet (fixed potential), when the root collar reaches a threshold value of $-15,000$ cm pressure head, which is defined as the wilting point of the plant. This switch of boundary conditions circumvents unrealistic potential values in roots and soil and reflects a RWU stress function.

DuMu^X solves the 3D soil water flow based on the Richards equation (Richards, 1931). Relationships between soil matric potential, soil water content and soil hydraulic conductivity, are defined by soil hydraulic properties, and calculated based on the Mualem – van Genuchten

model (Mualem, 1976; van Genuchten, 1980). In the default approach, DuMu^X solves the soil subproblem using an implicit Euler integration scheme in time, coupled with the finite volume method using a cell-centered two-point flux approximation in space (Khare et al., 2022). Hence, the 3D soil domain is discretized by a numerical grid, in which each soil element holds a single value for each soil parameter (i.e. soil water potential and soil hydraulic properties). By default, the soil grid is composed of rectangular soil elements of equal size. Different boundary conditions can be defined at the top and the bottom of the soil domain, to represent hydraulic events, such as: evaporation, irrigation, or free drainage. The lateral domain boundaries are commonly defined as no-flux.

To connect both subproblems, CPlantBox-DuMu^X embeds the 1D root segment network into the 3D soil domain. Considering RWU as a 1D-3D mixed-dimensional coupled problem, that does not account for the physical presence of roots and their respective volumes in the soil, is a common approach to maintain computational efficiency (Koch et al., 2018). The root-soil interactions in the 1D-3D coupled problem, are described by the sink/source terms of the Richards equation, where RWU is calculated based on the water potential difference between the RSI and the xylem. Water potentials at the RSI are approximated and equal to the soil water potential of the soil element that contains a respective root segment. CPlantBox-DuMu^X employs a sequential coupling of the root and soil subproblems, to derive the respective sink/source terms. The sequential coupling starts with calculating the xylem matric potential and source terms for each root segment in CPlantBox. At the first time step, the water potential at the RSI is based on the initial parameterization of soil water potentials. The calculated source terms for all root segments that are located in a soil element are summed up and passed as sink term to DuMu^X. This is done for each soil element of the soil grid. Next, DuMu^X solves the soil water flow according to the sink terms obtained from CPlantBox. The resulting soil water potentials are passed to CPlantBox and used for the calculation of the xylem water potential during the next coupling time step.

This modelling approach offers a large amount of flexibility: soil hydraulic properties and water status can be specified for each soil element, while root hydraulic properties can be specified for each root segment. We can parameterize different soil textures and a variety of hydraulic events. Hence, the influence of root hydraulic architecture on RWU can be studied for a wide

range of environmental conditions. Additionally, processes that are of importance to RWU (i.e. hydraulic lift), do not have to be parameterized, but are automatically reflected by the mechanistic description of water flow in the models (Javaux et al., 2008).

FSRMs have been used to investigate RSA ideotypes that offer high drought resistance (Leitner et al., 2014), to validate RWU modelling assumptions by comparing simulation outputs with measurements (Koch et al., 2019), and have even be tailored to investigate the influence of RSA on nutrient uptake (Mai et al., 2019; Postma & Lynch, 2011, 2012). Such in-silico investigations offer tremendous help in experimental design. They aid to narrow down the RSA properties that constitute phenotypes worthy of experimental investigation, and can identify potential knowledge gaps (Lynch, 2013).

The large amount of input parameters that can be specified in FSRMs, make them highly customizable, but is also the main challenge in using them. It has been shown that the model outputs are very sensitive to parameterization. This is true for experimentally verifiable parameters, like: the soil and root hydraulic properties that are applied to solve the water flow (Javaux et al., 2008), as well as, for the experimentally derived parameters that are used by the root architecture submodules to derive the RSAs themselves (Landl et al., 2018). In fact, the sensitivity of FSRMs also extends to numerical aspects. As shown by Khare et al. (2022) and Schröder et al. (2008), the resolution of the soil grid can heavily alter the RWU simulated by models.

1.7 Aims and Objectives

Knowledge of the exact spatial arrangement, connectivity, and position of roots in the soil, are of great interest for parameterizing FSRMs and for validating modelling assumptions. Volumetric MRI images of soil-grown plants that are combined with additional experimental observations, have large potential to aid us in deriving such knowledge. At present, the processing of MRI data poses substantial challenges. These challenges are related to the derivation of RSAs from the volumetric images themselves, as well as to the integration of MRI experiments into FSRMs. The overall aim of this thesis, was to advance root-soil systems modelling, based on volumetric MRI images of soil-grown plants. Based on this aim, the following three research objectives were derived:

1. To improve the quality and quantity with which RSAs can be reconstructed from MRI images, by deriving an improved image-processing workflow, that is based on state-of-the-art segmentation and reconstruction methods,
2. To investigate the impact of soil grid resolution on RWU, and implement a computationally efficient modelling approach, that allows the soil environment to be considered at a level of detail that is similar to the highly detailed RSAs derived from MRI images,
3. To enable virtual repetitions of MRI experiments, by developing parameterization methods that allow the observed root growth, and additional experimental data (e.g. cylindrical soil domains, irrigation, and soil water content), to be incorporated into models.

1.8 Thesis Outline

This thesis is divided into five chapters:

Chapter I gives a summary of the recent history of agriculture, and its implications in broader environmental and social context. We explain the importance of the “hidden half” in agriculture, and introduce into popular methods of root system phenotyping, with a focus on highlighting the potentials and challenges associated with deriving RSAs from volumetric images. Subsequently, we explain the key processes that define water flow in the SPAC. We introduce FSRMs, and use the state-of-the-art model CPlantBox-DuMu^X, to give a brief outline on the core concepts of root-soil systems modelling. Finally, we formulate the research objectives associated with utilizing volumetric MRI image material, to advance root-soil systems modelling.

Chapter II deals with the reconstruction of root systems from 3D MRI images. We establish a novel workflow that reduces the bottleneck of MRI image analysis, by deploying a 3D U-Net for the semantic segmentation of the images into roots and soil. Based on the segmentation, we apply state-of-the-art reconstruction methods (manual and automated), to derive the RSAs.

Chapter III investigates to which extent the spatial discretization of the soil domain influences simulated RWU in FSRMs at drying soil conditions. We perform a grid convergence study that quantifies the relationships between soil grid resolution, RWU calculation accuracy, and computational demand. Finally, we demonstrate an alternative modelling approach that greatly reduces the dependence of the simulation accuracy on the discretization of the soil grid.

Chapter IV explores the virtual repetition of MRI experiments in FSRMs. We derive parameterization methods, that allow to mimic experimentally measured root development, based on MRI time-series scans. We combine the MRI scans with additional experimental observations to enable a data-driven simulation of the resulting RWU.

Chapter V summarizes the main findings of the conducted work. We interpret the implications of the research and indicate how it may contribute to guide future endeavours in the context of FSRMs and plant science.

Chapter II

3D U-Net Segmentation Improves Root System Reconstruction from 3D MRI Images in Automated and Manual Virtual Reality Workflows

Based on a journal article published as:

Selzner, T., Horn, J., Landl, M., Pohlmeier, A., Helmrich, D., Huber, K., Vanderborght, J., Vereecken, H., Behnke, S., & Schnepf, A. (2023). 3D U-Net Segmentation Improves Root System Reconstruction from 3D MRI Images in Automated and Manual Virtual Reality Workflows. *Plant Phenomics*, 5, Article 0076. <https://doi.org/10.34133/plantphenomics.0076>

2.1 Introduction

The projected increases in frequency and severity of extreme weather events, combined with the expected growth of the global population, pose a risk to food security (FAO, 2017; Schmidhuber & Tubiello, 2007). There is an urgent need for crop varieties and agricultural management practices that allow yield increases with sustainable use of natural resources, while being resilient to adverse growing conditions such as drought (FAO, 2013; Tilman et al., 2011). For optimization of plant health and yield formation, roots are of utmost importance as they determine the sites in soil where roots take up water and solutes. RSA is often a highly plastic trait that is defined by the soil conditions surrounding the root system (Osmont et al., 2007).

Identifying RSA phenotypes that will perform well under adverse growing conditions is key to define breeding goals for varieties that can meet future challenges. A major constraint of identifying suitable RSAs is root phenotyping (Lynch, 2022). Roots can be readily observed using non-destructive techniques when seedlings are grown in rhizotrons, transparent growth pouches, or artificial growth media, but these methods usually result in 2D images that fail to capture 3D features of the root system. In addition, observations made in soil-free experimental setups are not necessarily transferable to field conditions, due to lack of root-soil-interactions (Atkinson et al., 2019). When roots are grown in soil, the opaque nature of the medium is a challenge. Here, roots cannot be readily observed without destroying the RSA, which hampers subsequent analysis of the plant (Lynch, 1995). Non-invasive methods that can derive the RSA of soil-grown plants are available but need special imaging devices. Magnetic resonance imaging—a 3D volumetric image acquisition method widely known from medical applications—has been used for imaging soil and root systems embedded in soil in the past two decades (Pohlmeier et al., 2013, 2018).

To derive RSAs from 3D images in an efficient manner, non-trivial image processing and pattern recognition are required. In recent years, rapid progress has been made in RSA extraction and soil-related research (Gerth et al., 2021; Koestel, 2018; Wei et al., 2019). Two fundamental steps are needed for deriving RSAs from MRI images: the segmentation of roots from the surrounding soil environment and the subsequent reconstruction of the root system from the segmented images (Schulz et al., 2013; Stingaciu et al., 2013; van Dusschoten et al.,

2016). The detection of roots in MRI is based on the difference in signal decay between water in the roots and in the soil (Metzner et al., 2015). Depending on this difference in signal decay, the segmentation task may be easy or difficult to solve. For a range of soils, the contrast between roots and soil is so high that water in soil is effectively invisible (Rascher et al., 2011). Under these conditions, the MRI scans almost exclusively contain root signals. Simple segmentation operations, such as applying a single global threshold, are adequate to remove the little noise (soil signal) contained in the data. However, achieving high contrast requires measurement settings, soil substrate, and soil water content to be chosen with care (Metzner et al., 2014; van Dusschoten et al., 2016). As shown by Pflugfelder et al. (2017) soil water contents above 70% of the maximum water holding capacity become problematic in sandy soils and Brown's soil. Although the root signal itself is unaffected, large fractions of the soil water signal cannot be suppressed and severely obstruct segmentation of roots and soil due to lower contrast. Consequently, the range of soils and experimental designs that can be readily used in MRI studies is limited, making it difficult to characterize root plasticity across a wide range of soil conditions.

Another challenge when working with MRI images are gaps in the roots. These discontinuities may originate in the MRI data itself or they may be introduced during image processing. As observed by Menzel et al. (2007), ferro- and paramagnetic particles present in natural soils can lead to local, spherical signal losses and general signal deterioration. Findings of Pflugfelder et al. (2017) suggest that the soil texture also influences the image quality, although a strict relationship could not be derived over the full range of tested soils. The authors recommend that the suitability of soil substrates should be evaluated before they are used in MRI studies, as not all aspects affecting image quality are well defined. During segmentation, additional gaps may be introduced when the CNR of the images is low. In these cases, applying thresholds to achieve sufficient visibility of the roots will cause additional discontinuities in the root branches (Stingaciu et al., 2013). This is particularly problematic with thin roots, because they may not only be interrupted by gaps, but can disappear completely.

To obtain a fully-connected geometry, the complete RSA structure must therefore be reconstructed from the 3D images. Reconstructed RSAs can be used to compute root system phenotyping traits (Jiang et al., 2019), or they can directly be used as geometries in FSRM

(Daly et al., 2018; Khare et al., 2022; Koch et al., 2019; Koebernack et al., 2015; McKay Fletcher et al., 2020; Postma et al., 2017; Stingaciu et al., 2013). However, studies usually do not include more than three plants for model applications, except when automated or semi-automated reconstruction algorithms, such as RooTrak (Mairhofer et al., 2012), are available and applicable to the respective data sets (e.g. in Daly et al. (2018) and McKay Fletcher et al. (2020)), where 12 RSAs have been reconstructed from μ CT image time series). Automated reconstruction methods for MRI images have been developed (Schulz et al., 2013; Stingaciu et al., 2013; van Dusschoten et al., 2016), but are built to work with high-quality inputs. As shown by Schulz et al. (2013), capabilities of automated reconstruction algorithms for MRI are severely impeded if the input has gaps, low CNR, and/or low resolution. Although the image resolution can be increased by prolonging the image acquisition time, it comes at the cost of lower CNR (Plenge et al., 2012). Hence, manual reconstruction methods in 3D VR systems (Stingaciu et al., 2013) are still widely used to process MRI images (e.g. Koch et al. (2019)). As manual reconstruction is a time-consuming task, data throughput in MRI root analysis pipelines is severely limited. Ultimately, improvements to CNR as well as to the resolution of MRI images are needed to extend the capabilities of automated reconstruction approaches beyond the use of high-quality inputs.

Recently, artificial neural networks have become state-of-the-art to solve many computer vision tasks, including semantic image segmentation. The rise of deep learning methods in image segmentation can mainly be attributed to their excellent abilities in discovering intricate features of interest in large data sets (Lundervold & Lundervold, 2019). A popular network architecture for 2D image segmentation, the U-Net, was introduced by Ronneberger et al. (2015). In comparison to other architectures, the method is able to achieve good segmentation performance with few training samples and can rely on data augmentation when available training data is sparse (He et al., 2021; Ronneberger et al., 2015). 2D U-Nets have been successfully applied to a variety of segmentation tasks, including segmenting cells in microscopy images (Al-Kofahi et al., 2018), roots and soil in rhizotron images (Smith et al., 2020), solid and gaseous phases in CT images of geological material (Alvarez-Borges et al., 2023) and segmenting pathological lungs from surrounding body tissue in CT images (LaLonde & Bagci, 2018). While the 2D U-Net showed promising results in 2D image segmentation, the method has limited abilities when applied to volumetric images. Input data

is processed slice-by-slice, ignoring 3D context information. Hence, spatial information along the vertical axis is not exploited for global feature extraction (Alalwan et al., 2021). This constraint can be overcome when a 3D network architecture is applied. Çiçek et al. (2016) proposed the 3D U-Net, which uses 3D volumes as inputs, and demonstrated the superior segmentation performance in comparison to an equivalent 2D implementation. Since its introduction, the 3D U-Net has been widely used in the medical field. The network was successfully applied to segment kidney volumes from confocal microscopy images (Çiçek et al., 2016), prostate volumes and brain lesions from 3D MRI images (Kamnitsas et al., 2017; Milletari et al., 2016), and hearth volumes from 3D CT scans (Smith et al., 2022). Zhao et al. (2020) also demonstrated promising results for the segmentation of roots and soil in volumetric MRI data. In addition to their capabilities in image segmentation, neural networks have shown excellent performance in image upsampling. They can derive super-resolution outputs using transposed convolution, where the interpolation is directly learned from the input data (Behnke, 2001; Dong et al., 2014; Uzman et al., 2019).

In this work, we evaluate a novel two-step workflow for automatic MRI root system reconstruction, aimed at overcoming the aforementioned challenges. In the first step, we apply a 3D U-Net developed and trained by Zhao et al. (2020) to increase CNR and resolution of MRI images by performing a segmentation into roots and soil in super-resolution. This U-Net segmentation still contains gaps and small amounts of noise. In the second step, we apply the automated root reconstruction algorithm of Horn et al. (2021), which has been designed to work on imperfect and noisy data. Although both steps have been successfully validated by Zhao et al. (2020) and Horn et al. (2021) under technical aspects, we herein test their practical suitability for RSA trait quantification and for deriving geometries to be used in FSRMs. To evaluate both steps of the automated workflow separately, we compare i) manual expert reconstructions of raw MRI images produced using our default workflow with ii) manual reconstructions performed on the segmented images from Step 1 of the automated workflow, and iii) tracings produced by the fully automated two-step workflow. Manual reconstructions are performed using a novel, state-of-the-art VR system that allows for optimal reconstruction quality. We hypothesize that using the 3D U-Net segmentation will increase the recovered root length in manual reconstructions when compared to our default workflow, which relies on manually applied global thresholds. For the fully automated reconstructions, we

hypothesize that the U-Net segmentation will allow us to process imperfect data with the automated root reconstruction algorithm and derive tracings of similar quality to the manual reconstructions. To test these hypotheses, we performed an MRI experiment with lupine plants grown in two different soil substrates, resulting in two subsets of MRI scans with vastly different image quality. We evaluate the quality of the three reconstruction workflows for MRI by means of visual comparisons of the reconstructed geometries and by calculating characteristic root measures. As the true RSA of plants grown in opaque soil is unknown, validation is based on comparing the reconstructed root lengths to root length data derived with WinRHIZO. In addition, we calculate model-based functional root traits. In contrast to the (isolated) characteristic root measures, these root traits allow us to investigate the integrated functional behavior of the whole RSAs in RWU. By comparing the equivalent conductance of the root systems, as well as the mean depth of water uptake, we can access if systematic differences in root hydraulic architecture between tracing methods exist (i.e. due to incorrect gap closing or differences in reconstructed root radii) and if they are critical for their functional behavior or can be neglected. This is particularly important when evaluating the quality of the automated reconstructions to the manual reconstructions, and thus determining their suitability for use in FSRMs.

2.2 Material and Methods

2.2.1 Experimental Design

The eight MRI scans of white lupine (*Lupinus albus*) used in this work were gathered in an experiment carried out at the Forschungszentrum Juelich. In brief, we used PVC cylinders (height of 21 cm, inner diameter of 5.6 cm) filled with sandy loam ($n = 4$) and natural sand ($n = 4$) to cultivate lupines. In the following, the sandy loam will be referred to as “soil”, and the natural sand will be referred to as “sand”. At the beginning of the experiment, the substrate-filled cylinders were saturated from the bottom to saturation soil water contents of $0.36 \text{ cm}^3 \text{ cm}^{-3}$ for soil and $0.38 \text{ cm}^3 \text{ cm}^{-3}$ for sand. Plants were grown for 8 to 15 days in a laboratory at a relative humidity of approximately 45%, a temperature of approximately 25°C and a day-night cycle of 12h/12h. Photosynthetic active radiation during the day was $450 \pm 50 \mu\text{mol m}^{-2} \text{ s}^{-1}$. The eight experimental containers were scanned by MRI at different time points (Table

2.1). Subsequently, the roots were excavated and washed. They were then scanned with an Epson flatbed scanner with a resolution of 0.005 mm in horizontal and 0.01 mm in vertical direction. The scans were analyzed with WinRHIZO (Regent Instruments, Ottawa, Canada) to determine total root length. A detailed description of the experiment is available in Appendix section A1.1.

2.2.2 MRI Measurements

MRI measurements were performed with a 4.7 T super-wide-bore MRI scanner (Bruker, Rheinstetten, Germany), at water contents between 0.25 and 0.36 $\text{cm}^3 \text{cm}^{-3}$. An overview of the parameters at scanning time is given in Table 2.1. Images were acquired using Bruker’s multislice multi echo imaging pulse sequence (MSME) with a single echo read-out (Bruker BioSpin MRI GmbH). Echo time for sand was $t_E = 6$ ms and for soil $t_E = 5$ ms with an acquisition bandwidth of 150 kHz, a matrix size in the horizontal plane of 256×256 points, two averages, and a repetition time of $t_R = 5$ s. The axial field of view was $70 \text{ mm} \times 70 \text{ mm}$, resulting in a resolution of 0.273 mm for 70 axial slices with a thickness of 0.9 mm in interlaced mode with a gap of 0.1 mm, so that the vertical field of view was also 70 mm. Due to their large height, samples were scanned in three sections (top, middle, and bottom).

Table 2.1: Properties of soil-grown *Lupinus albus* plants at time of MRI scan.

Root system #	Substrate	Plant age (days)	Water content ($\text{cm}^3 \text{cm}^{-3}$)
1	Sand	14	0.36
2	Sand	14	0.31
3	Sand	8	0.33
4	Sand	8	0.32
5	Soil	14	0.34
6	Soil	15	0.25
7	Soil	9	0.30
8	Soil	8	0.32

Subsequently the three sections needed to be stitched together and to be dewarped due to the gradient non-linearity artefact in our MRI system. The detailed description of the performed image-processing is included in Appendix section A1.2. An exemplary root system, resulting from the dewarping and stitching procedure, is depicted in Fig. 2.1.

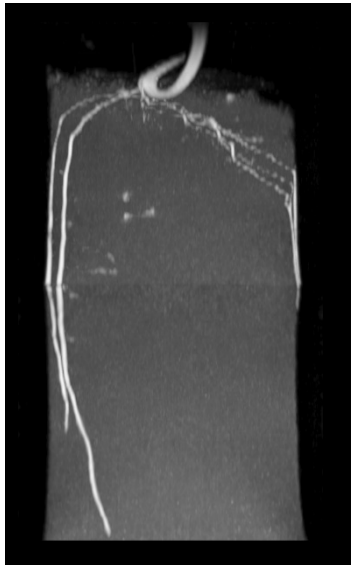


Fig. 2.1: Maximum intensity projection of a MRI scan of a 14-day old lupine root system grown in sand after dewarping and stitching (resolution $0.27 \times 0.27 \times 1 \text{ mm}^3$).

2.2.3 Root Reconstruction Methods

2.2.3.1 Two-step Workflow for MRI Image Segmentation and Root Tracing

Step 1: Image Segmentation in Super-resolution via 3D U-Net

To improve the resolution and CNR of the MRI data, we employ the 3D U-Net previously trained and described by Zhao et al. (2020). CNR is improved by decreasing the intensity of possible noise voxels while increasing the intensity of root voxels. The U-Net increases the resolution by a factor of two along all axes, resulting in a factor of eight for the number of voxels. This image pre-processing is referred to as "Step 1" of the automated reconstruction workflow.

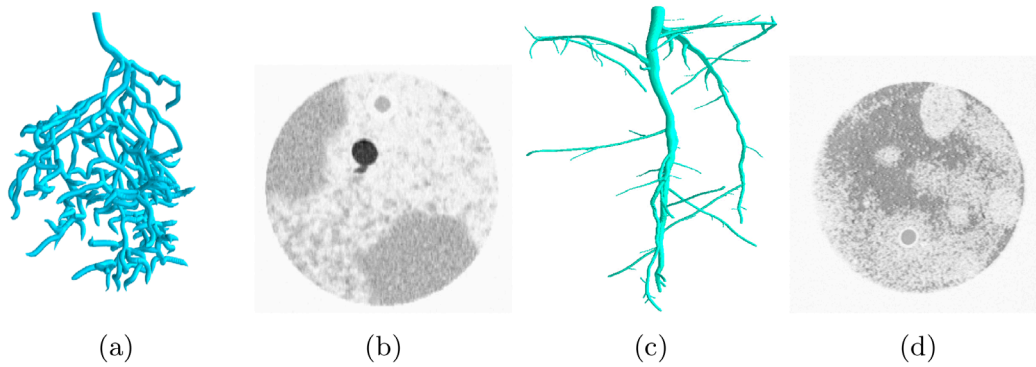


Fig. 2.2: Exemplary visualization of data used for training the U-Net. (a): rendering of manual reconstruction, (b): virtual soil data, (c): synthetic root system, (d): real slice of pure MRI soil.

The dataset used to train the network was combined from two subsets. The first dataset (Fig. 2.2a & Fig. 2.2b) was generated based on three MRI scans of soil-grown plants and their corresponding manual root system reconstructions. The manual reconstructions (Fig. 2.2a) were transformed into 3D paths using thin-spline interpolation. Given a path a 3D tube is constructed around it depending on the reconstructed radius. To increase data variety the reconstructed radius is scaled by $\frac{1}{3}$, $\frac{2}{3}$, 1 and $\frac{4}{3}$. In a second step these roots are rotated along the height axis by 0° , 120° and 240° . This results in a total of 12 different augmentations for each of the three manual reconstructions. To further increase variability of the training set, these augmented reconstructions were then combined with virtual soil data (Fig. 2.2b), simulated based on observed soil noise in real MRI images. This is combined with the second dataset (Fig. 2.2c & Fig. 2.2d), which consists of 30 synthetic root systems generated by randomly growing a path starting from a given shoot. After some distance a path may split. If this is the case, a second path grows at a random angle, sampled from a defined interval, while the original path continuous. These paths are then surrounded depending on randomized radii. The resulting synthetic root systems (Fig. 2.2c) were then combined with noise sampled from real MRI images of pure soil (Fig. 2.2d). To stay within limitations of GPU memory and to allow for a deeper network architecture, the training was performed on 3D image crops of the combined dataset. Variability of the 3D image crops was again increased by augmenting image parameters, such as the contrast between root and soil. Image crops were drawn from the combined data set and split into a training set and a validation set. Validation of the U-Net

on the image crops resulted in a distant-tolerant F1 score of 0.96 (Zhao et al., 2020), indicating good segmentation performance. The evaluation of the trained model, based on a test set of five whole (real) MRI images and their corresponding manual reconstructions, showed that it was able to detect most root branches correctly. Nevertheless, the current implementation of the U-Net does not consider connectivity of roots to the shoot during segmentation, so gaps in the roots caused by missing input information are neither recognized nor bridged. Hence, the segmented 3D images still contain false negatives corresponding to disconnections/gaps in the roots, small amounts of false positives corresponding to noise, and false positives corresponding to roots missed by the human reconstructors. Additional information on the 3D U-Net is available in Zhao et al. (2020).

Here, we used the 3D U-Net to increase the CNR and resolution of the MRI dataset described above. The U-Net segments the MRI images into root and soil in super-resolution. The horizontal resolution of the MRI input data is increased from 256×256 to 512×512 pixels, vertical slice distance is also halved. Subsequently, we use these segmented images in the algorithm-based reconstruction approach as well as in our manual reconstruction setup.

Step 2: Automated Tracing Algorithm

We use the root reconstruction algorithm developed by Horn et al. (2021), herein referred to as "Step 2" of the automated reconstruction workflow, to create automated tracings (A). The

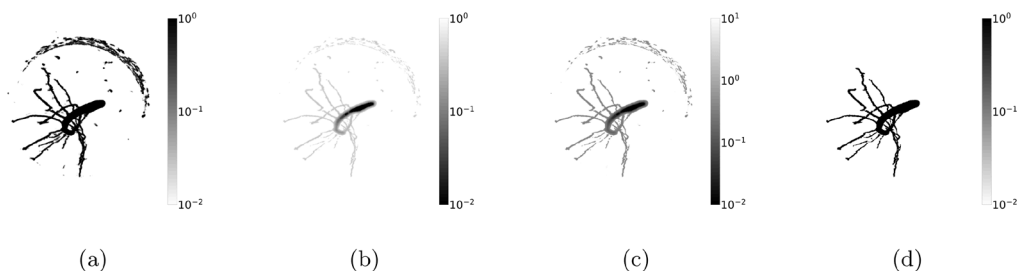


Fig. 2.3: Largest-connected-component extraction with gap closing. (a): segmented input in intensity, (b): voxel cost, (c): adapted cost-map for gap closing, (d): extracted largest-connected component. © [2021] IEEE. Reprinted from Horn et al. (2021).

algorithm itself takes a two-stage approach and is designed to work with imperfect and noisy input data.

In the first stage, the algorithm applies operations aimed at improving the input files once again, by considering the connectivity of the roots to the shoot as additional metric. Starting with the segmented input image derived by the U-Net (Fig. 2.3a), a start point at the uppermost shoot position of the root system is automatically set. Additionally, a minimum voxel intensity is given. Dijkstra's shortest path algorithm (Dijkstra, 1959) is used to extract the largest connected component. A cost map is derived from local radius estimates and signal intensity information and used to evaluate the cost of all voxels above the minimum voxel intensity (Fig. 2.3b). Low costs correspond to a high probability of a voxel being root. High-cost paths from voxels to the shoot are penalized and paths above a defined path-cost threshold are excluded from the extraction, further reducing noise. For imperfect data (i.e. data with gaps), this rigid exclusion of low-intensity voxels and high-cost paths means that portions of the root system will not be extracted. To address this issue, the shortest path algorithm is modified and extended with an option to bridge gaps of a predefined maximum gap length. An updated cost-map with enhanced contrast between gap and no-gap voxels is created to allow the algorithm to connect discontinuous root segments under the defined maximum gap length (Fig. 2.3c). The largest-connected-component resulting from this first stage is a binary volume that excludes noise clusters that are farther than the maximal gap length from the roots and in which root segments are connected by a unique connection (Fig. 2.3d). This fully connected volume now allows the extraction of a root skeleton.

In the second stage, a modified version of the 3D curve skeletonization algorithm described in Jin et al. (2016) is used to extract a root structure graph. A detailed description of the gap-closing modification to Dijkstra's shortest path algorithm (Dijkstra, 1959) and the modification to the 3D curve skeletonization algorithm by Jin et al. (2016) is given in Appendix sections A2.1 & A2.2. Further information is also available in Horn et al. (2021).

2.2.3.2 Manual Tracing in Virtual Reality

We developed and deployed a new VR system for the manual tracing of root systems. Unreal Engine is utilized as frontend and Python/VTK as backend for the computation of geometries from MRI scans. Geometries are visualized as opaque marching cubes isosurface and can be

dynamically adjusted by applying different signal cut-offs (global thresholds) to the intensity values of the 3D images. This allows to define the desired signal contrast between roots and soil and to change it during a reconstruction. The user wears a head-mounted display and interacts with the VR system by using tracked controllers, whose position and orientation are indicated by a digital copy in VR. The displayed data can be moved, scaled, and rotated to give the user an optimal perspective on different areas of the root systems in VR. We chose Root System Markup Language (RSML) as described in Lobet et al. (2015) as output format, a data format for RSA widely used in phenotyping and modelling applications. The hardware setup consists of an HTC VIVE™ Pro head-mounted display with HTC VIVE™ controllers (version 2018) connected to a mid-range desktop computer with a NVIDIA® GeForce® RTX™ 2060 SUPER GPU, an Intel® Core™ i7-8700K CPU, and 32GB of RAM.

The manual reconstruction workflow in VR is displayed in Fig. 2.4. For this schematic illustration, the point-of-view in VR was kept constant. To start the root system tracing, the user loads a raw image file of a scan into the VR system (Fig. 2.4a). The user then picks a signal threshold that allows to differentiate roots and soil as good as possible. Next, a parenting node (i.e. the uppermost point of the tap/primary root) can be defined by clicking on the

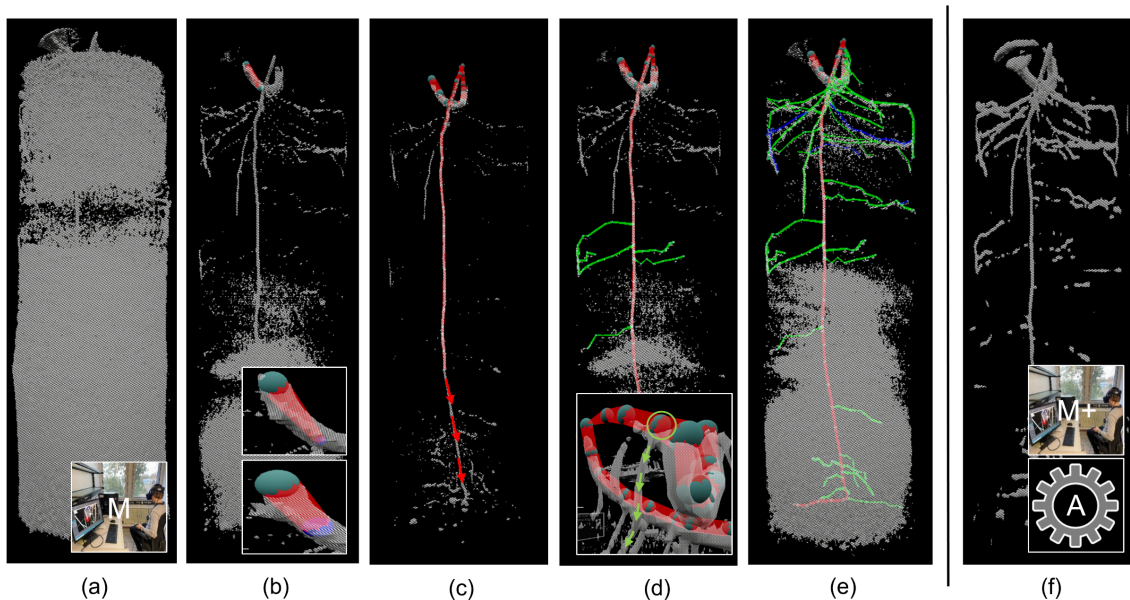


Fig. 2.4: Manual root system reconstruction workflows based on images from the VR application. Shown are the marching cubes isosurfaces of an MRI scan at different signal thresholds (gray) and manual tracings with color-coded root orders at different reconstruction stages. (a): raw image of MRI scan as displayed in VR, (b): threshold adjustment for improved visibility of roots, drawing and adjusting the radius of the first tap root segment, (c): reconstructing the tap root while creating nodes at potential branching points, (d): reconstruction of laterals from bottom to top, (e): finalized manual tracing, (f): U-Net segmentation in VR. Workflow M is based on (a), M+ and A are based on segmented images (f).

respective position on the opaque isosurface. A circular disk appears at the position of the node and can be scaled to the radial dimensions of the isosurface to define the node radius. Now the user follows the isosurface resembling the tap/primary root and defines a second node (Fig. 2.4b). As soon as the tap/primary root consists of two segments (Fig. 2.4c), lateral roots can be created by selecting an inner node and drawing a new root segment (Fig. 2.4d). The VR system also allows corrections and manipulations of the constructed root graph.

Manual tracing was performed by a single person to avoid human reconstruction bias. First, we reconstructed the tap/primary root top to bottom. At all visible branch points, we made a tap/primary root node to facilitate later tracing of laterals (Fig. 2.4c). Then, laterals were reconstructed following the tap/primary root from bottom to top (Fig. 2.4d). We aimed at reconstructing as many roots as possible (Fig. 2.4e). Depending on the CNR of an image, the number of gaps and their length, this may require applying multiple global thresholds and much manual gap closing. The manual gap closing relies on educated guesses that consider similarities in appearance, radius, orientation, position, and trajectory of disconnected root segments.

First, we used this system to perform a manual tracing based on the raw MRI images (M) (Fig. 2.4a). Multiple adjustments of the threshold were needed to achieve sufficient visibility of all roots. Second, we used the system to perform manual reconstructions based on the images segmented by the 3D U-Net (Fig. 2.4f), subsequently termed M+. Due to memory restrictions of the manual reconstruction setup, the super-resolution outputs from the U-Net needed to be scaled down. To achieve this, the U-Net was adapted to map the super-resolution outputs to the original scan resolution of 256×256 pixels. The initial threshold of our manual reconstruction setup (30% of maximum signal-intensity) provided a good balance of roots and noise. Hence, no adaption of this threshold was needed when working on the segmented images.

2.2.4 Measures to Determine Success

2.2.4.1 Visual Comparison of Tracings

We show the RSAs resulting from the M, M+, and A reconstruction methods of MRI images, with the root order per segment color-coded (Fig. 2.5 & Fig. 2.6). RSAs in the result section

are cropped to highlight areas of interest. The complete reconstructions are accessible in Fig. A.3 and Fig. A.4. Root segments are scaled with the radius determined by the respective reconstruction method. The visualization allows qualitative evaluation of differences between the manual reconstruction methods, due to working on raw MRI data or on the U-Net segmentation (Step 1, see Fig. 2.4a & Fig. 2.4f), as well as evaluation of the volume extraction and topological tracing performed by the algorithm in the A tracing.

2.2.4.2 Quantitative Measures

We calculate a selection of common root measures (Schnepf et al., 2018a) to describe RSA and robustness against reconstruction errors of the root systems obtained by the M, M+, and A reconstruction methods. In the results section, the metrics of each reconstruction method are aggregated over the root systems and presented in tabular form. An overview of the calculated root system measures is given in Table 2.2.

We use CPlantBox (Giraud et al., 2023; Schnepf et al., 2018b; Zhou et al., 2020) to load the RSML files of the tracings and then calculate the root measures. In addition to the common root measures, we evaluate differences in root hydraulic architecture of the reconstructions by calculating the model-based functional root system metrics K_{rs} and zSUF for two scenarios. In the first scenario, called constant scenario, we calculate the functional metrics by applying

Table 2.2: Characteristic root system measures.

Variable	Description
RL_{WR}	Root length measured by WinRHIZO (cm)
CNR	Contrast-to-noise ratio (-)
RL	Root length of reconstruction (cm)
Recovery rate	Recovered root length against WinRHIZO (%)
RLD	Root length density (cm cm^{-3})
HMD	Half-mean distance (cm)
r_{mean}	Mean radius of root system (cm)
K_{rsc}	Equivalent root system conductance for constant root hydraulic properties ($\text{cm}^2 \text{day}^{-1}$)
K_{rsv}	Equivalent root system conductance for variable root hydraulic properties ($\text{cm}^2 \text{day}^{-1}$)
zSUF _c	Standard uptake fraction for constant root hydraulic properties (cm)
zSUF _v	Standard uptake fraction for variable root hydraulic properties (cm)
v_r	Manual reconstruction speed (cm min^{-1})

the same fixed axial and radial conductivities to all roots. For the second scenario, called variable scenario, we apply order and age-dependent root hydraulic properties. Used age-distributions and conductivity values are accessible in Fig. A.1 and Fig. A.2.

Three additional measures, not directly related to the RSAs, are included in the results section to enable a more in-depth classification of the results. The available root length information from WinRHIZO measurements, RL_{WR} , is used to calculate the recovery rate. The recovery rate is the best available metric for quantitative validation of root system reconstructions of plants grown in opaque soil. For the M and M+ reconstructions, we also report the respective reconstruction speed, v_r . To give an estimate of the quality of the MRI images, we calculate an exemplary CNR for the raw images. All equations used for the calculation of the variables in Table 2.2 are given in supplemental section A3.

2.2.4.3 Statistical Analysis

All quantitative measures, except CNR, were statistically analyzed using R 4.2.1 (R Core Team, 2022) with RStudio 2022.2.3.492 (RStudio Team, 2022) and the packages rstatix 0.7.0 (Kassambara, 2021) and ggpubr 0.4.0 (Kassambara, 2020). Because of systematic differences in RL and CNR of plants grown in sand and soil of the MRI experiment, we divided the eight plants into two groups and performed separate statistics. As we are interested in the differences between the applied reconstruction methods and not in the differences between the root systems, we subsequently grouped the reconstructions according to the reconstruction methods M, M+, and A resulting in 3×4 reconstructions per substrate. Consequently, we consider the root systems as subjects ($n = 4$), the reconstruction methods as repeated measures of the same subject (i.e. within-subject factor with three levels), and the root metrics as the dependent variables. In the results section, we only report the mean values of the groups M, M+, and A. The individual values per reconstruction method and root system are included in Table A.1 and Table A.2.

We tested the within-subject levels of each analyzed dependent variable for normal distribution by means of Shapiro-Wilk tests. With the exceptions of total root tips, 2nd and 3rd order laterals for the reconstructions of the MRI_{sand} subgroup, and 2nd and 3rd order laterals for the reconstructions of the MRI_{soil} subgroup, the assumption of normality was met. For the

variables following normal distribution, we performed repeated-measures ANOVAs to test for significant differences between the reconstruction methods. During the ANOVAs, the criterion of sphericity was tested. In case sphericity was not met, a Greenhouse-Geisser correction was applied. If the repeated-measures ANOVA revealed significant differences between the reconstruction groups, we performed multiple pairwise, paired, two-sided t-tests (M to M+, M to A, M+ to A), to locate significant differences between the groups. Due to the multiple comparisons, the p-values of the ANOVA were corrected with the Holm-Bonferroni method. For the aforementioned cases of non-normally distributed variables, we performed a Friedman test as non-parametric alternative. All statistical tests were performed at $\alpha = 0.05$. We report significant differences of the post-hoc tests in the tables displaying the root measures. Significant differences found by the repeated-measure ANOVAs are indicated by superscript lowercase letters, significant differences found by the Friedman-test are reported by superscript uppercase letters. If no letter is specified, the mean values are statistically indifferent.

2.3 Results

2.3.1 Visual Comparison of Tracings

RSAs of the eight lupine root systems derived by the M, M+, and A reconstruction methods are displayed in Fig. 2.5 and Fig. 2.6. The age of the root systems is between 8 and 15 days (see Table 2.1). Note that the MRI_{sand} and the MRI_{soil} data sets each consist of two younger (≈ 8 days) and two older (≈ 15 days) plants. Therefore, we observe a large variability in appearance between the root systems of the same dataset caused by the age differences, but also between the root systems of the two data sets obtained in different soil substrates. For the root systems grown in sand (Fig. 2.5), we can observe differences in root lengths between the M+ and M reconstructions. With the exception of the root system in Fig. 2.5c, all M+ reconstructions include roots that are not present in the M tracings. The additional roots are mainly of first order. We also observe slight increases in the length of some roots that are detected in both reconstructions, being longer in the M+ reconstruction. Except for the additional root length included in the M+ reconstruction, the similarity of roots present in both manual reconstructions in terms of root order, root orientation, and root position, is very high. Therefore, working on the segmented images does not have much impact on human decision making for roots that can also be identified when working on the raw MRI images. An exception to this observation is the mean root radius, which is qualitatively larger for the M+ reconstructions.

When we compare the volumetric extraction of the A tracings to the manual tracings, we observe differences to M as well as to M+. Qualitatively, the difference in root radii between A and M+ is smaller than between M and M+. The total root length of A is lower than in M and M+ (see e.g. Fig. 2.5b), with A being more similar to M than to M+. Additionally, we observe an increased number of directional changes in the root trajectories of A. These frequent changes in direction can lead to step-like root trajectories (see e.g. upper half of Fig. 2.5c). Some roots present in both manual reconstructions are missing in A (see e.g. lower section of Fig. 2.5b). This indicates that a portion of the gaps present in the U-Net segmentation are still too large to be successfully bridged by the algorithm. Furthermore, we can observe that parts of the root

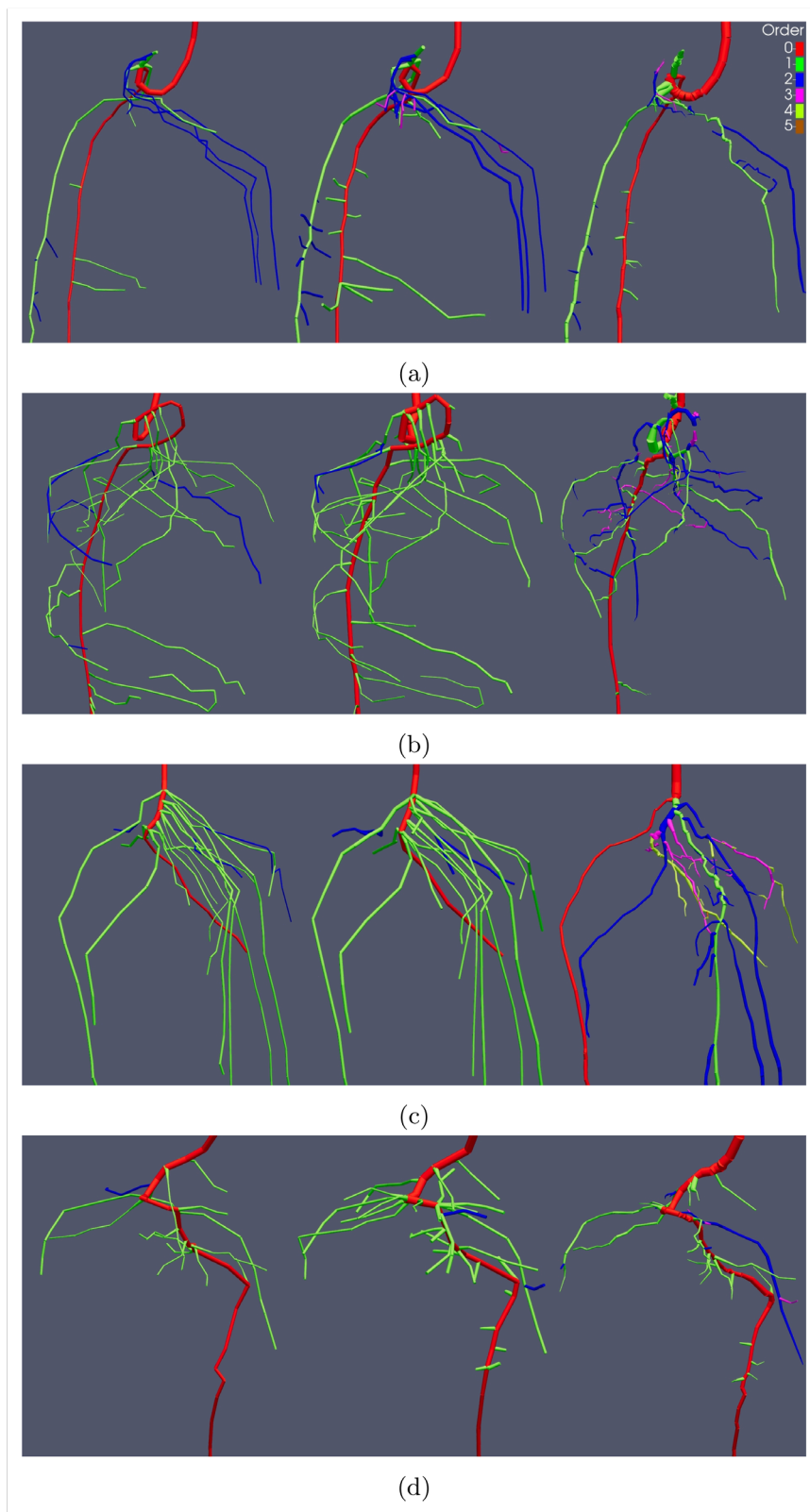


Fig. 2.5: Manual tracings M (left), manual tracings after segmentation M+ (middle) and automated tracings A (right) of four *Lupinus albus* root systems (a-d) grown in sand derived by MRI scans. Reconstructions are cropped to show areas of interest. Colors display root orders, root segments are scaled by their respective radius. Age of the root systems is between 8 and 14 days (see Table 2.1).

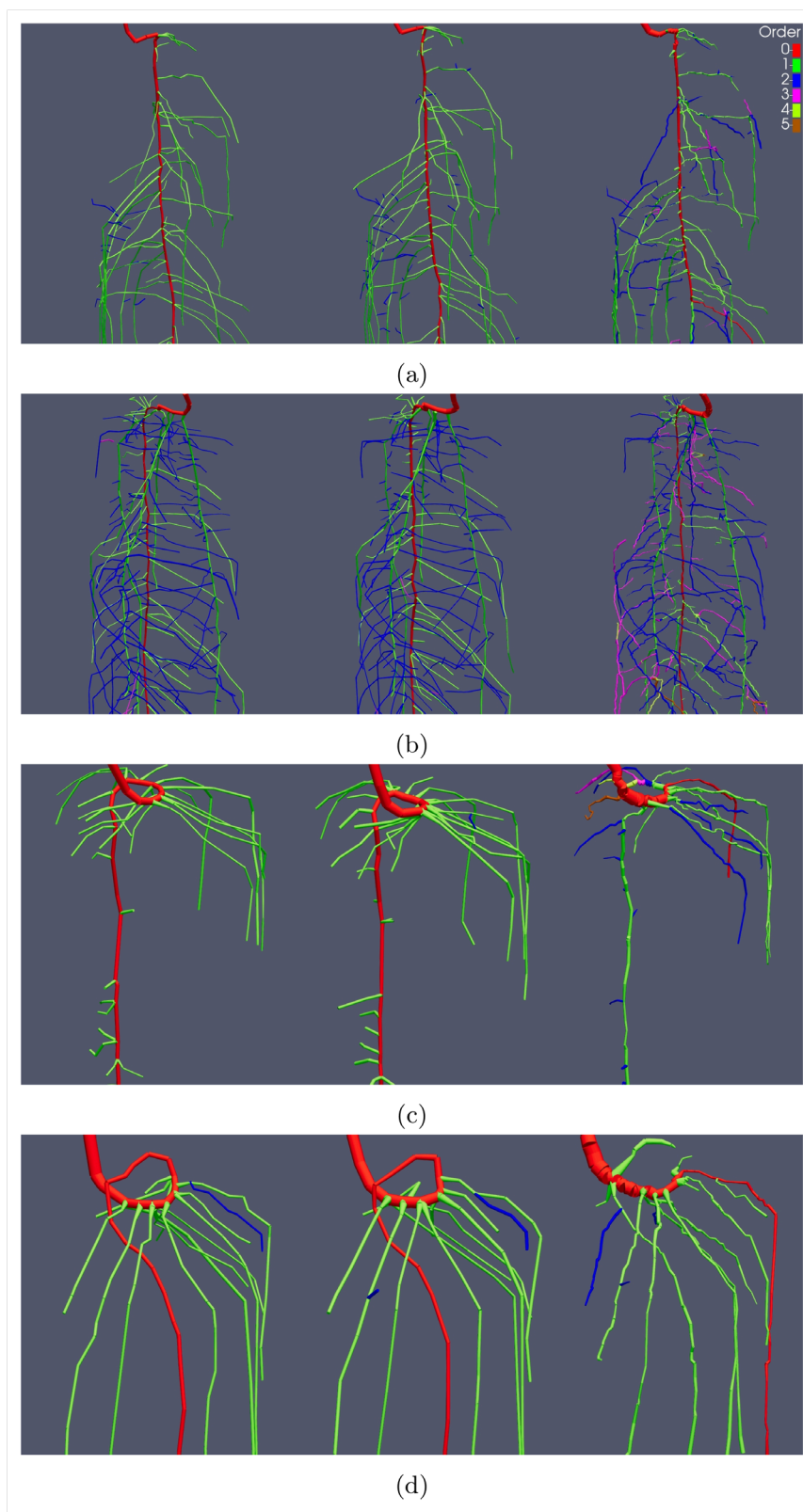


Fig. 2.6: Manual tracings M (left), manual tracings after segmentation M+ (middle) and automated tracings A (right) of four *Lupinus albus* root systems (a-d) grown in soil derived by MRI scans. Reconstructions are cropped to show areas of interest. Colors display root orders, root segments are scaled by their respective radius. Age of the root systems is between 8 and 15 days (see Table 2.1).

systems in A have different connectivity than in M and M+. As visible in the upper-right part of the root system in Fig. 2.5a, the algorithm traces the three second-order lateral roots differently as the human reconstructor. Here, gaps in the segmented image could be bridged to some extent. However, gaps too large to be bridged eventually result in partial root losses as well as in different connectivity of the recovered root segments. Incorrect gap closing seems to occur especially when gaps between interrupted segments of the same root are larger than the distance to an uninterrupted root in direct vicinity. The different connectivity caused by the partial recovery then shifts order of the respective segments towards higher values. Further topological errors in A may be caused by the fact that the topological tracing logic applied by the algorithm is not yet suitable for all cases. In case of root system in Fig. 2.5c, the algorithm identifies a wrong root as the tap root, although the extracted volume suggests other candidates. Again, the orders are shifted towards higher values when compared to M and M+.

For the four root systems grown in soil (Fig. 2.6), differences between the extracted structures are smaller than for the systems grown in sand. The M+ reconstructions do not include significant amounts of additional roots or longer roots than the M reconstructions. In terms of the extracted volumes, same holds true when comparing M and M+ to A: although there are still some gaps present (e.g. upper third of root system in Fig. 2.6a), the volume extraction of the algorithm is more complete. However, the topology derived on the extracted volumes again shows errors. In cases of the root systems in Fig. 2.6c and Fig. 2.6d, the errors are caused by gaps in the upper part of the tap root, which could not be successfully closed by the algorithm. Additionally, we observe errors in topology that are related to merging root structures in the volume extraction. Such merged structures can be caused by roots that are in direct contact with each other. An example of this issue can be seen in the upper region of the A reconstruction in Fig. 2.6c. The uppermost second order lateral root emerging from the tap root splits into two separate roots. When compared to the manual reconstructions, it becomes apparent that this second order lateral root actually consists of two separate second order laterals. Therefore, it should be connected to the tap root by two separate connections that do not branch later on. In the cases of root systems in Fig. 2.6a and Fig. 2.6b (see also Fig. A.4b), topological errors related to the topological tracing logic of the algorithm seem to cause a wrong trajectory of the tap root in the lower third of both root systems. The same applies to other parts of the A tracings, e.g. the ring at the bottom of the system in Fig. 2.6b (see also

Fig. A.4b), where the volume extraction should generally allow a more precise determination of root orders.

2.3.2 Quantitative Measures

Table 2.3: Comparison of root measures for *Lupinus albus* tracings derived by MRI scans. MRI_{sand} gives the mean values of the four root systems grown in sand (see Table A.1), MRI_{soil} gives the mean values of the four systems grown in Kaldenkirchener soil (see Table A.2). M denotes manual tracings derived using unaltered MRI images, M+ denotes manual tracings performed on the U-Net segmentations, A denotes tracings derived by the two-step automated workflow. Superscript lowercase letters denote statistically significant differences between the mean values of the reconstruction types M, M+ and A within the dataset MRI_{sand} and MRI_{soil} , as determined by repeated measures ANOVAs and located between the mean values of the groups by two-sided t-tests. Superscript uppercase letters indicate significant differences between the mean values as determined by Friedman tests and located between the mean values of the groups by two-sided t-tests. If no letter is specified, the mean values are statistically indifferent (see Section 2.2.4.3). Descriptions of the quantitative measures are given in Section 2.2.4.2, equations of measures and descriptions of the constant and variable simulation scenarios are given in Section A3. Note that K_{rs} and zSUF are simulated and not measured quantities (see Eq. A4 - Eq. A6).

Dataset	MRI_{sand}			MRI_{soil}		
	M	M+	A	M	M+	A
Reconstruction method	M	M+	A	M	M+	A
CNR (-)	11	-	-	171	-	-
RL (cm)	92	110	85	226	231	221
Recovery rate (%)	64 ^{ab}	78 ^a	60 ^b	88	91	84
RLD (cm cm ⁻³)	0.20	0.24	0.19	0.50	0.51	0.48
HMD (cm)	1.3	1.2	1.4	1.0	1.0	1.1
r_{mean} (mm)	0.26 ^a	0.34 ^b	0.32 ^{ab}	0.26	0.28	0.26
# of roots (-)	22	36	53	79	91	111
# of 1 st laterals (-)	17	28	20	38	38	25
# of 2 nd laterals (-)	4	6	18	38	50	53
# of 3 rd laterals (-)	0	1	11	2	2	24
K_{rsc} (cm ² day ⁻¹)	2.0E-03 ^a	2.8E-03 ^b	2.4E-03 ^{ab}	3.3E-03	3.5E-03	3.2E-03
K_{rsv} (cm ² day ⁻¹)	1.0E-02	1.3E-02	1.1E-02	1.3E-02	1.4E-02	1.2E-02
zSUF _c (cm)	-4.5	-4.3	-4.6	-6.5	-6.3	-6.5
zSUF _v (cm)	-3.5	-3.1	-3.5	-4.3	-4.1	-4.1
v_r (cm min ⁻¹)	3.3 ^a	6.5 ^b	-	5.8 ^a	7.4 ^b	-

Table 2.3 shows the root measures derived for the MRI root systems grown in sand and soil. The CNR of the MRI images derived for the plants in the two substrates differs substantially. Images acquired in sand have a CNR of 11, resulting in poor contrast between roots and soil and a large number of gaps in the roots, which are also of considerable length. MRI images taken in soil have a comparably high CNR of 171, translating to much better contrast between roots and soil, and less missing information in form of gaps. This is probably due to the high soil water content at scanning time, which is MRI visible in sand, other than in soil. The slower relaxation in nearly saturated sand cannot be faded out completely by the choice of the weakly T_2 -weighted pulse sequence with $t_E = 6$ ms: latter is a compromise between getting sufficient signal from roots and suppressing the signal from sand. For soil with its inherently fast relaxation the sequence works far better.

For the root systems grown in sand, the quantitative measures support the initial findings of the visual comparison. We see differences in RL between M, M+ and A, translating to recovery rates of 64% for M, 78% for M+, and 60% for A. Significant differences are found for the pair {M+,A}, but not for the pairs {M,M+} and {M,A}. RLD and HMD of the reconstructions follow the same pattern as RL and are therefore on a similar level as RL for all reconstruction methods. As root growth is confined by the experimental containers, we observe a linear increase of RLD with increasing RL. The mean root segment radius, r_{mean} , derived in the manual reconstructions M and M+ is significantly different, with a higher radius occurring when working on the segmented images, while there are no significant differences to the mean radius determined in the A tracings. The total number of roots found by M+ is higher than M. These additional roots are almost exclusively first-order laterals.

Although the RL is lower, there are more roots found in A than in both manual reconstructions. These additional roots are of higher orders, as well as of orders ($>3^{\text{rd}}$ lateral) that are generally not detected by the human reconstructor. Remembering the visual comparison, this inflation of root order is to be expected. It is likely associated to errors made by the algorithm and not to errors made during the manual reconstruction: partial gap closing leads to different connectivity and combined with general problems in the topological decision making of the algorithm (e.g. incorrect determination of the tap root), the distribution of roots per order is skewed to higher values. Although these issues inflate the root orders in A, partial gap closing makes the other

root measures more robust, as it still helps to recover larger fractions of RL. Interestingly, the differences in RL and connectivity between the manual reconstructions and A do not transfer directly to the K_{rsc} values. We observe significant differences between M and M+, while the K_{rsc} value of the A tracings is statistically equivalent to M and M+. As this simulation scenario applies the same axial and radial conductivity values to all root segments, the water uptake of a root segment largely depends on its respective root radius. Hence, the higher similarity in mean root radii between M+ and A has greater impact on K_{rsc} than the observed differences in root length and connectivity of A to M and A to M+. The mean depth of RWU, $zSUF_c$, is statistically indifferent for all reconstruction methods. Again, values of M+ and A are more similar than M to M+ and M to A. RWU in the constant scenario can be allocated to a mean depth of approximately 4.4 cm over all reconstruction methods. The more realistic parameterization of the variable simulation scenario, that explicitly assigns different radial and axial conductivities to the tap root and first order laterals, as well as varying them for all root segments based on their respective radii and interpolated age, does not result in larger differences of the RWU metrics. K_{rsv} of M+ and A are further harmonized. We see that this parameterization decreases the mean depth of RWU to values between 3.1 and 3.5 cm depth. The difference of M+ to M as well as to A is higher. This can be explained by the fact that all root systems possess a high number of laterals in the upper region. As the variable scenario attributes a higher radial conductivity to the lateral roots, RWU is shifted towards areas with high RLD and $zSUF_v$ decreases. The effect is more pronounced for M+, since increases in recovery rate are mainly obtained in the upper region of the root systems (see e.g. Fig. 2.5b and Fig. 2.5d).

The difference in reconstruction rate v_r , calculated according to Equation A8, between M and M+ is statistically significant. For the M workflow, we record an average v_r of 3.3 cm root per minute. This rate is almost doubled (+97%) when working on the U-Net segmentation in M+. For images gathered in sand, the manual reconstruction is greatly hindered by the poor CNR. In addition to substantial gaps in the data that have to be connected to the fullest extent possible, noise prohibits identification of small and thin root segments severely. When performing the M reconstructions on unaltered images, multiple thresholds have to be set in order to identify the general trajectory of the roots, as well as to recover unconnected parts of the roots within gaps. This results in much larger reconstruction times. When working on the

segmented image, in which most of the soil signal is successfully removed, the gap closing becomes less challenging. Visibility of roots is improved and closing gaps is easier because the gaps are not as numerous or as large as in the thresholded raw data.

For plants grown in soil, differences between the three reconstruction types are small. We record RLs of 226 cm for M, 231 cm for M+, and 221 cm for A. Resulting recovery rates range between 88 and 91%. Due to the highly similar RLs, differences in RLD and HMD are also small. In this case, we also observe higher similarity of the mean root radii for all reconstruction methods. The significant difference in mean radius between M and M+ is not present for the reconstructions of soil. The number of root tips is slightly increased from 79 to 91, when comparing M to M+, suggesting that the small increase in RL can largely be attributed to finding additional roots. More specifically, the exact same number of 1st order laterals is recorded, while the increase in total number of roots is solely comprised of second order laterals. Again, the segmented image allows detection of additional roots that are of the same order as present in the M reconstruction. Although the number of total roots found in A is the highest, the number of 1st order laterals in A is lower than in M and M+. Once more, an increased number of $\geq 3^{\text{rd}}$ order laterals (see Fig. 2.6), suggests that this increase is caused by partial gap closing combined with general errors in the topological decision making of the algorithm. K_{rs} and zSUF of all three reconstruction methods are highly similar for the constant and variable simulation scenarios, indicating equivalent behavior in RWU. Again, we observe an increase in the reconstruction rate v_r . Although not as prominent as for the root systems grown in sand, we still record a statistically significant increase of 27% in v_r . The reasons for this increase are the same as for the root system grown in sand, but here the manual thresholding achieves a more similar quality to U-Net segmentation.

2.4 Discussion

In this work, we tested a novel two-step workflow for automated root system reconstruction from noisy, imperfect 3D MRI images. Both steps of the automated workflow were investigated for their suitability to improve or replace the currently used manual workflows—under practical conditions. We could show that 3D U-Net segmentation provides fundamental improvements to the manual workflow for the low CNR dataset MRI_{sand} . Substantial increases in mean

reconstruction rate (+97%), root length (+20%), and in root recovery rate (+14%) could be achieved (see Table 2.3). For the MRI_{soil} dataset with a high CNR, the benefits of using the U-Net segmentation were smaller: reconstructed root length was increased by 2%, root recovery rate by 3%, and reconstruction rate by 27%. These results are consistent with our initial hypothesis. When CNR is low, manually set thresholds have limited capability in segmenting the images into root and soil, which is in line with results reported by Pflugfelder et al. (2017) for data derived under similar conditions as the MRI_{sand} dataset. It is tedious and time-consuming to achieve sufficient visibility of the whole target structure. Multiple thresholds need to be applied, since root signal intensities vary over a wide range and are close to or overlap with soil intensity values. Imposing these thresholds results in a substantial number of gaps in the root structure and loss of smaller roots, as low-intensity parts of the root system will be cut off. This cut-off of low-intensity values also led to significant differences in mean root radii of M and M+ (see MRI_{sand} in Table 2.3). At low CNR, applying high signal intensity thresholds to increase root-soil contrast can thin out roots, especially low-intensity root signals at the root-soil boundary. Under these low CNR conditions, the 3D U-Net offers a segmentation performance that cannot be matched by manual thresholding. Gaps in the target structure are less frequent, smaller, and a higher number of low-intensity roots that are close to the signal intensity of the unsuppressed soil signal are still preserved in the segmented images. The additional roots found when working on the segmented images in M+ were of the same orders as present in M. Hence, the U-Net segmentation increased the general visibility of roots but did not allow the identification of potentially present thinner roots of higher orders. On average, the M+ reconstructions still lacked $\approx 22\%$ of the roots in sand, and $\approx 9\%$ in soil. As the performed WinRHIZO analysis did not derive order-specific root measures, we cannot characterize this missing root fraction precisely. In general, MRI protocols suitable for deriving RSAs from soil-grown plants have a minimum detectable root radius, which, for example, was experimentally determined to be ≈ 0.1 mm for the protocol used by van Dusschoten et al. (2016). On the other hand, the increase in recovery rate of M+ in sand can be strictly attributed to finding additional roots of similar radius than found in M; same is true for the small increase in recovery rate in soil. In future experiments, the WinRHIZO analysis should include a quantification of root measures per root order. This would allow us to determine if the missing

root fraction consists of additional roots with similar radii to the detected roots, or if a fraction of the roots is below the MRI detection limit.

For images with high CNR, the benefits of the U-Net segmentation in manual reconstruction are obviously reduced. As shown for the MRI_{soil} dataset, root metrics derived by M and M+ are highly similar (see MRI_{soil} in Table 2.3). The intensity thresholds needed to suppress the soil signal are smaller than in sand. Consequently, the higher contrast allows more suitable thresholds that exclude smaller portions of the root signal. The 27% increase in reconstruction speed is nonetheless interesting, as it emphasizes an additional benefit of the U-Net segmentation: decrease of human reconstruction bias due to a more complete target structure. Most of the time spent on manual reconstruction of raw MRI images was on finding appropriate thresholds and interpreting gaps. As shown by Bauer et al. (2022) for the case of 2D rhizotron images, the variability between individuals reconstructing imperfect images (i.e. gaps in the target structure) can be large. Based on our experience, this also applies to 3D MRI images. It can be assumed that the amount of missing information in the input files is strongly correlated to the divergence of reconstructions performed by different individuals. One aspect of this divergence is the general ambiguity that is introduced by gaps in the data, as gap closing is a subjective task. Small and isolated gaps require little interpretation, while a large number of gaps of considerable length leads to ambiguity in the interpretation of the target structure (see Fig. 2.4). Another aspect are the thresholds chosen to visualize the data. Depending on time expenditure and initial guesses, this procedure can have a certain hit-or-miss character. As the U-Net segmentation offers a way to standardize the thresholding procedure while reducing the amount of missing information in the target structure, we conclude that this image pre-processing approach should lower human reconstruction bias in manual workflows severely. Since the use of the segmented images also increases the recovery rate and the reconstruction speed, we propose that an improved manual workflow for MRI images, as demonstrated in this work with the M+ workflow, can be created by utilizing the U-Net segmentation.

Finally, the differences in recovery rates between the MRI_{sand} and MRI_{soil} data sets highlight the need for careful interpretation of the derived root metrics. Although we could decrease the difference between low and high-contrast data, there still is a systematic difference in the

recovered root length for the two substrates (i.e. $\approx 13\%$ between M+ of sand and soil). Since the amount of roots obtained from MRI data has been shown to vary depending on the used soil substrate (Pflugfelder et al., 2017), the differences in root metrics cannot be attributed solely to root system plasticity. Destructive measurements at the end of the experiment, or destructive empirical preliminary tests, are still necessary to distinguish whether differences are caused by root plasticity or by measurement related factors.

The second step of the automated workflow, an algorithm-based root system reconstruction performed on the U-Net segmentation in super-resolution, showed promising results for the MRI data sets. First, the super-resolution segmentation allowed us to derive meaningful automated reconstructions of the MRI_{sand} data. Since these low CNR data are notoriously difficult to process in automated reconstruction approaches, this in itself is an achievement. Although the recovery rate of the automated tracings is lower than in both manual reconstruction approaches (see Table 2.3, -5% to M, -17% to M+), root metrics of A are generally on a similar level as M. More intriguingly, differences in the radii derived by M and M+ have a larger impact on root system functioning and simulated RWU than the roots missing in A. Hence, we also make substantial errors when processing challenging raw data in our default workflow M. With exception of the root system in Fig. 2.5c, all geometries derived by the automated workflow for the MRI_{sand} dataset seem suitable for use in FSRMs (see Fig. 2.5 & Fig. A.5). Same can be stated for the automated reconstructions of the high CNR dataset MRI_{soil} (see Fig. 2.6 & Fig. A.6). We did not find any statistical differences between the root measures of M, M+ and A (see MRI_{soil} in Table 2.3), and also observed a high similarity of the RSAs derived by the three reconstruction approaches. Nonetheless, we notice different reconstruction quality of the automated tracings for the two MRI data sets. These differences indicate that the performance of the algorithm still depends on the input quality of the segmented images, which was also observed by Horn et al. (2021), and is to be expected for automated approaches in general (Schulz et al., 2013). Although the U-Net segmentation considerably reduces noise and gaps, the gaps and noise remaining in the MRI_{sand} data still lower the quality of the automated extraction. For the analyzed MRI data, the missing information had a stronger impact on the algorithm than on the human reconstructor, suggesting that automated gap closing remains a challenge even when noise is largely absent. The automated gap closing tends to connect disconnected areas to the nearest

neighboring roots, which leads to a substantial inflation of total root tips and derived topology. In contrast, human tracing decisions are based on a broader context of global information when it comes to determining which unconnected root segments are parts of the same root. Local branch orientation is one of the main factors to derive an educated guess during manual reconstruction but is currently not evaluated by the algorithm. Hence, including it as a factor in the automated gap closing procedure could greatly reduce the divergence between M, M+ and A reconstructions caused by differences in the interpretation of missing input data. Nevertheless, the automatic gap closing procedure increases the robustness of the calculated root measures. Although the connectivity is different, most root segments present in the data are recovered.

For both data sets, the topological information derived by the algorithm showed errors resulting from incorrect gap closing (i.e. inflation of root orders), and from general issues related to the logic applied to derive the topology. We suspect that implementing the use of time-series data will allow us to decrease these errors in future iterations of the algorithm. When the automated reconstruction is started with a young root system, fewer roots are present and RLD is usually small. Therefore, it is easier to distinguish between tap/primary roots and the few lateral roots that are present at that growth stage. Gap closing is also less challenging, as the number of potential connection-candidates is lower. Subsequently, an MRI scan acquired at a later growth stage can be used to only track root growth that occurred since the initial measurement. By relying on information derived from earlier time-points, the complexity of determining topology should be lowered. In addition, the use of time-series could also reduce problems related to gaps in the root trajectory. As image quality varies over the course of an experiment, e.g. depending on the irrigation regime and the resulting soil water contents, the visibility of roots and the number of gaps can be expected to fluctuate as well. The use of time-series data could reduce the impact of gaps. Once a root segment is detected, it remains permanently in the reconstruction, whether or not the root signal is present at another measurement time. Such use of time-series data could also help reduce errors associated with merged root structures, which can result from roots coming into direct contact with each other at some point during root growth.

Despite the discussed differences between the reconstructions, the practical benefits of the automated workflow must be evaluated against current common practice. At the moment, data throughput of MRI images is severely hampered by the capabilities of available automated reconstruction methods. Even automated reconstructions derived from MRI images with comparatively high CNR often require manual addition or deletion of certain parts of the root systems (e.g. Pflugfelder et al. (2017)), or manual determination of topology (Pflugfelder et al., 2021)), to retrieve meaningful data. Since we evaluated two data sets that reflect the upper and lower boundaries of MRI image quality in terms of CNR and gaps, it is reasonable to assume that the performance of the automated workflow will gradually improve from the quality obtained for the MRI_{sand} dataset, to the quality obtained for the MRI_{soil} dataset. The automated workflow should therefore enable us to perform MRI experiments in a wider range of soil substrates, as well as at higher soil water contents, since it allows a more efficient use of low CNR data. However, further studies with a wider range of soil substrates are needed to validate this assumption. The results of this work do not necessarily transfer to other plant species. Certain species (e.g. maize), or specific data properties (e.g. missing crown root sections), require specialized adaptations of automated tracing tools to allow meaningful reconstructions. Another example of such complications can be expected for bean root systems. Nodules attached to the root system make automated volume extraction more difficult. It is also to be expected that errors in the second step of the automatic reconstruction process will increase with root system size. Larger root systems tend to be more complex in their architecture, and the containers used in MRI experiments are rather small. As root growth is restricted by the container geometry, RLDs of larger root systems will inevitably increase. The smaller distances between individual roots and an increasing number of roots in direct contact with each other will further complicate automatic volume extraction, gap closing, and the successive derivation of root topology.

At the current state of automated reconstruction methods, visual inspection is essential to ensure qualitative standards are met. In cases of errors that are classified as critical for the intended use of the reconstruction, e.g. using the MRI root system in Fig. 2.5c for RWU simulations, we propose to use the automated reconstruction as scaffold and perform a manual correction. This approach should strike a balance between reconstruction quality and manual

effort. Missing and false-positive roots can be easily corrected when using a system like our VR application, and topology can also be corrected.

2.5 Conclusions

We found that segmentation via 3D U-Net in super-resolution is a new and beneficial step stone in MRI root reconstruction pipelines that reduces manual reconstruction time, increases root recovery rates, and generally enables automated reconstruction of low CNR data. In addition, it offers a way to standardize image pre-processing in manual reconstruction workflows, reducing the influence of different human reconstructors on the derived geometries. Hence, the U-Net segmentation should replace simpler segmentation procedures such as global thresholds, which are currently applied in manual and automated reconstruction workflows. For the automated tracing algorithm, we could show that U-Net segmentation and super-resolution enable a state-of-the-art performance when deriving tracings for data of high and low CNR. However, topological decision making and gap closing of the tracing algorithm still need further improvements. In future studies, we aim to realize these improvements by factoring in local branch orientation during gap closing and utilizing root order information of different growth stages contained in MRI time-series data. In cases where visual inspection of an automated reconstruction reveals an error that is deemed critical to the intended use, a hybrid workflow would be proposed. Here, the automated reconstruction of the segmented image can be used as a scaffold to which manual corrections are applied in an interactive VR environment. This hybrid workflow should allow us to process larger numbers of root images while maintaining optimal reconstruction quality. It will be investigated by us in further studies.

Chapter III

Root System Scale Models Significantly Overestimate Root Water Uptake at Drying Soil Conditions

Based on a journal article published as:

Khare*, D., Selzner*, T., Leitner, D., Vanderborght, J., Vereecken, H., & Schnepf, A. (2022). Root System Scale Models Significantly Overestimate Root Water Uptake at Drying Soil Conditions. *Frontiers in Plant Science*, 13, Article 798741. <https://doi.org/10.3389/fpls.2022.798741>

* These authors have contributed equally to this work and share first authorship.

3.1 Introduction

Most FSRMs used to calculate RWU consider RSAs as networks of discrete cylindrical tubes embedded in 3D soil domains. We refer to those macroscopic models as models on the root system scale (RSS) (Schröder et al., 2009a). Approaching RWU as 1D-3D mixed-dimension coupled problem is computationally more efficient than explicitly considering the physical presence of roots and their respective volumes (Koch et al., 2018). RWU is calculated based on the water potential (ψ) difference between soil and xylem (Dunbabin et al., 2013). When only below-ground organs are explicitly modelled, the water potential at the root-soil interface (ψ_{RSI}) is defined by transpirational demand prescribed at the root collar, soil water status, and soil and root hydraulic properties. If the soil becomes dry due to RWU, soil hydraulic conductivity (k_{soil}) becomes very low, leading to the formation of steep microscopic gradients in soil water potential (ψ_s) around the roots. These gradients are often not spatially resolved by the numerical grid used to simulate the soil water flow (Carminati et al., 2020; Rodriguez-Dominguez & Brodribb, 2020; Schröder et al., 2008). The simulated ψ_{RSI} , which represents the ψ_s that is “felt” by plants and determines their water status, is influenced by the precision with which these gradients are modelled, as ψ_{RSI} is heavily dependent on k_{soil} . When accurately captured, the k_{soil} drop leads to an earlier onset of drought stress, while inaccurate representation may lead to the overestimation of simulated RWU.

Our preliminary solution of an RWU scenario in dry loam for the collaborative benchmark initiative of FSRMs launched by Schnepf et al. (Schnepf et al., 2020) prompts this study. Although we were aware of the grid size dependency of our RSS model under dry conditions (Schröder et al., 2009b), we wanted to test it in detail for this benchmark. We found a rather large overestimation in our RWU calculations compared to the numerical reference solution computed on a fine adaptive soil grid meshed around an explicitly modelled 3D RSA. The resolved interface method used to create the reference is described in Koch (2022). Here, we develop the perspective that for drying soils, RSS modelling approaches are not suitable to capture the drop in k_{soil} satisfactorily and are, therefore, prone to numerical errors. Grid refinement may be used to increase accuracy: in dry soils, the steep part of ψ_s gradients extends only to a few millimeters around the roots (Carminati et al., 2016; Metselaar & De Jong van Lier, 2011; Schröder et al., 2008) and thus, soil grid sizes similar to the root diameters are

needed to resolve them (Koch et al., 2020; Koepl et al., 2018). However, when the soil grid resolution approaches the diameter of the roots, the physical presence of root segments can no longer be neglected (Mai et al., 2019). While methods exist to distribute the sink term across several soil elements when the grid size becomes smaller than the root diameter (Koch et al., 2022), the problem of high problem computational cost remains. To quantify the impact of grid size on RWU from dry soil, we simulate benchmark C1.2 (Schnepf et al., 2020) using our RSS model with different grids and compare the results to the reference solution. Furthermore, we implement an alternative approach by Mai et al. (2019) to show that specialized models developed to represent gradients in ψ within the soil element are required for a correction of ψ_{RSI} in a practice-relevant manner. This continuum multi-scale model represents water fluxes and potentials in the rhizosphere by a 1D radially symmetric model in which fluxes and potential gradients in the axial direction are neglected. This may be justified for small root segments when the gravitational head differences on the length scale of the root segment are small compared to the radial gradients (Mai et al., 2019; Roose & Fowler, 2004; Schröder et al., 2009b), and we use this simplification to be able to reduce the problem to a 1D radially symmetric one. Note that gravity is only neglected in the 1D radially symmetric models. On the RSS, gravity is considered. Ultimately, the multi-scale model allows finer soil resolutions in the radial direction of root segments while keeping the computational costs low. We then use the reference solution to evaluate the results of the RSS and multi-scale model for loam. Finally, we extend the benchmark scenario to investigate the impact of grid size on the k_{soil} drop for the soil textures clay and sand.

3.2 Material and Methods

3.2.1 Benchmark Scenario C1.2

The benchmark scenario is implemented based on section 2.2.5 of Schnepf et al. (2020) and considers the RWU of an 8-day-old lupine with static RSA (Appendix B, Fig. B.1) and constant root hydraulic properties. Axial conductivities are set to $4.32 \times 10^{-2} \text{ cm}^3 \text{ day}^{-1}$, and radial conductivities are set to $1.72 \times 10^{-4} \text{ 1 day}^{-1}$. Root segment diameters range from 0.02 to 0.32 cm, with an average diameter of 0.13 cm; total root length is 53.08 cm; mean root surface area is 21.68 cm^2 . A sinusoidally modulated potential transpiration (T_{pot}) rate of $6.4 \text{ cm}^3 \text{ day}^{-1}$

derived from experimental data is prescribed over a simulation period of 3 days. The 3D soil domain surrounding the RSA has dimensions of $8 \times 8 \times 15 \text{ cm}^3$ and is parameterized as loamy soil. Used soil hydraulic properties are given in Table B.1. Assuming a hydrostatic equilibrium, the initial ψ_s is set at $\psi_{s,top} = -659.8 \text{ cm}$ at the soil surface.

3.2.2 Model Description

The soil water flow equations are solved using an open-source simulation framework, DuMuX (Koch et al., 2021), available through a python binding within our dedicated root-soil interactions module CPlantBox-DuMuX. The 3D soil domain is discretized using structured grids consisting of equally sized cuboids in which the root axes network, which is represented by a discrete network of linear 1D segments, is embedded. In the RSS model, the physical presence of roots in soil is neglected. Following, we will refer to root axis segments as root segments where each root segment has next to its spatial coordinates, root radius, and radial and axial conductivities as attributes. Soil water flow is described by the Richards equation (Richards, 1931), and the hybrid analytical solution of Meunier et al. (2017) is used for solving the water flow in the roots. RWU is calculated based on the potential difference between the RSI and the xylem. We solve the governing partial differential equations using a fully implicit time integration scheme coupled with the finite volume method using a cell-centered two-point flux approximation which holds the mass conservation in each control volume of soil and root. In the RSS model, ψ_{RSI} is approximated by the mean ψ_s of the voxels in which the root segment is embedded. In contrast, the continuum multi-scale approach of Mai et al. (2019) solves the 3D Richards equation on the RSS scale, coupled with a 1D radially symmetric model of soil water flow (1D Richards equation) that is applied on the single-root scale for each root segment. To set up the 1D single-root models, the soil voxel volume, V_s , is divided between all root segments within the voxel proportional to their volume, $V_{rs,i}$, and the total root volume inside the voxel, V_{rst} . The soil volume assigned to a segment is calculated by $\frac{V_{rs,i}}{V_{rst}} \times V_s$, which is then used to define its surrounding hollow soil cylinder as $(r_1^2 - r_0^2) \pi L$, where the segment radius r_0 and the soil cylinder r_1 are the inner and outer boundaries of the 1D radially symmetric single-root model, and L is the segment length. At the inner boundary, water flux is prescribed based on the gradient between ψ_{xylem} and ψ_{RSI} . The net flux into or out of the soil voxel on the RSS is

partitioned between the root segments inside this voxel in proportion to their surface area and prescribed as flux boundary condition at the outer boundary. Distributing the RSS net flux between all soil cylinders in a soil voxel couples both models in a mass conservative way. More details on the multi-scale approach are given in Mai et al. (2019). Both modelling approaches use no-flux boundary conditions at the top and bottom boundaries of the soil domain. We assume zero flux boundary conditions at the root tips and prescribe T_{pot} as flux boundary condition at the root collar. As the ψ_{collar} reaches a threshold ($-15,290$ cm), the boundary conditions are switched, and the collar potential is set at this threshold. Equations of water flow in soil and roots are given in Schnepf et al. (2020). All simulations were performed on a local machine with an Intel® Core™ i5-8365U CPU (@1.6 GHz, 8 Cores) and 16 GB of RAM.

3.2.3 Impact of Grid Size

The RSS model was simulated at uniform soil resolutions ranging from a coarse grid of ≈ 4.0 cm to a comparatively fine grid of ≈ 0.2 cm with soil grids consisting of equally sized cuboids with almost same edge-lengths in XYZ directions. We idealize them to be cubic and give one approximated edge-length to denote the grid size (Table B.2). The 1D cylinders of the multi-scale model are discretized by 60 elements each while using a logarithmic scaling with grading factor of 1.5 (40,000 elements in total). Hence, we achieve the highest spatial resolution close to the root surface. The mean edge length is 0.08 mm, the minimum is 6.8×10^{-3} mm, and the maximum is 3.2 mm. The adaptive grid of the reference is gradually refined toward the roots and consists of 1.45 million tetrahedral cells with a mean edge length of 1.06 mm, a minimum of 3.46×10^{-4} mm, and a maximum of 3.16 mm. A comparison of 1D and reference grid is given in Fig. B.2. RWU is simulated with RSS and multi-scale model and results are compared to the numerical reference solution. Relative error (RE), defined as $\frac{(f_i - f)}{f}$, is used to quantify the differences to the reference where f_i is the cumulative transpiration (T_{cum}) at the “ i^{th} ” soil resolution, and f is the T_{cum} of the reference solution.

Based on root hydraulic architecture, we compute the standard uptake fraction (SUF) of each root segment, yielding the relative contribution of each root segment to RWU in case of a uniform ψ_s . These SUF values are used as weighing factor to calculate the weighted average of

ψ_s of voxels containing root segments (Couvreur et al., 2012; Meunier et al., 2017). The resultant weighted average, known as equivalent soil water potential, $\psi_{s,eq}$, is a metric that represents the actual ψ_s “sensed” by the plant. We also calculate $\psi_{s,bulk}$ as the average of all soil elements within the domain.

3.3 Results

Results of the RSS model at different soil grid resolutions and the multi-scale model for benchmark C1.2 are shown in Fig. 3.1a. The solid black line shows the potential T_{cum} resulting from a mean T_{pot} rate of $6.4 \text{ cm}^3 \text{ day}^{-1}$ per plant. For the given RSA with a root surface area of 24.42 cm^2 , this is equivalent to a mean water flux at the root surface of $3.42 \times 10^{-6} \text{ cm s}^{-1}$ which is a typical value, refer to e.g., Roose et al. (2001); Nye and Marriott (1969). For the RSS model, no stress is observed for a 4.0 cm grid. Starting at a soil resolution of 3.0 cm, drought stress is observed and with further refinement, its onset is shifted to earlier times. REs decrease from 3.26 at 3.0 cm to 0.30 at 0.2 cm. The needed wall-clock times range from 19 s to 21.2 h.

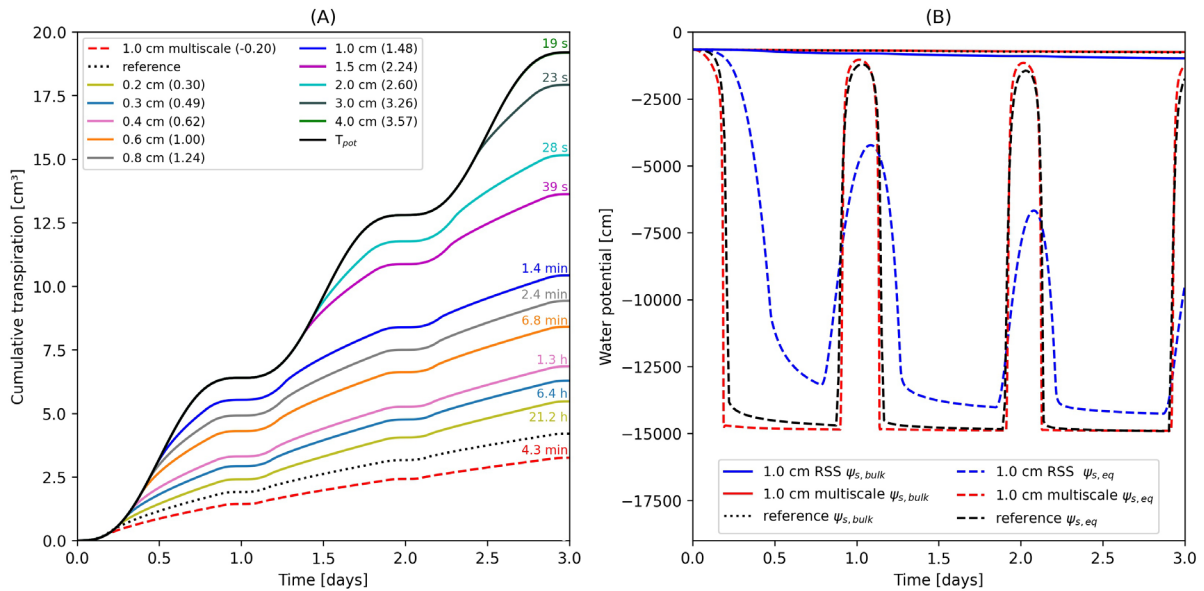


Fig. 3.1: (a): Cumulative transpiration of the numerical reference solution (dotted), the multi-scale model (dashed), and the root system scale (RSS) model at different soil resolutions (solid) for the loamy soil scenario benchmark C1.2 at initial $\psi_{s,top} = -659.8 \text{ cm}$. Values in parentheses indicate the relative error (RE), numbers above lines indicate the wall-clock time required to compute the respective simulation. (b): Equivalent soil water potential, $\psi_{s,eq}$, (dashed) for the reference solution (black), and for RSS (blue), and multi-scale model (red) while using a bulk soil resolution of 1 cm. Blue and red solid lines show the mean bulk soil water potential, $\psi_{s,bulk}$, of the soil domain in RSS and multi-scale model, $\psi_{s,bulk}$ of the reference solution is shown with a black dotted line.

Applying the multi-scale model results in a T_{cum} of 3.2 cm^3 after 3 days. In comparison to the numerical reference solution, we observe a RE of -0.20 with a required computation time of 4.3 min. As the reference solution was computed externally on different hardware, we cannot give a comparable wall-clock time.

While an initial $\psi_{s,top}$ of -659.8 cm in a loamy soil might not seem very dry from an experimental standpoint, our simulations show that considering rhizosphere gradients will lead to uptake limitations rather quickly. A visualization of the simulated $\psi_{s,bulk}$ and the $\psi_{s,eq}$ sensed by the roots for reference, RSS and multi-scale model is given in Fig. 3.1b. Although we apply a 1 cm grid on the RSS in both approaches, the gradients in the soil differ substantially. Quicker water replenishment in the vicinity of the roots leads to smaller ψ gradients between RSI and bulk soil in the RSS model. Utilizing the multi-scale approach results in sharper k_{soil} drops that are formed faster and result in larger ψ_s gradients. An additional plot of $\psi_{s,eq}$ showcasing the transition from non-stressed to stressed conditions for multi-scale and RSS model is shown in Fig. B.3.

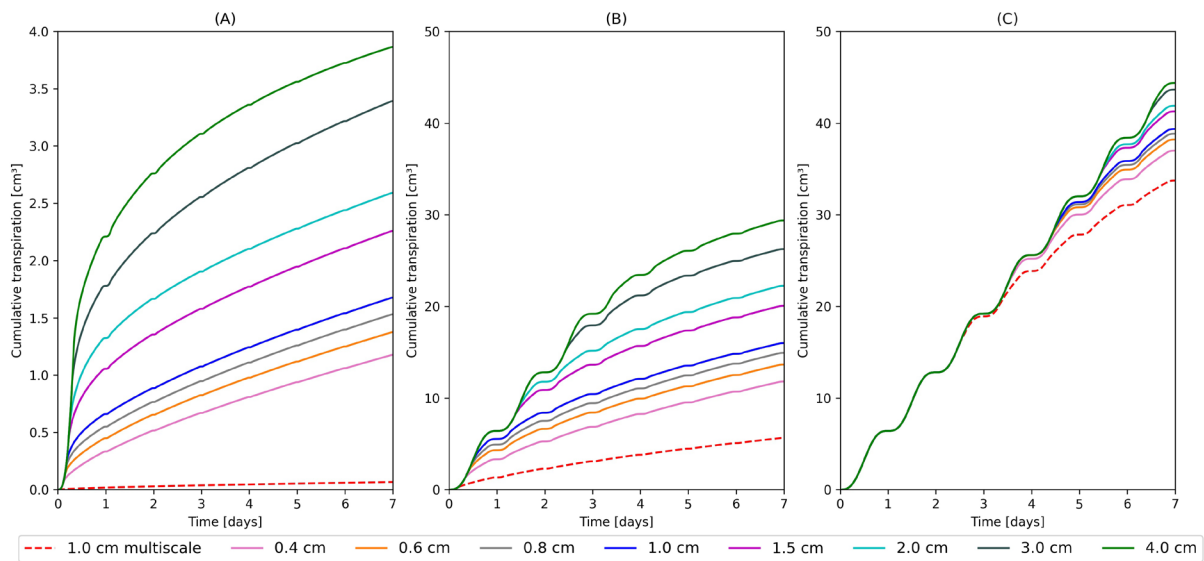


Fig. 3.2 Cumulative transpiration at different soil grid resolutions for the root system scale (RSS) model (solid) and the multi-scale model (dashed). (a): Sand at $\psi_{s,top} = -100 \text{ cm}$, (b): Loam at $\psi_{s,top} = -659.8 \text{ cm}$, and (c): Clay at $\psi_{s,top} = -659.8 \text{ cm}$.

We expanded the benchmark setting to include a sand and clay scenario (Fig. 3.2). Simulation time was increased to 7 days to include times of interest for clay. We used the same initial

condition of $\psi_{s,top} = -659.8$ cm for clay. For sand, we opted for a more agronomically relevant $\psi_{s,top}$ of -100 cm. For the case of dry sand, Fig. 3.2a, we observe stress onset on day 1 for both modelling approaches. Even the RSS model with a grid of 4.0 cm only reaches a T_{cum} of 3.9 cm³ after 7 days. As the grid is refined, T_{cum} is successively reduced to 1.2 cm³ for the 0.4 cm grid. For the multi-scale model, we observe an even earlier reduction in transpiration, leading to a T_{cum} of 0.06 cm³ at the end of the simulation. Hence, even the 0.4 cm grid overestimates the T_{cum} by a factor of ≈ 20 compared to the multi-scale model. In the dry clay soil, Fig. 3.2c, no stress is simulated while using a 4 cm grid and 44.8 cm³ are transpired after 7 days. We see a transpiration reduction starting at 6.4 days for the 3.0 cm grid. Further grid refinement to 0.4 cm decreases the T_{cum} to 37 cm³ after 7 days. The multi-scale model simulates a T_{cum} of 33.7 cm³. Consequently, the difference between the models is smallest for this soil.

3.4 Discussion

Overestimation of RWU under drying conditions using RSS modelling concepts was found to depend on soil discretization for all soils analyzed in the scenarios (Fig. 3.2). Even fine grids (0.2 cm) resulted in 30% overestimation of T_{cum} compared to the numerical reference solution (Fig. 3.1a). The multi-scale model underestimated the reference solution by 20%. However, we need to keep in mind that the reference is itself a numerical solution. A larger fraction of the total soil volume than in the reference solution is covered by small edge-lengths in the multi-scale model (Fig. B.2). Conceptually, as the multi-scale model assumes equal distribution of root segments within the voxel, it is more likely to still overestimate RWU. Nevertheless, we could demonstrate that the multi-scale model outperforms the RSS approach in accuracy, while being roughly 300 times faster (Fig. 3.1a) and being more stable for different grid sizes (Fig. B.4). Due to the lower computational effort, simulations of large RSAs and multiple RSAs in parallel are still possible on a local computer. We are aware that adaptive grids, only refined in areas containing root segments, would improve the performance of the RSS model. However, as shown by Schröder et al. (2009b), use of adaptive refinement with acceptable error margins would improve the speed with an order of magnitude of one at best. It also remains to be investigated whether other numerical methods, such as FEM, in combination with unstructured

grids exhibit similar grid dependencies, and if the continuum assumption is still suited to describe water flow on very fine grids as used in the multi-scale model.

Whether a more detailed representation of k_{soil} gradients through the demonstrated improvements in rhizosphere soil process descriptions alone leads to more realistic RWU predictions is still debatable. Biophysical processes, such as mucilage deposition (Carminati et al., 2016; Kroener et al., 2014; Landl et al., 2021), have been shown to create challenging entanglements in the rhizosphere, which can heavily alter the k_{soil} gradients. On the other hand, a gap between process descriptions and the current means of measurement methods could be introduced or widened. RSAs derived using MRI or CT can miss a significant proportion of fine roots (Metzner et al., 2015), which could lead to a systematic underestimation of RWU if used in modelling approaches such as the multi-scale model. Missing fine roots would lead to an overestimation of RWU per unit root length for the remaining roots and larger ψ_s gradients around the roots would limit transpiration earlier. As Cowan (1965) shows, such changes in the ratio of total root length to T_{pot} can significantly alter $\psi_{s,eq}$, $\psi_{s,bulk}$, and their daily patterns, making reliable parameterization of this ratio an ongoing challenge. In addition, current measurement methods do not allow soil hydraulic properties to be reliably determined at the rhizosphere scale and we, therefore, lack the possibility to validate simulations.

Despite these challenges, we are convinced that a shift in RWU modelling paradigms for drought conditions and rhizosphere processes, in general, is needed. A new generation of more advanced RWU models is starting to emerge. Most of these approaches utilize simplified local models around the root segments coupled to RSS models defined on a coarse grid. The ψ_{RSI} is approximated numerically (Mai et al., 2019) or by a local analytical solution based on the Kirchhoff transformation of the 1D radially symmetric Richards equation and a steady-rate (Schröder et al., 2009a) or steady-state assumption (Koch et al., 2022). In addition, Koch et al. (2022) allow distributing sink terms around root segments over a small radially symmetric tubular support. Beudez et al. (2013) also use a local analytical solution of the linearized form of the Richards equation (Richards, 1931) and additionally apply the superposition principle to account for potential uptake competition due to dense root clusters. Graefe et al. (2019) also extended a cylindrical root model to account for non-regular root distributions. In addition to non-regular root distributions, de Willigen et al. (2018) included partial contact between roots

and soil in cylindrical models. Ultimately, it will be these approaches that serve as frameworks to consider rhizosphere processes and upscale them to the RSS. They combine computational efficiency with the option to incorporate rhizosphere-scale information if it becomes available and enable comparisons between simulations and data at this scale.

Chapter IV

Parameterizing In-silico Replications of MRI Experiments

Based on the draft of a book chapter to be published as:

Selzner, T., Helmrich, D., Landl, M., Leitner, D., Lobet, G., & Schnepf, A. (2024). Chapter 16: Coupling of MRI and modelling. In Pohlmeier, A., Haber-Pohlmeier, S., Stapf, S. (Eds.), *NMR in Plants and Soils*. Royal Society of Chemistry.

4.1 Introduction

Root phenotyping is a major obstacle to identifying root traits that will allow plants to cope with the future changes in growing conditions (Lynch, 2022). Conventional root phenotyping methods are either limited in their ability to monitor root growth (Trachsel et al., 2011), to determine the complete 3D architecture of the root system (Buczko et al., 2008; Nagel et al., 2012), or to observe roots grown in natural soil media (Atkinson et al., 2019; Lequeux et al., 2010; Rich et al., 2020).

MRI (Pflugfelder et al., 2021; Pohlmeier et al., 2013; Stingaciu et al., 2013), μ CT (Daly et al., 2018; Mooney et al., 2012) and NT (Bereswill et al., 2023; Mawodza et al., 2020; Tötze et al., 2021), have been successfully used for non-destructive imaging of root systems embedded in soil. These non-invasive volumetric imaging techniques have their own drawbacks (e.g. challenging image processing (Selzner et al., 2023)), but also offer great potential. They are capable to derive explicit 3D RSAs of soil-grown plants, and can be used to monitor root development in a range of different natural soils, by performing multiple scans (Atkinson et al., 2019; Pflugfelder et al., 2017). Time-series scans of the RSA offer us unique possibilities to investigate root growth and root-soil-interactions over time. The scans may be used to derive root system phenotyping traits, and explicit 3D RSAs of plants at different stages of their development (Pflugfelder et al., 2021). These explicit RSA time-series can also be directly used as geometries in FSRMs. Such data on root development are particularly useful for studying root-soil interactions, when they are supplemented with experimental data on soil water content and dynamics (Haber-Pohlmeier et al., 2010; Koch et al., 2019; Koebernick et al., 2015; Tötze et al., 2021).

Although time-series data acquired by volumetric imaging techniques are well suited to investigate water transport in the SPAC, and to validate modelling assumptions of RWU, incorporating such data into FSRM, is not trivial. In this chapter, we showcase the workflow of incorporating data from MRI experiments into the FSRM CPlantBox-DuMu^X (Giraud et al., 2023; Schnepf et al., 2018b; Zhou et al., 2020). The parameterization aims to facilitate a virtual repetition of the experiment. We then show example modelling outputs that can be derived from such a virtual replication of experiments.

4.2 MRI Experiment and Gathered Data

MRI Experiment

The following is a short description of the essential elements of the MRI experiment that is virtually replicated in CPlantBox-DuMuX.

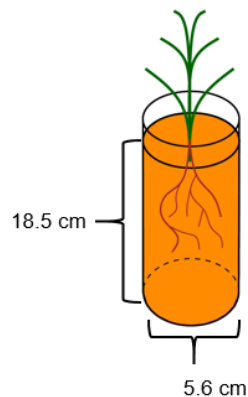


Fig. 4.1: Dimensions of the soil substrates in the experimental containers.

Lupine seeds (*Lupinus albus*) were germinated on wet paper for four days and planted into substrate-filled cylindrical plastic containers. The transfer of the seeds marks day after planting (DAP) zero. Used cylinders were 23 cm in height, had an inner diameter of 5.6 cm, and were filled with two different soil substrates to a height of 18.5 cm (Fig. 4.1). One substrate was natural sand (FH-31), the other a sandy loam taken from Kaldenkirchen. Henceforth, the sandy loam will be referred to as “soil”, and the natural sand will be referred to as “sand”. Plants grown in the respective soil substrates will be divided into the subgroups MRI_{sand} and MRI_{soil}, accordingly. To prevent evaporation, a layer of coarse gravel was added as a capillary barrier at the soil surface. The cylinders were perforated at the bottom, and the holes were covered with a nylon mesh. Subsequently, the substrate-filled cylinders were saturated from the bottom to saturation soil water contents of $0.36 \text{ cm}^3 \text{ cm}^{-3}$ for soil, and $0.38 \text{ cm}^3 \text{ cm}^{-3}$ for sand. Irrigation was performed with tap water, consistently every second to third day from the top, to compensate for approximately half of the transpiration loss.

The plants were grown over a period of four weeks, while a subgroup of plants was harvested once a week. During the experiment, the individual containers were scanned up to four times

by MRI, to obtain the RSA at different root system ages. Strong overlaps of roots at later growth stages prohibited the analysis of MRI images of older plants. Hence, the analysis of RSA was mostly limited to plants younger than 20 days.

Table 4.1: Overview of plants used to derive time-series scans of RSA.

Root system #	Substrate	Plant age at MRI scan (days)
1	Sand	5, 13
2	Sand	10, 17, 24
3	Sand	8, 14
4	Sand	8, 14
5	Sand	6, 8
6	Soil	7, 13, 19, 26
7	Soil	7, 13, 18, 25
8	Soil	5, 10, 17
9	Soil	5, 10, 17
10	Soil	10, 14
11	Soil	6, 15
12	Soil	7, 9
13	Soil	6, 8

Root System Architecture

MRI image-processing was carried out as described in Section A1.2. Ultimately, MRI images of 13 plants were suitable to derive time-series of RSA. The root systems of the 13 plants were manually reconstructed with the Holobench (Stingaciu et al., 2013), at all plant ages given in Table 4.1.

Volumetric Soil Water Content

Soil water contents were monitored by the weighing of the experimental containers. By subtracting the dry weight of the filled-in substrate and the weight of the containers themselves,

the absolute amount of water in the soil domain was obtained. The absolute amount of water was divided by the dry weight of the soil substrate, to obtain the gravimetric soil water content.

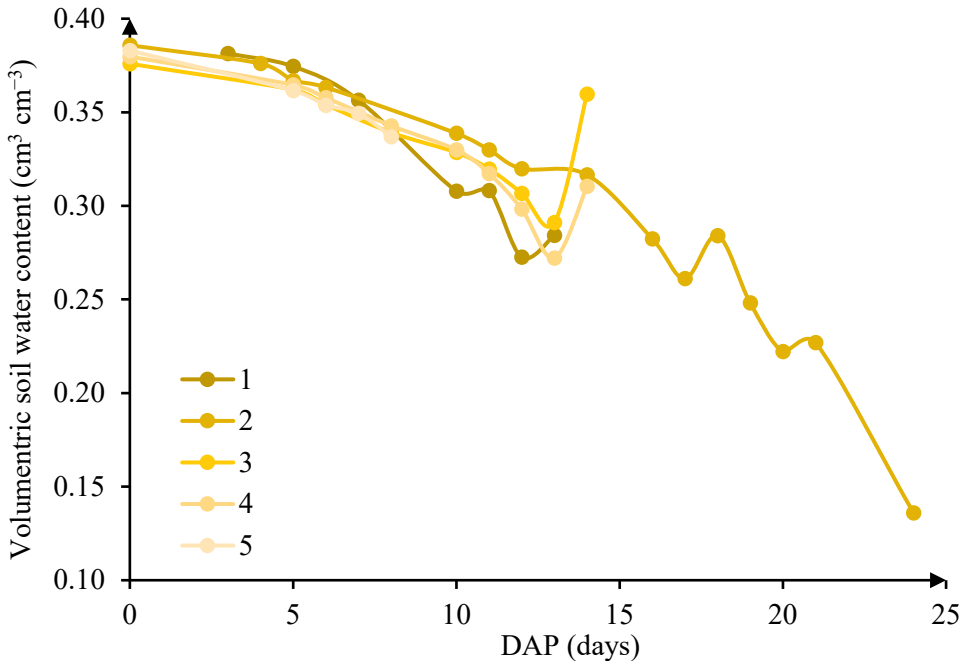


Fig. 4.2: Volumetric soil water content in the five containers of the MRI_{sand} subgroup over the course of the experiment. Points indicate measurements. Increases in soil water content are caused by irrigation.

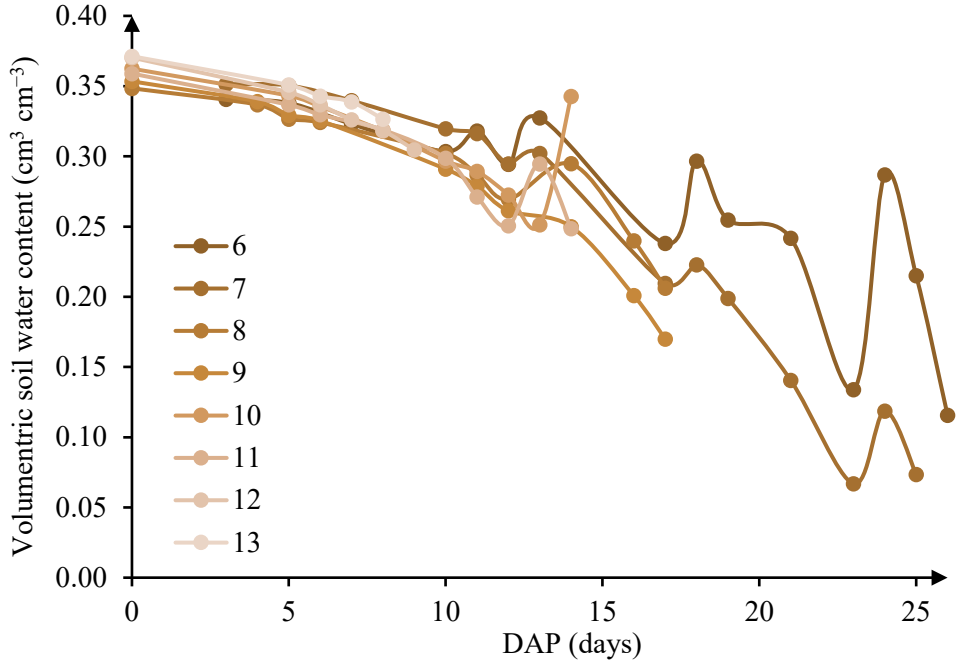


Fig. 4.3: Volumetric soil water content in the eight containers of the MRI_{soil} subgroup over the course of the experiment. Points indicate measurements. Increases in soil water content are caused by irrigation.

Subsequently, the gravimetric soil water content was multiplied by the bulk density of the soil to obtain the volumetric soil water content. Volumetric soil water contents for the sand treatment are displayed in Fig. 4.2, measurements of the soil treatment are shown in Fig. 4.3. The interval between measurements varied between one and five days.

Irrigation

The absolute amount of irrigation, in g day^{-1} , was measured by weighing the containers immediately before and after irrigation was performed. The obtained values were transferred to mm day^{-1} , by scaling them to the soil surface of the cylindrical containers. Fig. 4.4 shows the data collected for the MRI_{sand} subgroup, Fig. 4.5 shows the data for the MRI_{soil} subgroup.

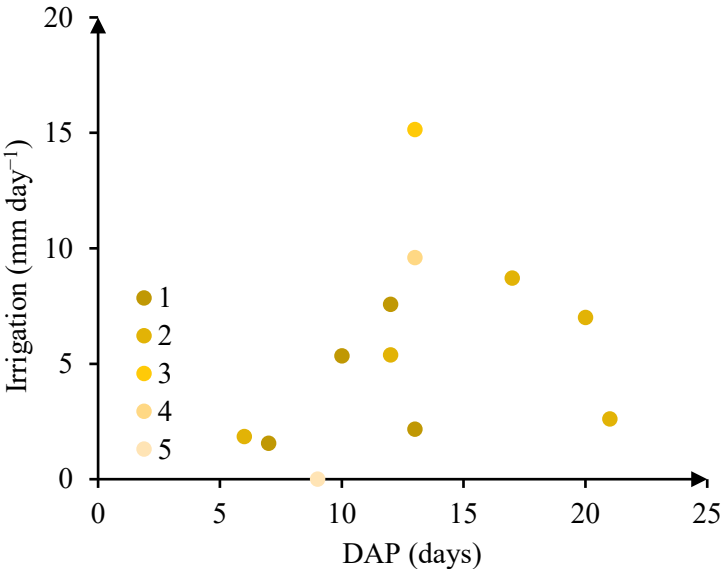


Fig. 4.4: Irrigation schedule for the experimental subgroup MRI_{sand} .

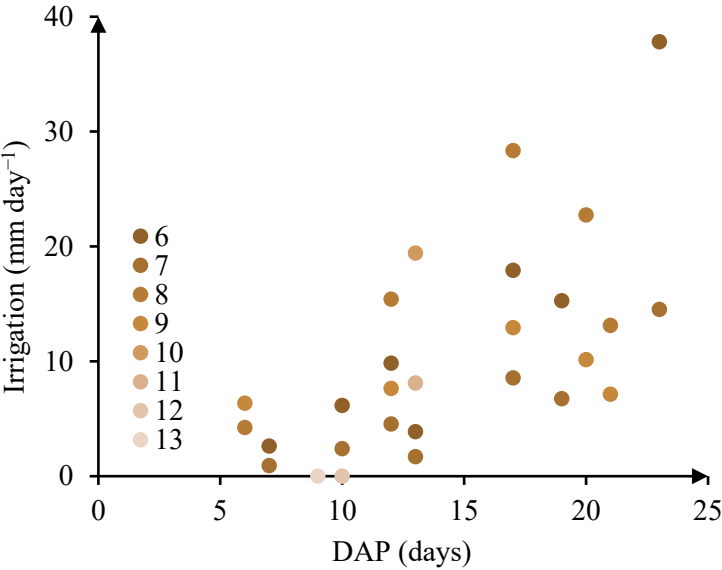


Fig. 4.5: Irrigation schedule for the experimental subgroup MRI_{soil} .

Transpiration

The weight difference of the soil columns between measurements was used to calculate the transpiration rates. This was done under the assumption that the weight loss is only caused by transpiration, and that evaporation from the soil surface (i.e. covered with gravel) can be neglected. If the distance between two measurements was more than one day, the measured difference in soil water was divided by the number of days between the measurement points. Fig. 4.6 displays the calculated transpiration rates for the MRI_{sand} subgroup, Fig. 4.7 displays the calculated transpiration for the MRI_{soil} subgroup.

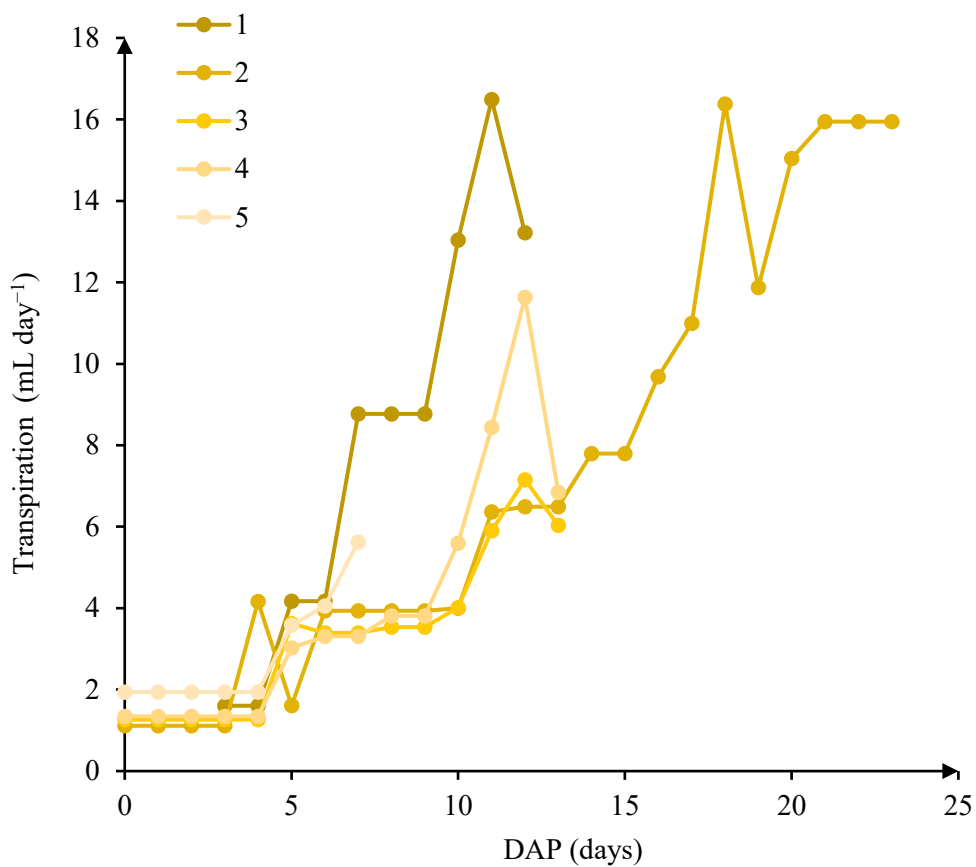


Fig. 4.6: Transpiration rates of plants in the MRI_{sand} treatment over the course of the experiment.

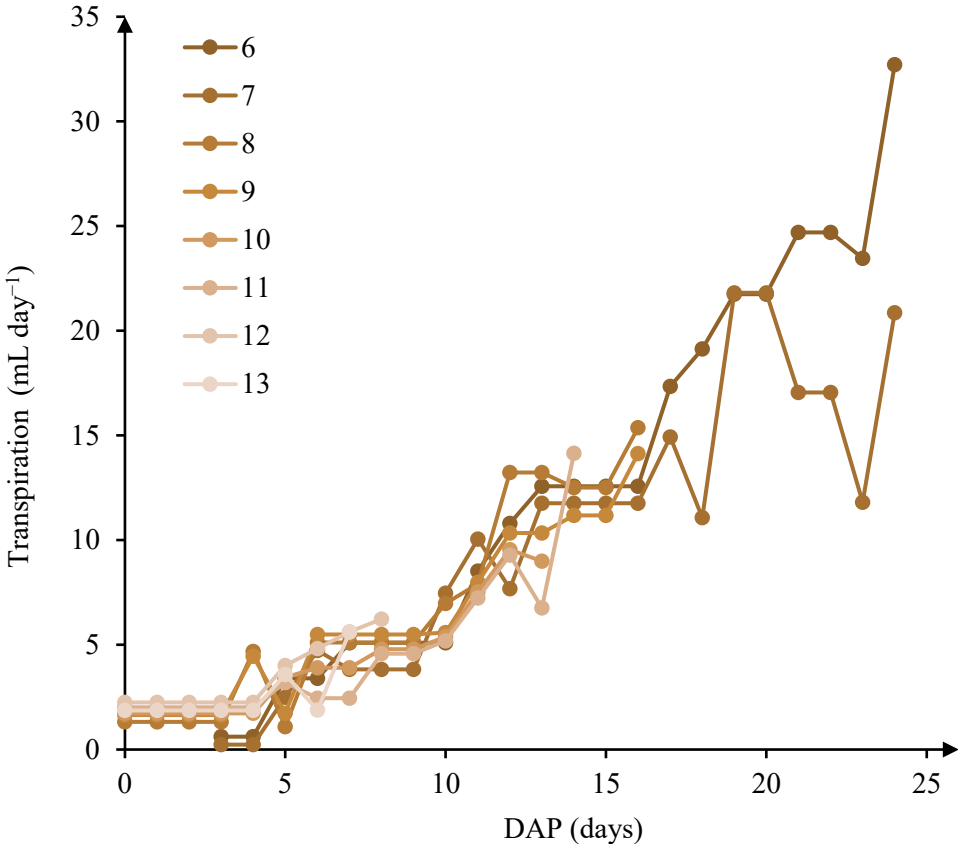


Fig. 4.7: Transpiration rates of plants in the MRI_{soil} treatment over the course of the experiment.

4.3 Model Parameterization

Reconstructing Root System Architectures with Age Distribution

In the first step of model parameterization, we reconstruct the 13 root systems of the MRI time-series scans. We utilize the temporal relationship between the MRI scans, to derive an age distribution for the RSAs. A schematic representation of this method is shown in Fig. 4.8. Each manual reconstruction (Fig. 4.8 a-d) shows the root system at a different root system age.

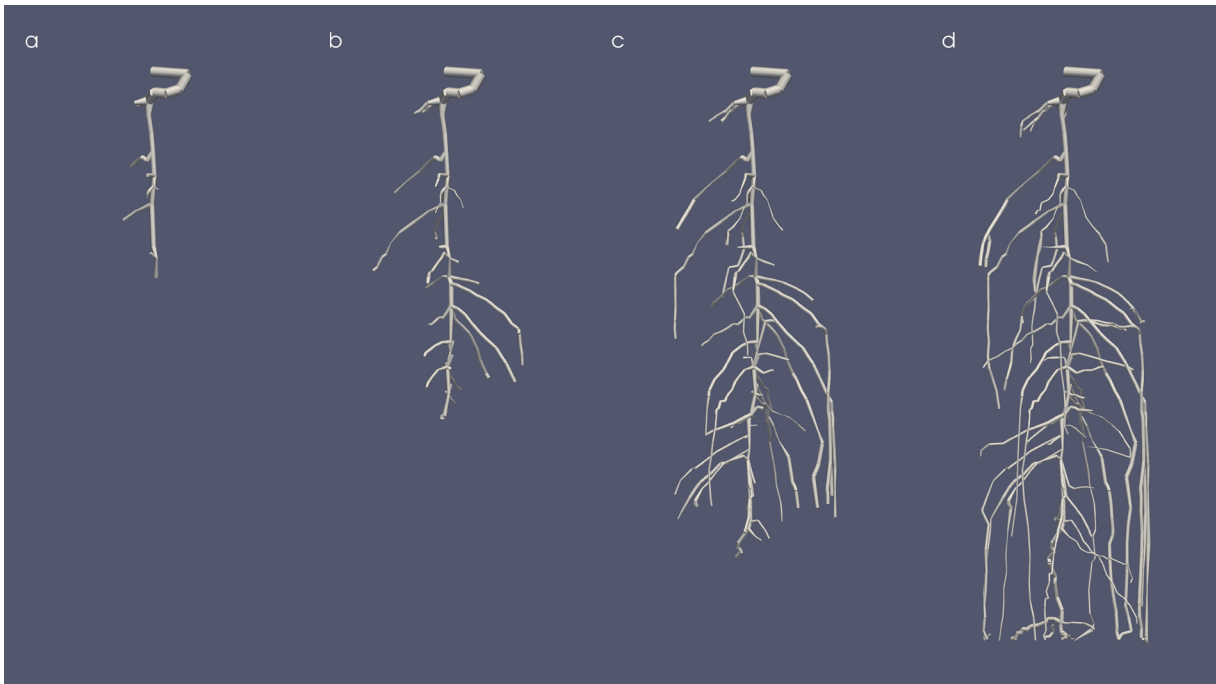


Fig. 4.8: Schematic representation of manual root system reconstructions derived from MRI time-series data at four different root system ages $t_a - t_d$. Root segments are scaled by their respective radius.

We start the manual reconstruction with the oldest MRI image of the root system (Fig. 4.8d). After the reconstruction of the RSA at t_d is finished, we save the result and load the previous scan at t_c . The root system age, t_n , at which the respective MRI scan was performed, is set as the emergence time of the root tips. We now delete all root segments of the reconstruction at t_d , that are not grown yet at t_c . This procedure is repeated until we reach the MRI scan at the youngest root system age t_a . In this example, we retrieve four reconstructions from root system ages t_a to t_d . All gathered 3D-coordinates of the root segments within the soil domain, their radius, and the respective emergence times of the root tips, are then saved in form of RSML

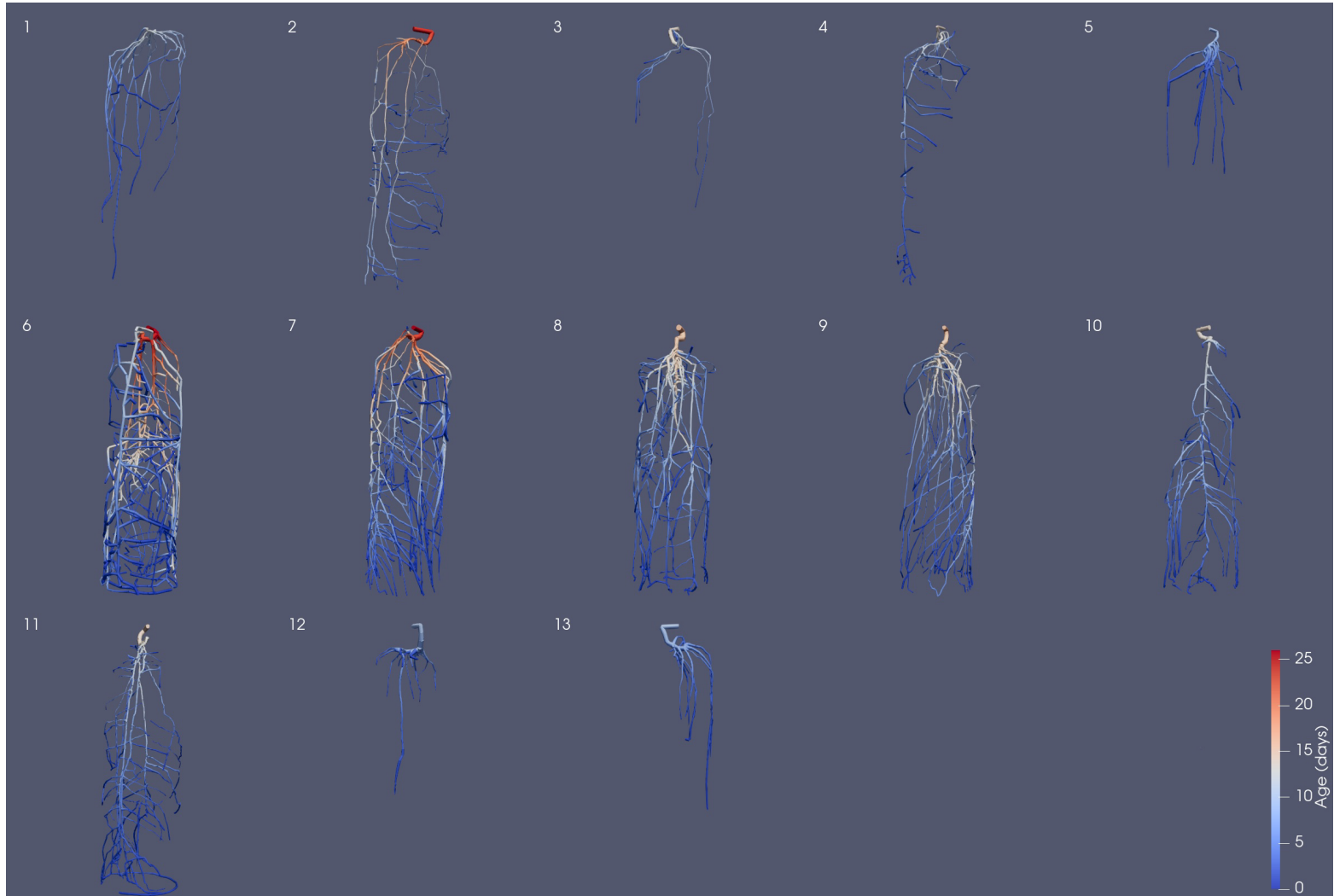


Fig. 4.9: Manual reconstructions of 13 root systems based on MRI time-series. Data includes age information that is interpolated between the respective measurement dates (see Table 4.1). Root segments are scaled by their respective radius and color-coded based on the interpolated age.

files (Lobet et al., 2015). Finally, we combine the four separate RSML files, to create a single RSML file, which includes a root segment age distribution for the whole RSA. This is realized by linear interpolation from the emergence times of the root tips between t_a and t_d . The resulting RSML files for all 13 plants of the experiment are displayed in Fig. 4.9. Note that in this visualization, we display the age distribution of the fully grown root systems at the last MRI measurement date.

Mimicking Root Growth on Static Root System Architectures

The 13 RSAs shown in Fig. 4.9 can now be loaded directly into CPlantBox-DuMu^X and then be used as geometries to simulate RWU from a dynamic soil domain. As we want to simulate RWU from plant establishment to the last MRI measurement, we update the root segment ages in the model via $age_{sim} = age_{seg} - age_{max} + t_{sim}$, where age_{seg} is the segment age saved in the RSML file (see Fig. 4.9), age_{max} is the root system age at the last MRI scan (see Table 4.1),

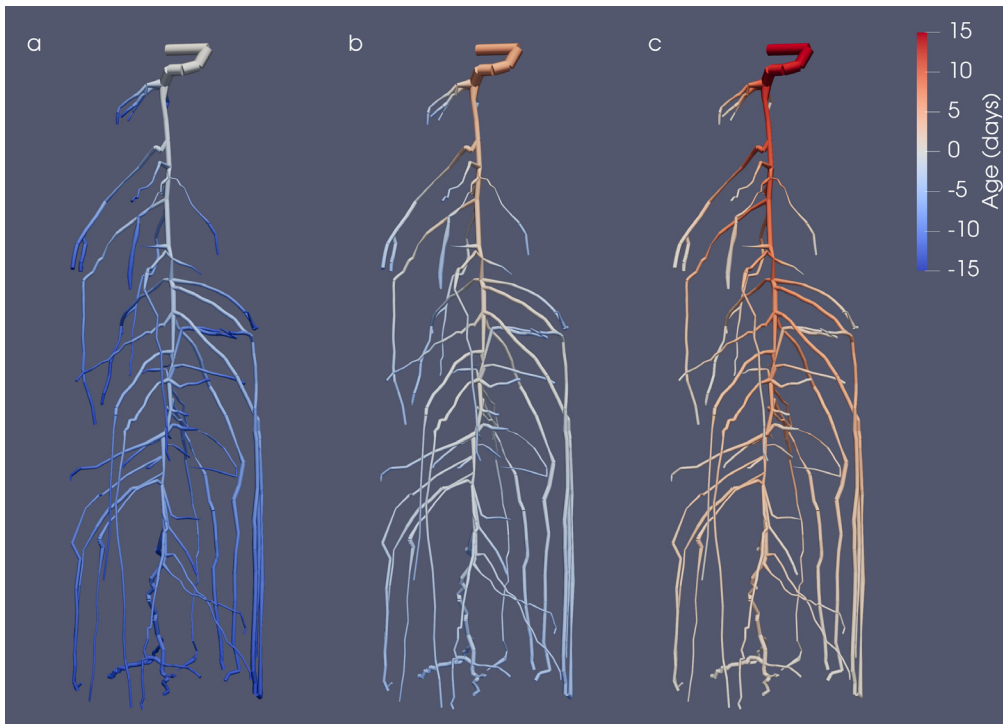


Fig. 4.10: Root system architecture of plant 10 derived by two manual reconstructions of MRI scans. Shown is the segment age (age_{sim}) at simulation times (t_{sim}) of 0.1, 7 and 14 days. Root segments are scaled by their respective radius.

t_{sim} is the current time of the simulation, and age_{sim} is the resulting segment age in the simulation. The resulting age distribution for the exemplary root system of plant 10, during different simulation times (age_{sim}), is displayed in Fig. 4.10. At the start of the simulation (0.1 days, see Fig. 4.10a), only a small fraction of the tap root is grown. Most of the root segments have not yet grown and therefore have a negative age. At the end of the simulation (14 days, see Fig. 4.10c), the whole root system is established. The root collar has an age of 14 days, and all root segment ages are above zero.

Based on the segment ages in the model (see Fig. 4.10), we can now mimic the functional behavior of growing root systems on static RSAs. We realize this, by assigning order and age-dependent root hydraulic properties. The hydraulic conductivities of first and second order roots are parameterized in the model based on values from Zarebanadkouki et al. (2016). Used axial, k_z ($\text{cm}^3 \text{d}^{-1}$), and radial conductance values, k_r (d^{-1}), are displayed in Fig. 4.11. By assigning unborn root segments ($age \leq 0$) a radial conductance of zero, they cannot take up water, and therefore, do not participate in RWU from the soil. Fig. 4.12 and Fig. 4.13 show the resulting k_z and k_r distributions mapped onto root system 10.

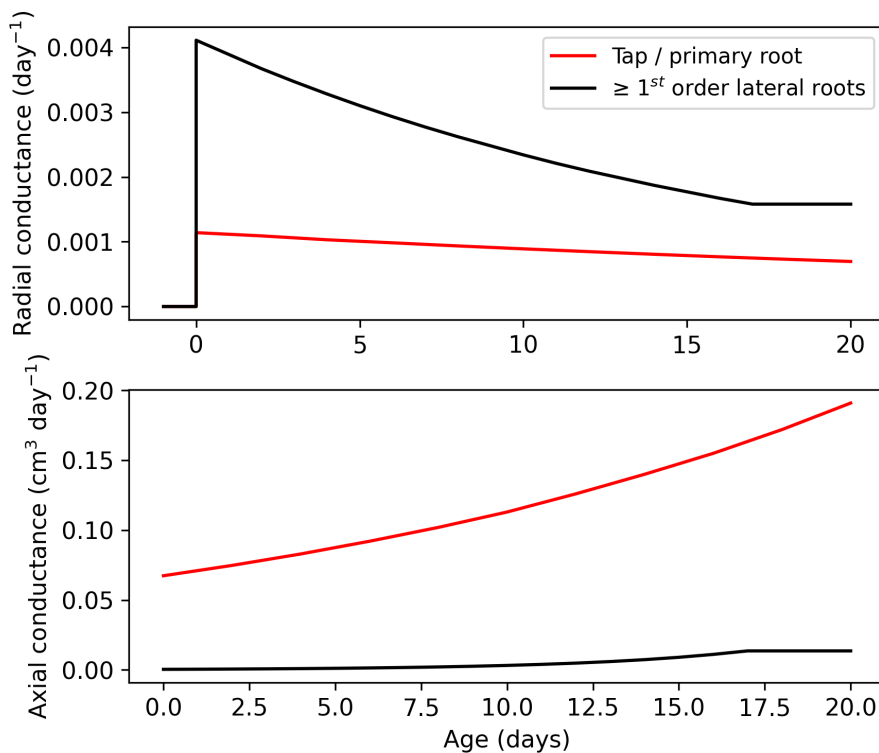


Fig. 4.11: Order and age-dependent root hydraulic conductivity functions used for parameterization.

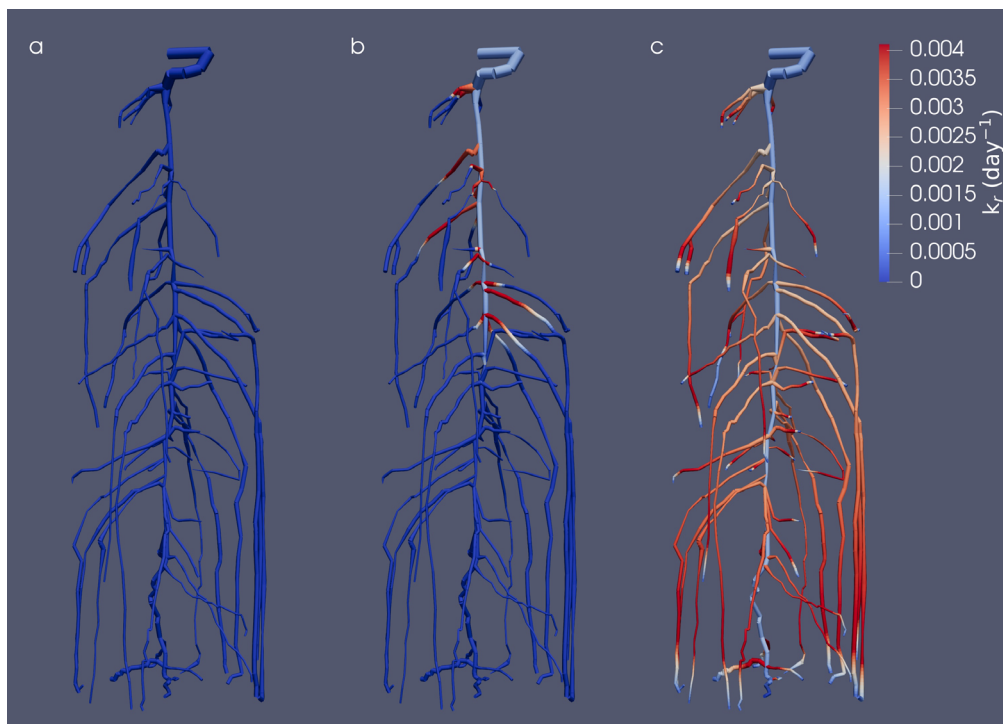


Fig. 4.12: Root system architecture of plant 10 derived by two manual annotations of MRI time-series scans. Shown is the axial conductivity as a function of root system age at simulation times (t_{sim}) of 0.1, 7 and 14 days. Root segments are scaled by their respective radius.

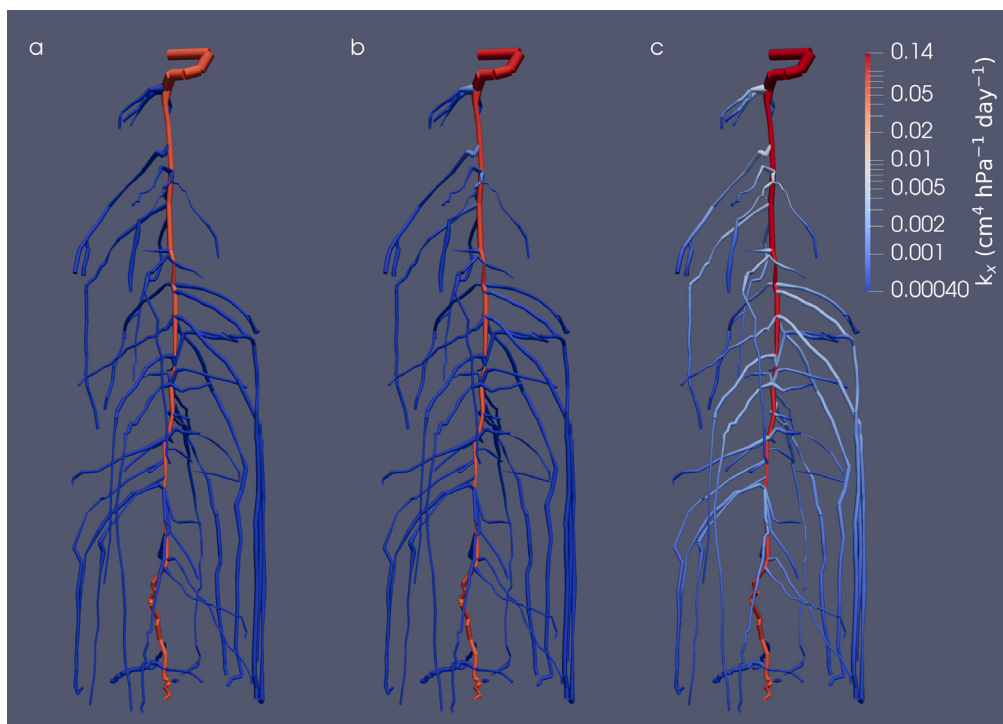


Fig. 4.13: Root system architecture of plant 10 derived by two manual annotations of MRI time-series scans. Shown is the radial conductivity as a function of root system age at simulation times (t_{sim}) of 0.1, 7 and 14 days. Root segments are scaled by their respective radius.

Soil Hydraulic Properties

CPlantBox-DuMu^X characterizes soil hydraulic properties by the van Genuchten model (van Genuchten, 1980). The van Genuchten parameters for the used soil substrates have been determined in past studies and are therefore taken from the literature. Parameters of the Kaldenkirchener soil are taken from Herbst et al. (2016), parameterization of the natural sand was done according to Haber-Pohlmeier et al. (2010). As the bulk density in the containers of the MRI_{sand} group was lower than in Haber-Pohlmeier et al. (2010), the van Genuchten parameters of the sandy soil were adapted to the observed bulk density values with pedotransfer functions (Assouline, 2006a, 2006b). Parameters for both substrates are given in Table 4.2, where θ_r is the residual water content ($\text{cm}^3 \text{cm}^{-3}$), θ_s is the water content at saturation ($\text{cm}^3 \text{cm}^{-3}$), α is related to the inverse of the air entry suction (cm^{-1}), n is a measured estimate of the pore-size distribution (-), and K_s is the saturated hydraulic conductivity of the soil. The resulting soil water retention curves are depicted in Fig. 4.14.

Table 4.2: Soil hydraulic properties of the used soil substrates.

Soil type	θ_r ($\text{cm}^3 \text{cm}^{-3}$)	θ_s ($\text{cm}^3 \text{cm}^{-3}$)	α (cm^{-1})	n (-)	K_s (cm d^{-1})
Sand (FH-31)	0.020	0.39	0.0013	12.70	3909
Sand, adapted	0.018	0.44	0.0093	10.27	6816
Soil	0.015	0.47	0.0271	1.77	100

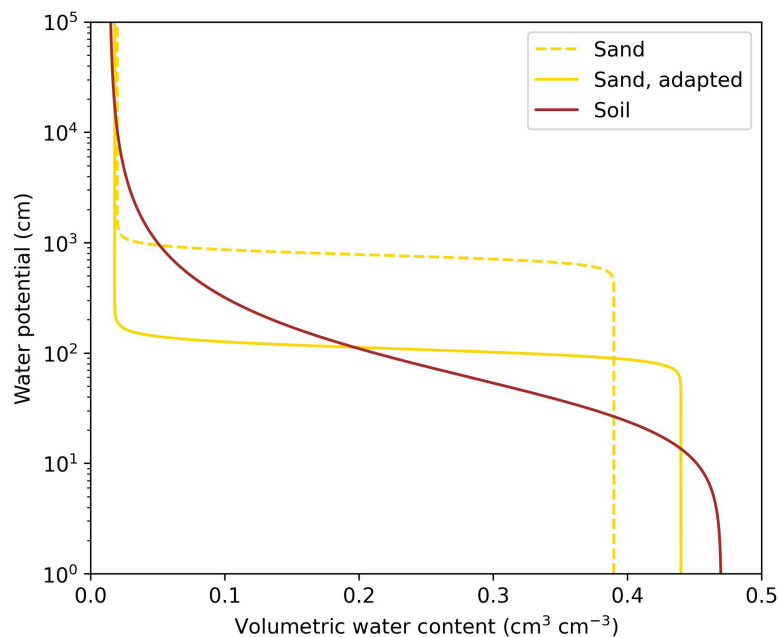


Fig. 4.14: Soil water retention curves of the soil substrates used in the experiment. The used retention curve of sand was adapted to the observed bulk density (Sand, adapted).

Cylindrical Soil Domain and Initial Soil Water Content

CPlantBox-DuMu^X can be used directly to create structured grids consisting of equally sized cuboids to discretize a soil domain of a given size. However, approximating the size of the cylindrical containers that are commonly used in MRI experiments by equally sized voxels, will lead to either over- or underestimation of the experimental soil volume. One way to realize the representation of a cylindrical soil domain in CPlantBox-DuMu^X is to provide an externally created grid in form of a mesh file as input. We use pyGmsh (Schlömer, 2022), which is a python interface for Gmsh (Geuzaine & Remacle, 2009), an open-source grid generator for finite elements, to supply a hybrid grid to the model. Fig. 4.15 shows the hybrid grid itself (Fig. 4.15a), and a root system that is embedded in the cylindrical soil domain (Fig. 4.15b). We chose to use a grid with a structured core, and only use unstructured grid elements (soil voxels of varying volume and shape) in the outer layers of the soil domain, to approximate the cylindrical shape.

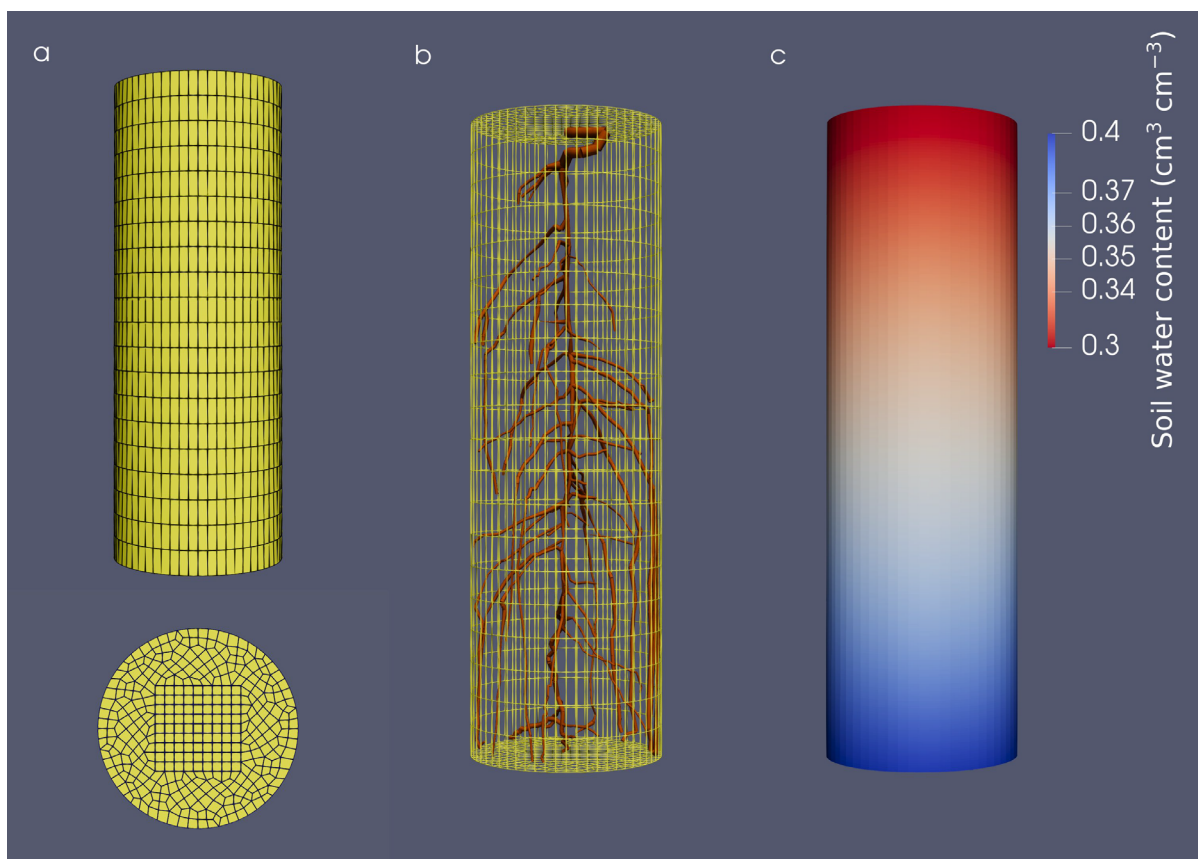


Fig. 4.15: (a): Top and side-view of the hybrid grid used to discretize the cylindrical soil domain, (b): root system of plant 10 embedded in soil domain, (c): initial soil water content distribution at the beginning of the simulation.

This hybrid grid requires less computing power in the simulation than a grid consisting exclusively of unstructured elements. The code for creating the displayed grid is available in Appendix Section C1.

The initial amount of water in the soil domains was parameterized according to the respective measurements at the beginning of the experiment. The recorded values showed mean soil water contents in the range of 0.38 to 0.35 $\text{cm}^3 \text{cm}^{-3}$, which were directly entered into the model input files. We assumed a hydrostatic equilibrium in the soil domain at the start of the simulations. The resulting soil water distribution for the example of root system 10 is shown in Fig. 4.15c.

Irrigation and Transpiration

The irrigation rates in mm day^{-1} (see Fig. 4.4 and Fig. 4.5), are passed to the model in tabular form. To mimic a realistic irrigation event, the irrigation is not spread over a whole day, but concentrated to small time-intervals: hence, irrigation rates are multiplied by 12, but only applied for 2 hours.

Assuming that the recorded soil moisture is unlikely to lead to drought stress for the plants during the course of the experiment, the measured values of T_{act} (see Fig. 4.6 and Fig. 4.7) are defined as T_{pot} rates in the model. A realistic transpiration behavior throughout the day was simulated by introducing an oscillating pattern using a sinusoidal function.

4.4 Model Outputs

Based on the reconstructed RSAs, we can use CPlantBox to derive age-dependent root system metrics of the plants. Fig. 4.16 shows a small selection of common root metrics calculated for the plants grown in sand, Fig. 4.17 shows the same metrics for the plants grown in soil.

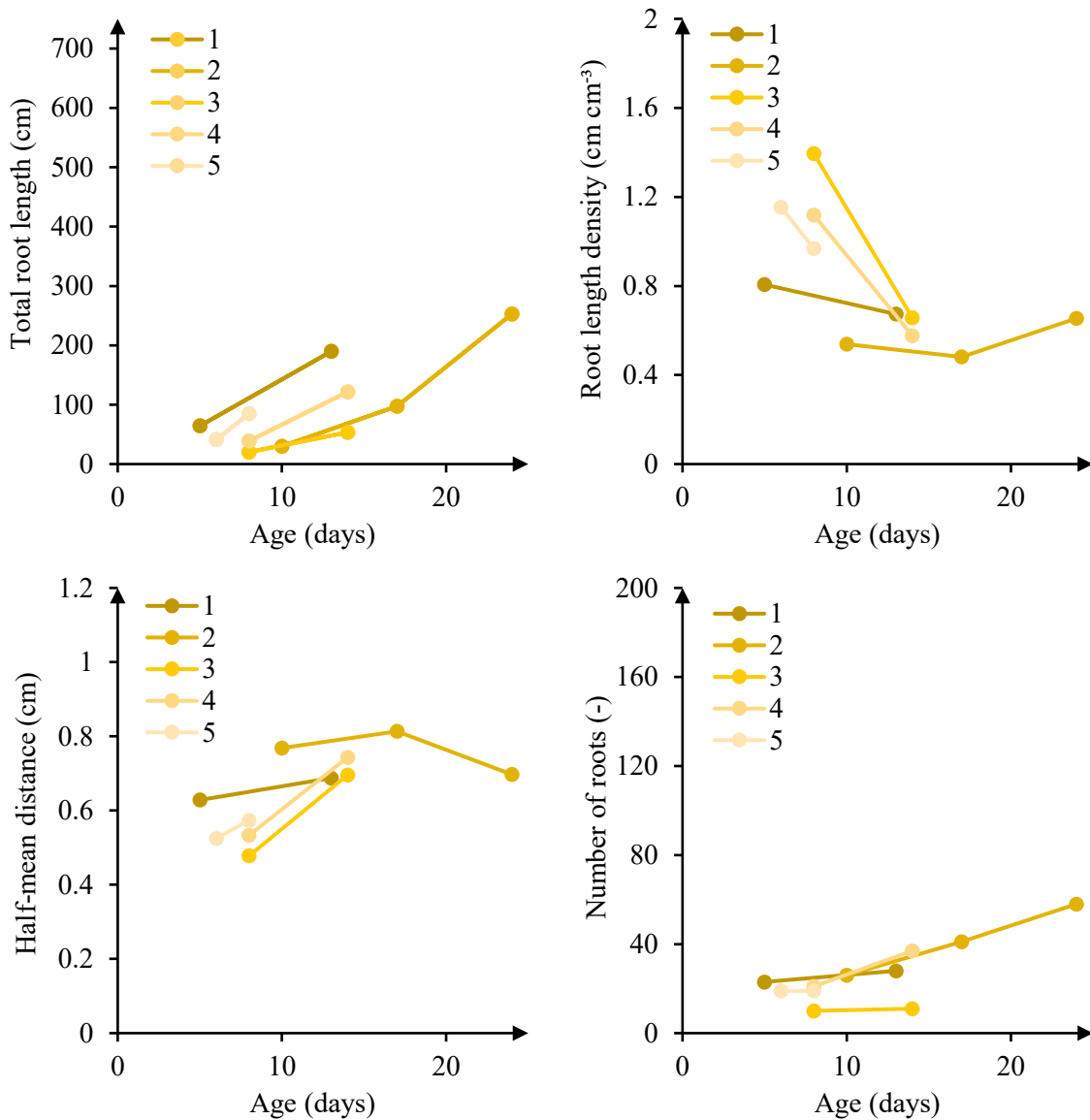


Fig. 4.16: Root system metrics derived from manual reconstructions of MRI time-series scans for the subgroup MRI_{sand}.

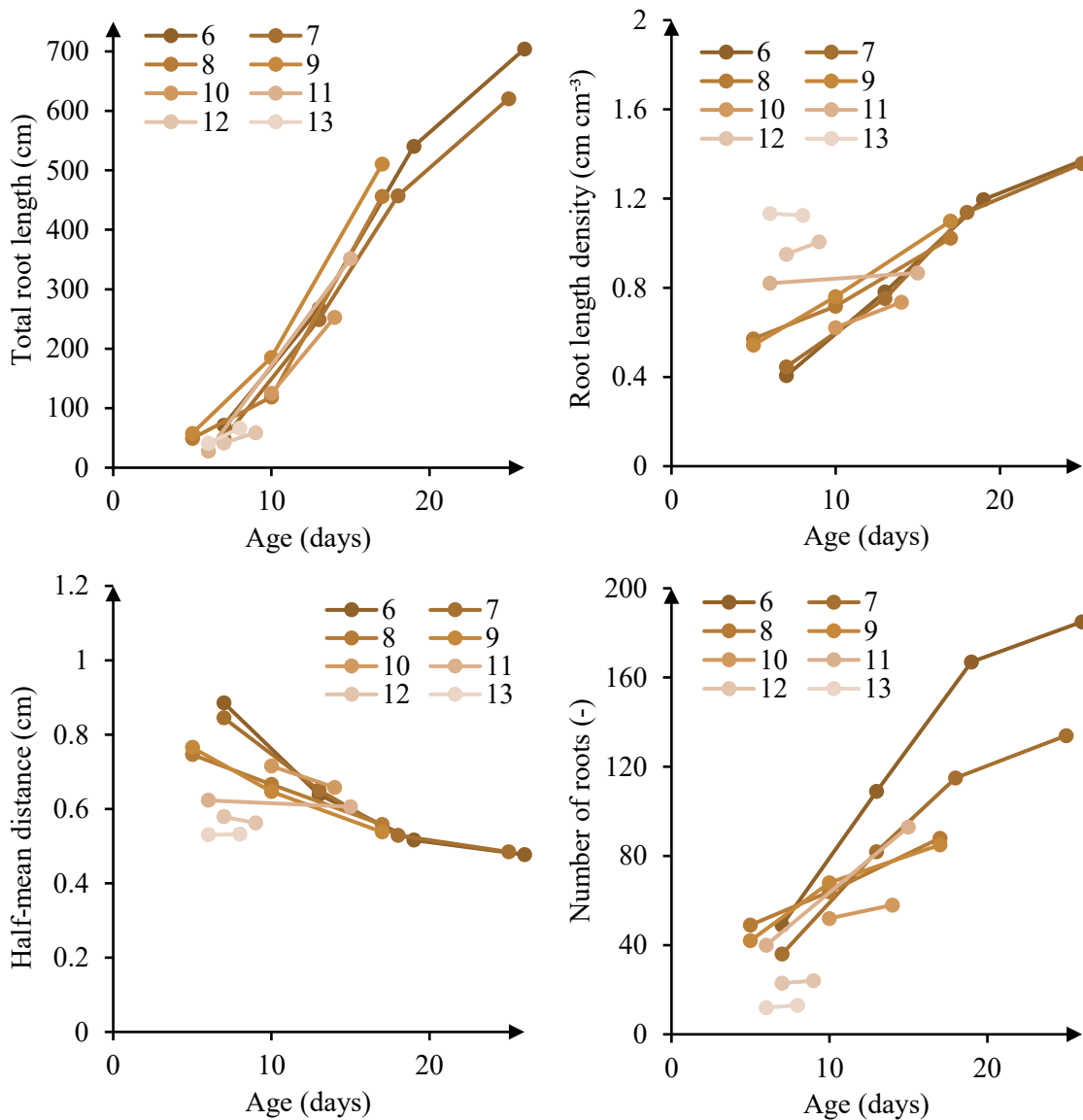


Fig. 4.17: Root system metrics derived from manual reconstructions of MRI time-series scans for the subgroup MRI_{soil}.

It should be noted that the reconstructed time series also enable us to calculate model-based functional root traits that evaluate the hydraulic behavior of the root systems during their development. As shown in Selzner et al. (2023) (see Table 2.3), we can investigate the integrated functional behavior of the whole RSAs in RWU, by calculating the equivalent root system conductance and the standard uptake fraction of roots in static soils.

The fully parameterized CPlantBox-DuMu^X can now be used to calculate RWU from a dynamic soil domain. Fig. 4.18 shows the simulated transpiration rates of plant 10 grown in soil.

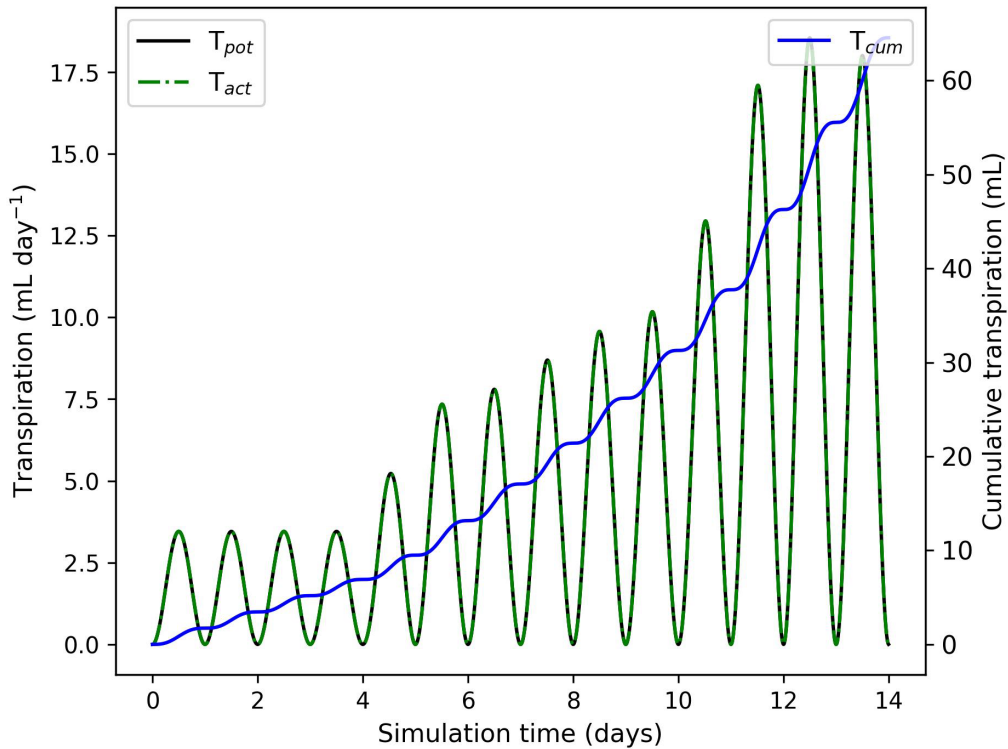


Fig. 4.18: Potential transpiration (T_{pot}), actual transpiration (T_{act}) and cumulative transpiration (T_{cum}) of plant 10 grown in soil.

The diurnal pattern of T_{pot} , which was introduced by applying a sinusoidal function to the measured transpiration values, is shown in black. Based on the simulated T_{act} (green), no reduction in transpiration is simulated by the model. In case the root system could not achieve sufficient water uptake to satisfy the T_{pot} , the onset of drought stress would be indicated by a divergence between T_{act} and T_{pot} . A detailed overview of the behavior of the transpiration curves under drought stress, can be found in Khare et al. (2022) (see also Fig. 3.1 and Fig. 3.2).

In addition to the qualitative information on plant water status displayed in Fig. 4.18, we can also access the xylem water potential to investigate whether a plant is close to potential drought stress. Fig. 4.19 shows the simulated root collar potential of plant 10 over the course of the

experiment. Fig. 4.20 shows the root water pressure distribution of all root segments at selected simulation time points.

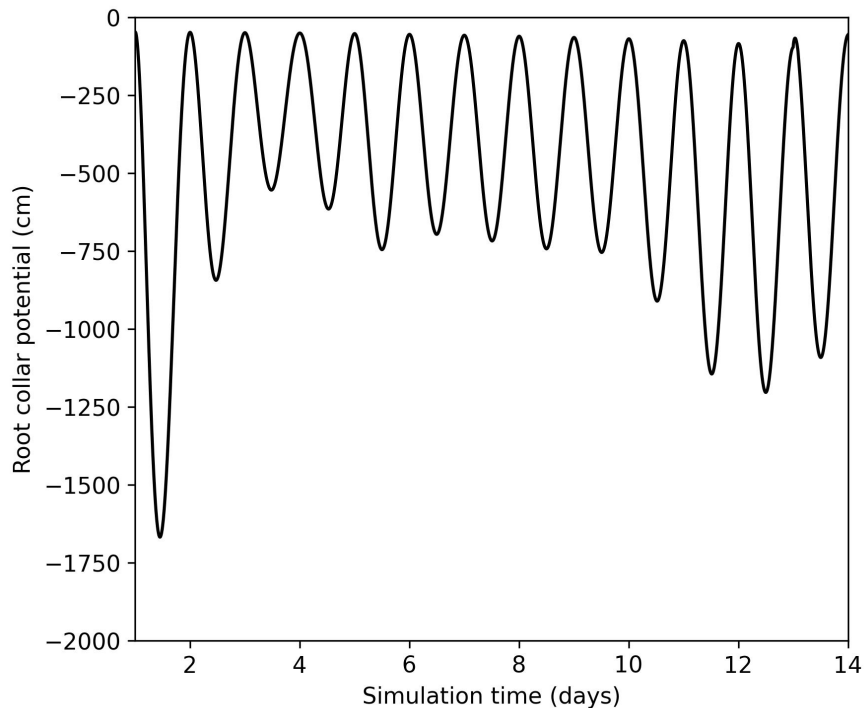


Fig. 4.19: Simulated root collar potential for plant 10 grown in soil.

As we parameterized the commonly used root collar potential of $-15,000$ cm as limiting water potential (Javaux et al., 2008; Schnepf et al., 2023), we can observe that the simulated plant is at no point close to being draught stressed (minimal collar potential of $\approx -1,800$ cm at day 1).

In this chapter we have shown how replications of growing root systems can be parameterized and performed in CPlantBox-DuMu^X. The data-driven repetition of MRI experiments with FSRM allows us to link RSAs and their functioning in RWU with root development over time. The virtual repetitions become increasingly useful, when additional data on the spatial distribution of soil water are available (e.g. as in Haber-Pohlmeier et al., 2010; Koch et al., 2019; Koebernick et al., 2015; Tötze et al., 2021). Such data can then be used in comparisons with the simulated soil water distributions, to aid us in validating modelling mechanics and modelling assumptions.

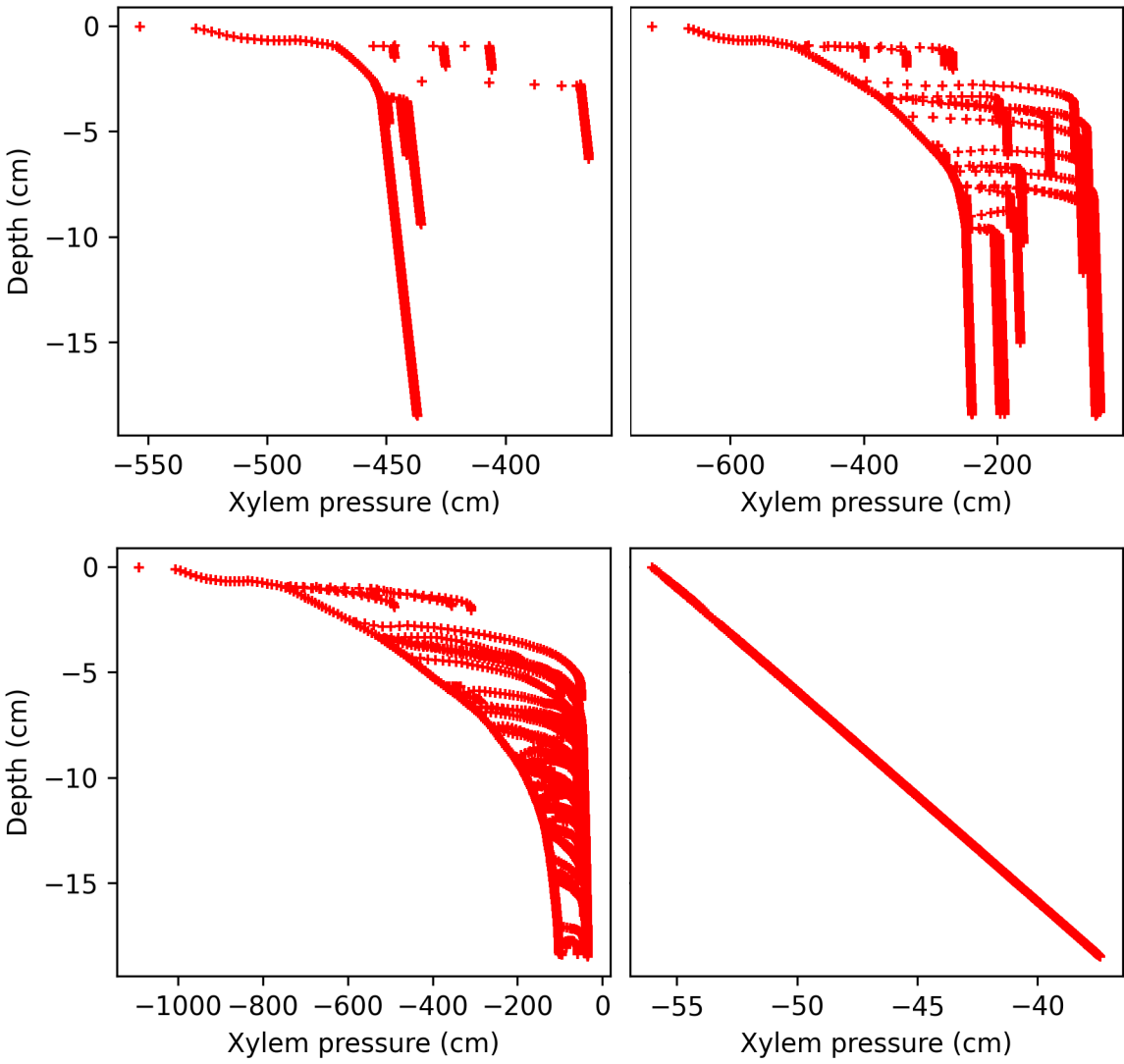


Fig. 4.20: Xylem water potential of all root segments of plant 10 during peak transpiration at day 3.5 (upper left), 7.5 (upper right), 13.5 (lower left) and during the night of day 14 (lower right).

Chapter V

Conclusions and Outlook

5.1 Conclusions

Root analysis methods, including models, can help our effort to breed varieties that can cope with adverse growing conditions to mitigate the potentially devastating effects of climate change on crop production and global food security. Even at the status quo, we need to move towards more sustainable practices to avoid additional environmental damage and overexploitation of natural resources. Optimizing the RSA of crops offers great potential to help shift agricultural production towards more sustainable practices. To optimize the RSA, we first need to understand it. With the help of volumetric imaging, we can derive high quality RSAs and describe their development over time. The derived RSAs can then be used in FSRM to study the interaction between roots and their (soil) environment. However, the processing of volumetric images and their incorporation into FSRMs is a challenging task that has limited the efficient use of the derived data to date.

In this work, we investigated how MRI images can be used more efficiently, and how MRI experiments can be incorporated into FSRM to help us to gain an advanced understanding of the SPAC. The main objectives were: to improve the current workflow of RSA reconstruction from MRI images (Chapter II), to investigate if the current soil process descriptions in FSRM are adequate to derive realistic RWU predictions of RSAs derived from MRI images (Chapter III), and to develop parameterization methods that allow holistic and precise virtual replications of MRI experiments in FSRM (Chapter IV).

Chapter II presents a novel state-of-the-art workflow, which leverages a 3D U-Net for semantic image segmentation in combination with automated and manual root system reconstruction methods, to derive RSAs from MRI images. We could show that the approach allows us to process MRI images more efficiently, and to recover larger fractions of roots from MRI images. The standardization of the segmentation procedure should greatly decrease human reconstruction bias. In addition, we can now apply automated reconstruction approaches to MRI images of low CNR. The current methodological paradigm of limiting experiments to a set of environmental conditions that are optimal for obtaining high quality images, but which are insufficient for studying phenotypic responses to a wide range of environments, is being challenged by the demonstrated advances.

The study presented in Chapter III highlights that coarse soil grid resolutions in RSS models of RWU are not able to spatially resolve the steep soil water potential gradients near plant roots during water uptake. We were able to show that results for dry conditions obtained with RSS models of RWU can contain significant errors and must therefore be interpreted with caution. At present, the associated errors are often underestimated or neglected. We believe there is an urgent need to adapt our RWU modelling paradigms to drought conditions. More advanced models (i.e. models that operate on similar principles as the continuum multi-scale model) need to become the standard modelling approach to derive accurate results for dry conditions in a computationally efficient manner. While we move towards models with more detailed descriptions of soil processes, we must be aware of potential systematic gaps between process descriptions and measurement methods. Although we have been able to increase the recovery rates from MRI images, RSAs derived from volumetric images commonly still miss a significant fraction of roots. If the derived geometries are used to simulate RWU with advanced modelling approaches, such as the multi-scale model, the missing roots could lead to a systematic underestimation of RWU (Khare et al., 2022).

Chapter IV showcases the workflow of incorporating RSAs derived from MRI images, in combination with additional experimental data, to enable a virtual repetition of MRI experiments in FSRM (i.e. CPlantBox-DuMu^X). We reconstruct RSAs that contain interpolated information on the root age, based on MRI time-series scans. This allows us to calculate root system metrics at different stages of plant development. Such age-dependent root system metrics are very useful for parameterizing the RSA submodules of FSRM. The improved RSA reconstruction workflow will facilitate the parameterization of RSA submodels based on time-dependent measurements of root system metrics. In addition, we introduce a parameterization method that is suitable to reflect the age- and order-dependent functional behavior of growing root systems. By combining this functional representation of growing root systems with experimental data on irrigation, transpiration, soil water content, and soil hydraulic properties, we created a parameterization framework that allows a data-driven simulation of the observed RWU. The parameterization workflow can be applied to model the resulting soil water distributions and to compare them to experimental observations. We have therefore refined our options for validating the modelling mechanics and assumptions connected to RWU.

5.2 Outlook

At present, we did not apply the novel workflow for root system reconstruction to MRI time-series data. However, this data should help us to further improve the algorithm for automated reconstruction. By exploiting the relatively simple structure of young root systems, the algorithm should be able to derive an automated reconstruction in which the topology of the roots is mostly correct. This should also defuse the problem of temporal fluctuation in image quality, which is prone to result in root gaps. Based on this initial high-quality reconstruction, the algorithm could be directed to extend the reconstruction only by the additional root growth that occurred between two consecutive MRI scans. By repeating this process for all images in the time-series, information on root topology and connectivity that was determined at unambiguous stages of root system development would be preserved, and automated reconstruction quality should increase by a large margin. To boost the efficiency of MRI image processing once again, a hybrid workflow seems promising. Such a hybrid workflow could leverage the automated reconstruction as a scaffold, which can then be manually corrected in the VR application. Instead of performing a complete root system reconstruction, the human reconstructor would only need to detect and correct errors in the automated reconstruction, until a satisfactory quality is reached. In addition, the reconstructed RSAs still miss a significant fraction of roots. A potential solution to increase root recovery could be based on virtual root system completion. By comparing WinRHIZO measurements with reconstructed RSAs, we can characterize the missing root fraction. This information on the missing fraction (i.e. order, radius, length), can then be leveraged to instruct CPlantBox-DuMu^X to complete the reconstructions. The virtual root system completion should significantly reduce errors in deriving root architectural parameters for the use in RSA submodules of FSRMs, and in RWU calculations that use the RSAs as direct geometries. This is especially true for advanced RWU modelling approaches, such as the herein presented multi-scale model, which otherwise may significantly underestimate RWU.

We were able to demonstrate that the multi-scale model provides a better description of rhizosphere soil processes than RSS approaches, while being fast and accurate. However, it is still debatable if the multi-scale model itself leads to more realistic RWU predictions. It has been shown that biophysical processes, such as mucilage deposition and rhizosphere

compaction, can heavily alter soil hydraulic properties in the rhizosphere (Kroener et al., 2014; Landl et al., 2021). In the presented work, we did not assign different soil hydraulic properties to the rhizosphere and the bulk soil. These processes, however, could at least partially counteract the strong k_{soil} soil gradients. Hence, it is vital to integrate and to investigate these biophysical processes in the framework of the multi-scale model. The validation and parameterization of biophysical processes could be facilitated by MRI experiments and their virtual replications in the model. To this end, the demonstrated workflow for integrating MRI experiments into CPlantBox-DuMu^X is well suited to perform data-driven virtual repetitions.

Appendix A

A1 MRI Experiment and Image Processing

A1.1 Experimental Description

The MRI scans used in this work were gathered in an experiment carried out at the Forschungszentrum Juelich. Eight seeds of white lupine (*Lupinus albus*) were germinated on wet paper for four days and planted into two different soil substrates: four seedlings were planted into PVC cylinders filled with a sandy loam and four seedlings were planted into cylinders containing natural sand. The sandy loam was taken from the topsoil of an agricultural field close to Kaldenkirchen, Germany, with a texture of 73% sand, 23% silt and 4% clay, a soil organic carbon content of $0.85 \text{ g } 100 \text{ g}^{-1}$ and a small fraction ($< 0.0025 \text{ g g}^{-1}$) of ferromagnetic particles (Pohlmeier et al., 2009). It was dried and sieved to 2 mm and is denoted as “soil”. The natural sand had a mean grain size of approximately 0.3 mm (FH-31, Quarzwerke Frechen GmbH, Frechen, Germany) and is denoted as “sand”. Used cylinders were 21 cm in height, had an inner diameter of 5.6 cm, and were filled with the respective soil substrate up to a height of 18.5 cm. Additionally, a marker tube filled with 80:20 D₂O/H₂O (w/w) was inserted into each cylinder, which was used later to normalize voxel intensities of the MRI images. To prevent evaporation, a layer of coarse gravel was used as a capillary barrier at the soil surface. The cylinders were perforated at the bottom and the holes were covered with a nylon mesh. Subsequently, the substrate-filled cylinders were saturated from the bottom to saturation soil water contents of $0.36 \text{ cm}^3 \text{ cm}^{-3}$ for soil and $0.38 \text{ cm}^3 \text{ cm}^{-3}$ for sand. Water contents were measured gravimetrically and converted to volumetric water contents via the soil volume. Bulk densities ranged between 1.45 and 1.49 g cm^{-3} for sand, and 1.39 and 1.42 g cm^{-3} for soil. Plants were grown for 8 to 15 days in a laboratory at a relative humidity of approximately 45%, a temperature of approximately 25°C and a day-night cycle of 12h/12h. Photosynthetic active radiation during the day was $450 \pm 50 \mu\text{mol m}^{-2} \text{ s}^{-1}$. Irrigation was performed with tap water, consistently every second to third day from the top with a syringe to compensate for half of the transpiration loss. For the plants grown in sand, the tap water was additionally mixed with half strength Hoagland nutrient solution. The experimental containers were scanned by MRI at different time points (Table 2.1). At the end of the experiment, the roots were excavated

and washed. They were then scanned with an Epson flatbed scanner with a resolution of 0.005 mm in horizontal, and 0.01 mm in vertical direction. The scans were analyzed with WinRHIZO (Regent Instruments, Ottawa, Canada) to determine total root length.

A1.2 MRI Image Processing

All pre-analysis image-processing steps of the MRI scans were performed using MATLAB (The MathWorks Inc., Cambridge, UK). Due to the gradient non-linearity artefact in our MRI system, the raw MRI scans showed systematic distortions increasing from the center line in both vertical directions. We built a calibration phantom using the same PVC cylinders as in the experiment with soil-grown lupine plants, which was filled with sand, as well as four marker tubes that were filled with 80:20 D₂O/H₂O (w/w). The phantom was then scanned using the same setup (sequence, resolution). The undistorted center slice of the scanned MRI phantom stack was used as reference slice. Using affine transformation, each horizontal slice up and down the center slice was registered to the reference slice and dewarped. The generated transformation matrices were subsequently used to de-warp the MRI lupine scans slice-by-slice. As mentioned before, each column was scanned in three sections with an overlap between 5 and 10 mm. These scans were subsequently stitched together using the following approach: first, we normalized the voxel intensities of the different sections using the intensities of the marker tube as a reference. Next, we determined the two overlapping slices of two neighboring sections using the criteria of maximal correlation. The overlapping slice of the lower section was then mapped to the overlapping slice of the upper section using an affine transformation. All remaining slices of the lower section were then equally registered with the slice above using the same transformation matrix. Finally, the three sections were concatenated. Subsequently, the connected structure of the marker tube was masked and excluded from the MRI scans. The images pre-processed in this way were the starting point for the three root reconstruction workflows examined in this paper (Fig. 2.1).

A2 Modifications to Automated Reconstruction Algorithm

A2.1 Modification to Dijkstra's Shortest Path Algorithm

To allow a more complete extraction of roots from imperfect data (i.e. data with gaps), Dijkstra's shortest path algorithm (Dijkstra, 1959) is modified. The path-cost threshold is momentarily ignored to allow the exploration of high-cost voxels within the maximum gap length. Allowing such traversals requires a new cost-map, as using the initial cost-map (Fig. 2.3b) would result in the emergence of multiple high-cost paths from disconnected segments of the same root. Hence, the initial cost-map is adapted when using the gap closing option: voxels below the given minimum intensity threshold are not excluded from the cost map, but their cost is increased by a factor of ten (Fig. 2.3c). Subsequently, all voxels above half of the maximum voxel cost are considered as potential gaps. This preserves low intensity information while simultaneously enhancing the contrast between gap and no-gap voxels. Penalizing these low-intensity voxels also ensures that the shortest path algorithm explores no-gap positions before considering gap positions. When the shortest path algorithm arrives at a no-gap position, where all adjacent voxels are classified as gap positions, it explores all voxels within the predefined maximum gap length. If a voxel classified as no-gap position can be found within this perimeter, it is assumed that the gap positions between the two no-gap positions is caused by missing root information and the gap is bridged. The cost of the path that traverses the gap is adjusted, because it is assumed that it should have crossed a missing lower-cost area. Since the adjusted path cost is now below the path-cost threshold, the gap separating the root segments is closed and exploration continues at the found no-gap position on the other side of the gap.

A2.2 Modification to the 3D Curve Skeletonization Algorithm

In the second stage of the automated reconstruction algorithm a modified version of the 3D curve skeletonization algorithm described in Jin et al. (Jin et al., 2016) is used to extract a root structure graph. A radius estimate map is extracted from the largest connected component (Fig. 2.3d). This is used as basis for another cost map used for the Dijkstra's shortest path algorithm (Dijkstra, 1959). Larger radius estimates result in lower traversal cost. Local maxima in the radius-estimate map are extracted. These quench-points are used as potential root tips and sorted by their respective distance to the selected shoot position, starting with the farthest point. If unused quench points are available, a connection is made between the shoot and the topmost quench point in the list. This connection is made along the shortest path, according to the radius-based cost map. The resulting connection follows the path of highest radius estimate and should therefore follow the center of the segmented root. Quench points in the vicinity of this extracted path are identified based on an enlarged radius search along the path and deleted from the list. Not starting connections in a tube around paths reduces the number of wrong subbranches from noisy data. If an already extracted branch is reached, the current extraction is connected to the existing root graph. The resulting root graph contains a node for each connected voxel. To reduce the number of nodes, the Douglas-Peucker algorithm (Douglas & Peucker, 1973) is used. Radius estimates for each node are taken from the generated radius map. Root parameters are computed based on this radius estimate and the voxel size of the data.

A3 Calculation of Quantitative Measures

RL (cm) denotes the total root length of a root system. The root length density, RLD (cm cm^{-3}), is calculated based on the soil volume in the container V_c :

$$RLD = \frac{RL}{V_c} \quad (\text{A1})$$

For the MRI experiment, V_c was 455 cm³. The half-mean-distance between roots, HMD (cm), is also based on the root length per soil volume in the container and approximated following the classical approach proposed by Newman (1969):

$$HMD = (\pi \times RLD)^{-\frac{1}{2}} \quad (A2)$$

We calculate the mean radius of a root system as

$$r_{mean} = \sum_{i=0}^n \frac{l_i}{RL} r_i, \quad (A3)$$

where r_i is the radius of a root segment, l_i is the length of a root segment, and n is the total number of root segments of a given root system.

The total number of root tips per tracing, as well as the number of lateral root tips is given as a topology measure. Here, we specify lateral tips up to the highest order observed in the manual reconstructions (3rd order lateral roots). Although lateral roots above 3rd order are recorded in the automatic tracings, we refrain from stating them in the root measures results section for improved readability. Laterals above 3rd order are qualitatively accessible in the visual comparisons.

We compute the equivalent conductance of the root system, K_{rs} (cm² d⁻¹), according to Meunier et al. (2017) as

$$K_{rs} = \frac{T_{act}}{\Psi_{RSI} - \Psi_{collar}} K_{rs}, \quad (A4)$$

where T_{act} (cm³ day⁻¹) is the actual transpiration rate, Ψ_{RSI} (cm) is the mean soil water potential at the root-soil interfaces, and Ψ_{collar} (cm) is the water potential at the root collar. We chose a scenario where Ψ_{collar} is set to -15,000 cm, applied as Dirichlet boundary condition, and Ψ_{RSI} is set to -500 cm at the soil surface, while assuming a hydrostatic equilibrium in the soil domain. K_{rs} reflects the ability of a root system to take up a certain water volume under a given water potential difference between root

collar and soil. T_{act} results from solving water flow in the roots according to Meunier et al. (2017). We calculate the root xylem potential of each root segment and use it to derive the respective radial volumetric flow ($\text{cm}^3 \text{ day}^{-1}$). Finally, summation of the radial flows yields T_{act} .

The standard uptake fraction of a root segment, SUF_i (-), indicates its relative contribution to T_{act} and is calculated via

$$SUF_i = \frac{J_r}{T_{act}}, \quad (\text{A5})$$

where J_r is the radial water flux into a root segment ($\text{cm}^3 \text{ day}^{-1}$). To obtain an aggregated (scalar) metric, we determine the mean depth of standard RWU, $zSUF$ (cm), by

$$zSUF = \sum_{i=0}^n z_i \times SUF_i, \quad (\text{A6})$$

where z_i (cm) is the respective depth of a root segment.

Finally, we investigate in how far the root hydraulic properties affect the impact of differences in tracings of the three reconstruction methods on root system function metrics. In the first scenario, called constant scenario, we calculate the metrics by applying the same fixed axial and radial conductivities to all roots. Based on Zarebanadkouki et al. (2016), we apply a fixed axial conductivity of $k_z = 4.32e^{-2} (\text{cm}^3 \text{ d}^{-1})$ and a fixed radial conductivity of $k_r = 1.73e^{-4} \text{ d}^{-1}$ to all roots. For the second scenario, called variable scenario, we apply order and age-dependent root hydraulic properties. As we did not reconstruct time-series, we linearly interpolate root segment ages as a function of root length while assuming a daily growth rate of 1 cm. A resulting age distribution for an exemplary 14-day old root system is shown in Fig. A.1. Parameterized conductivity values are again based on Zarebanadkouki et al. (2016) and depicted in Fig. A.2. We compute the functional metrics for the constant scenario (K_{rsc} , $zSUF_c$), as well as for the variable scenario (K_{rsv} , $zSUF_v$).

Three additional measures, not directly related to the RSAs, are included in the results section to enable a more in-depth classification of the results. The available root length

information from WinRHIZO measurements, RL_{WR} , is used to calculate the recovery rate, RR (%), of a respective tracing:

$$RR = \frac{RL}{RL_{WR}} \times 100 \quad (A7)$$

For the M and M+ reconstructions, we also report the respective reconstruction speed, v_r (cm root min^{-1}), which is calculated as

$$v_r = \frac{t_r}{RL}, \quad (A8)$$

where t_r (min) is the total time required to trace a root system. Division by the respective RL is done to mitigate differences in total root length on t_r between M and M+ reconstructions.

To give an estimate of the quality of the MRI images, we calculate an exemplary CNR (-) for the raw images. The raw data is loaded into Fiji (Schindelin et al., 2012) and an image slice roughly located at medium depth of the experimental containers (-10 cm) is used to manually place a circular selection around the area of the layer with highest, homogeneous signal intensity I_s (-), i.e. the root center of the thickest root. A second circular selection is placed around a soil region containing background noise of intensity I_B , i.e. the largest possible area of the soil cylinder slice that does not contain roots. The mean intensities of the two areas are used to calculate the CNR as

$$CNR = \frac{I_s - I_B}{\sigma_{I_B}} \times 100, \quad (A9)$$

where σ_{I_B} is the standard deviation of I_B .



Fig. A.1: Age-distribution used to assign age-dependent root hydraulic conductivities to manual tracings M (left), manual tracings based on segmented images M+ (middle), and automated tracings A (right). Shown is an exemplary 14-day old *Lupinus albus* root system of the MRI dataset.

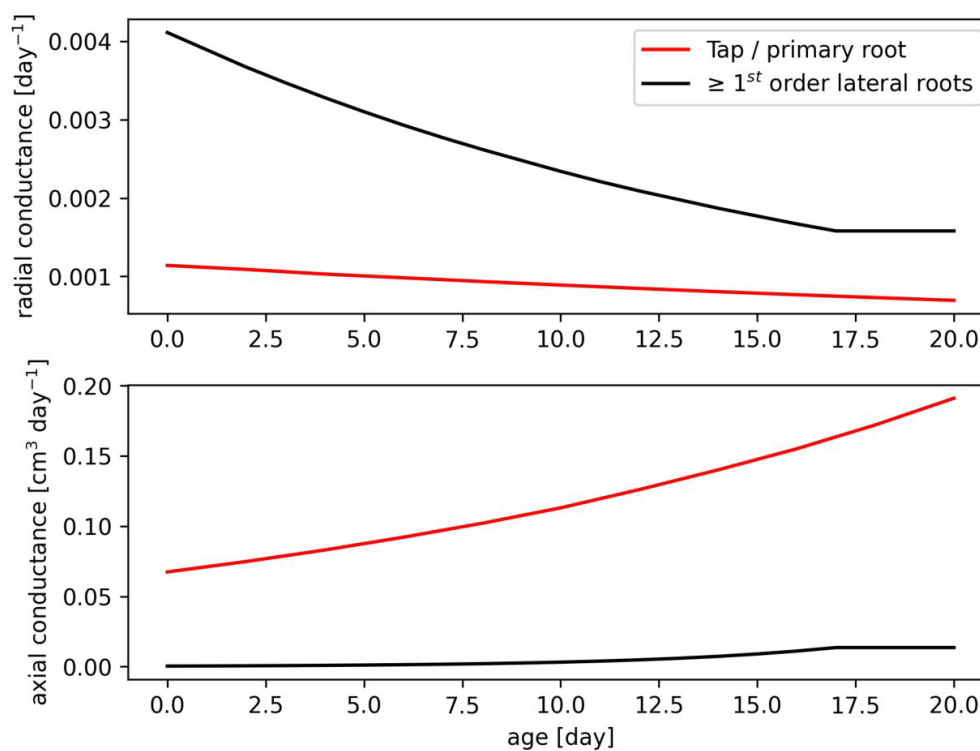


Fig. A.2: Age-dependent root hydraulic conductivities applied in the variable simulation scenario.

A4 Complete Root System Reconstructions

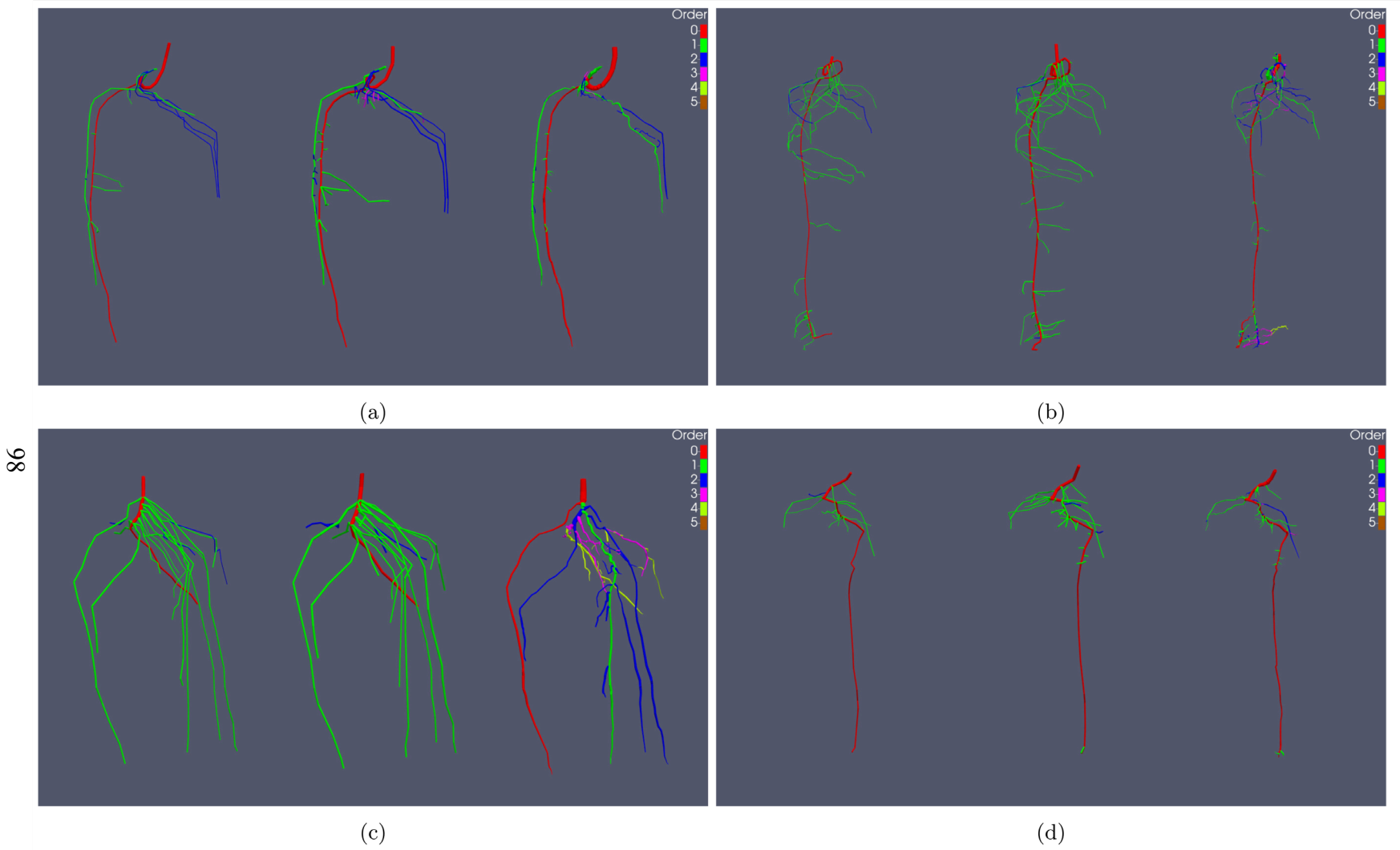


Fig. A.3: Manual tracings M (left), manual tracings after segmentation M+ (middle) and automated tracings A (right) of four *Lupinus albus* root systems (a-d) grown in sand derived by MRI scans. Colors display root orders, root segments are scaled by their respective radius. Age of the root systems is between 8 and 14 days (see Table 2.1).

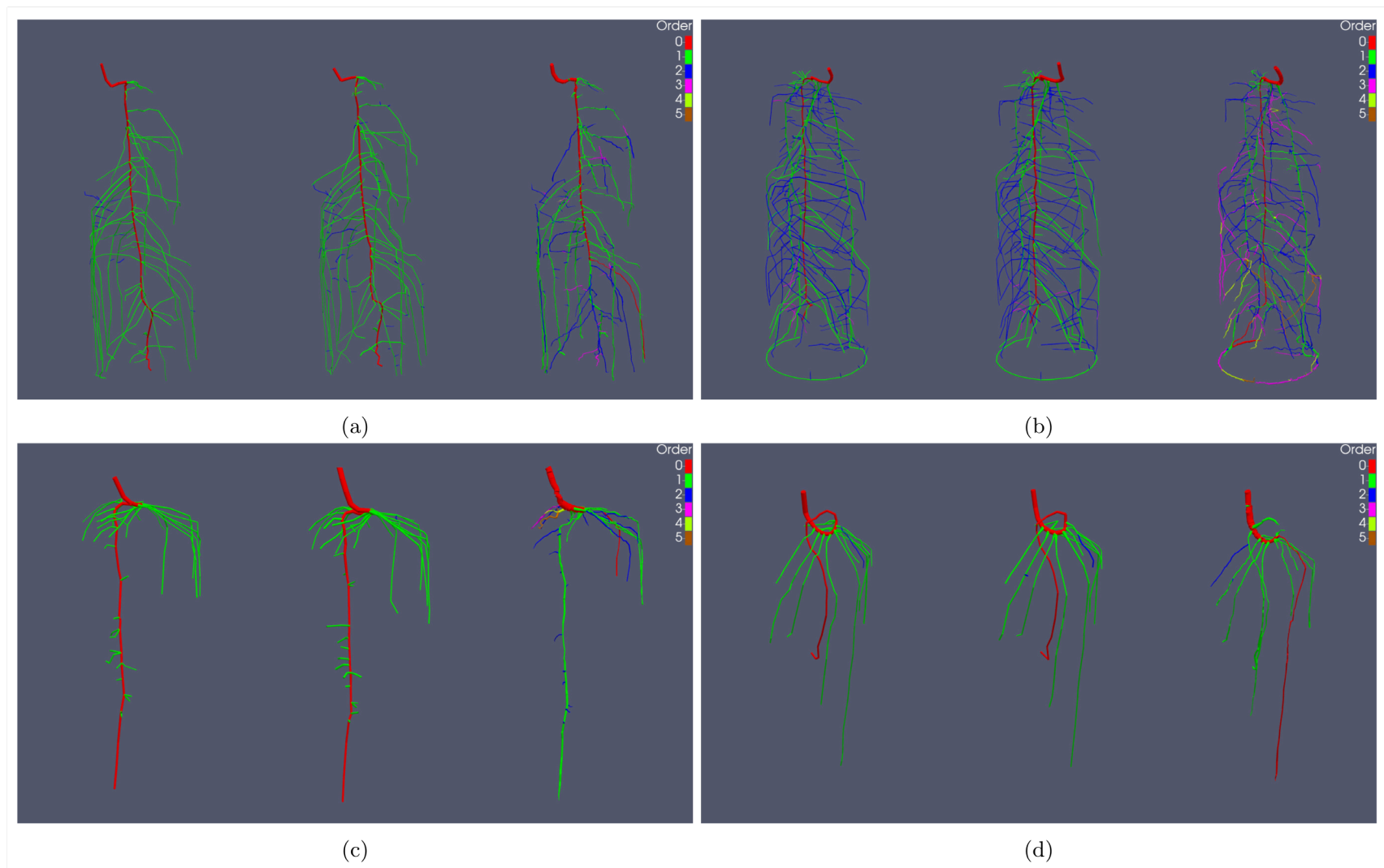


Fig. A.4: Manual tracings M (left), manual tracings after segmentation M+ (middle) and automated tracings A (right) of four *Lupinus albus* root systems (a-d) grown in soil derived by MRI scans. Colors display root orders, root segments are scaled by their respective radius. Age of the root systems is between 8 and 15 days (see Table 2.1).

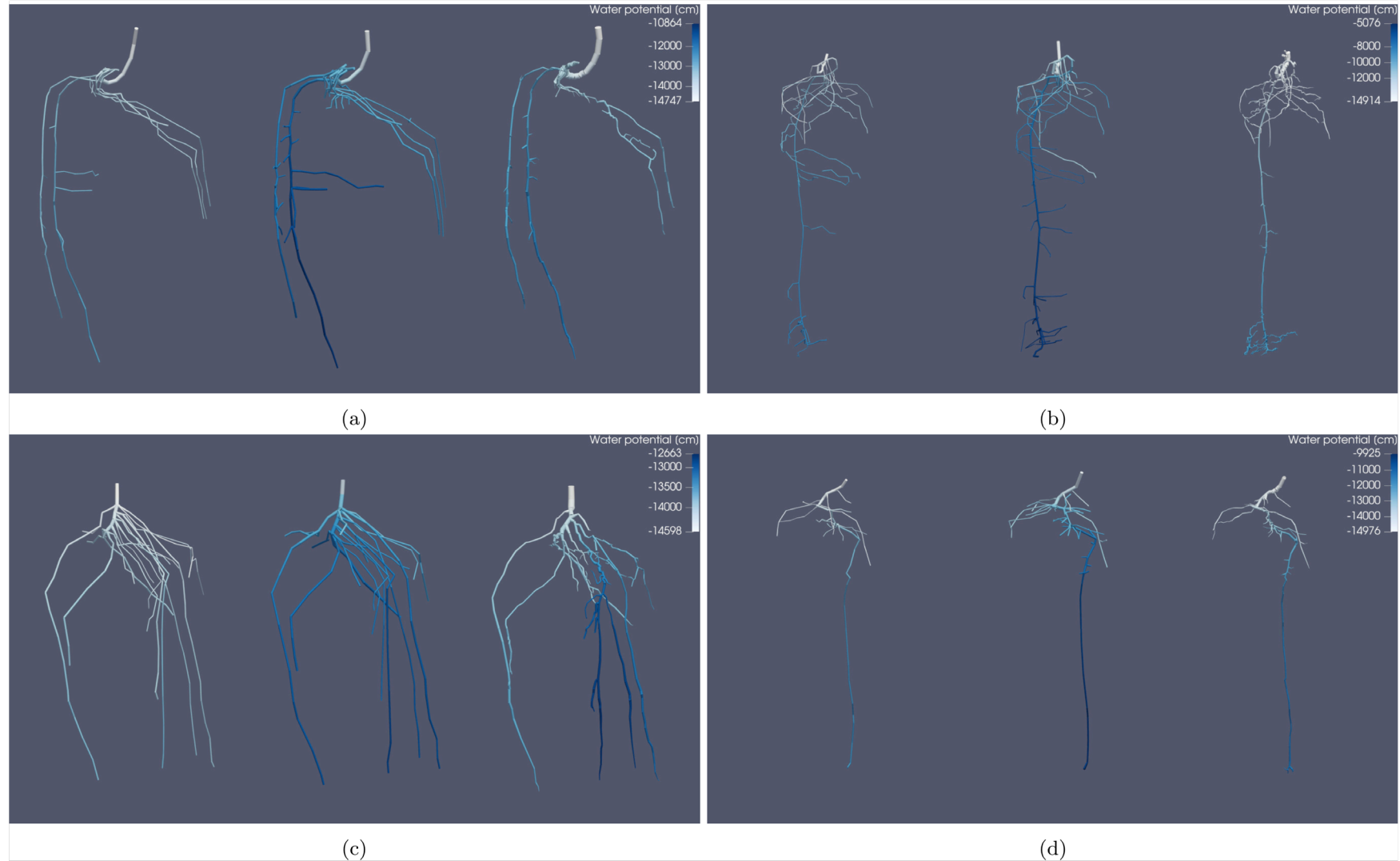


Fig. A.5: Manual tracings M (left), manual tracings after segmentation M+ (middle), and automated tracings A (right) of four *Lupinus albus* root systems (a-d) grown in sand derived by MRI scans. Age of the root systems is between 8 and 14 days (see Table 2.1). Shown is the root water potential (cm) of the constant simulation scenario, scaled to the maximal and minimal potentials observed for the three root systems shown in each subfigure. Root segments are scaled by their respective radius.

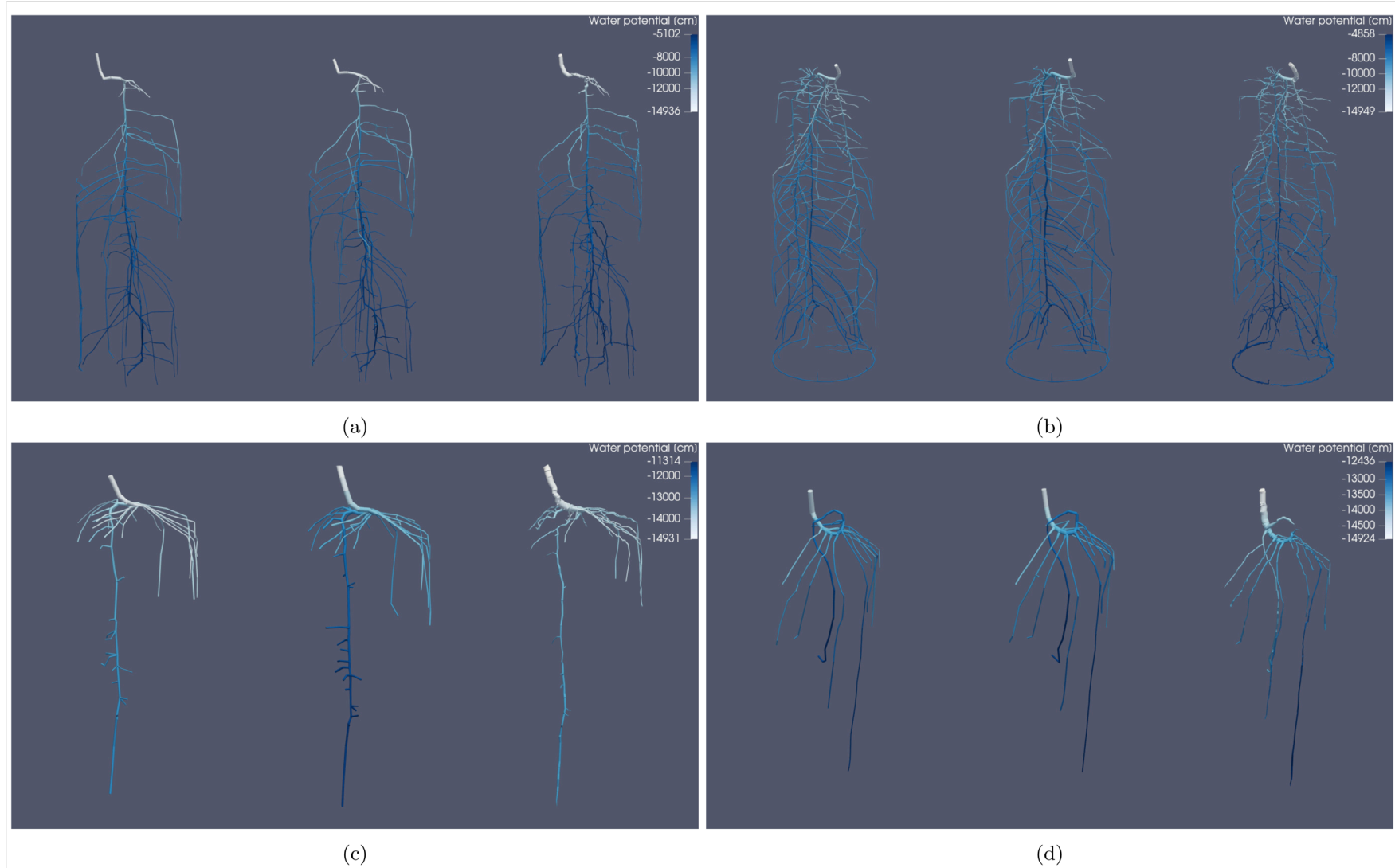


Fig. A.6: Manual tracings M (left), manual tracings after segmentation M+ (middle), and automated tracings A (right) of four *Lupinus albus* root systems (a-d) grown in soil derived by MRI scans. Age of the root systems is between 8 and 15 days (see Table 2.1). Shown is the root water potential (cm) of the constant simulation scenario, scaled to the maximal and minimal potentials observed for the three root systems shown in each subfigure. Root segments are scaled by their respective radius.

Table A.1: Comparison of root measures for *Lupinus albus* tracings derived by MRI scans. MRI_{sand} is comprised of the four root systems grown in sand. M denotes manual tracings derived using unaltered MRI images, M+ denotes manual tracings performed on the U-Net segmentations, A denotes tracings derived by the two-step automated workflow. Descriptions of the quantitative measures are given in Section 2.2.4.2, equations of measures and descriptions of the constant and variable simulation scenarios are given in Section A3. Note that K_{rs} and zSUF are simulated and not measured quantities (see Eq. A4 – Eq. A6).

Dataset	MRI _{sand}											
	1			2			3			4		
# of root system	137			233			105			97		
RL _{WR} (cm)	14			14			8			8		
Root system age (d)	M	M+	A	M	M+	A	M	M+	A	M	M+	A
Reconstruction method	M	M+	A	M	M+	A	M	M+	A	M	M+	A
CNR (-)	15.78	-	-	9.42	-	-	11.38	-	-	7.57	-	-
RL (cm)	64.57	84.09	56.29	148.28	185.73	138.63	98.23	97.46	84.68	55.93	74.13	58.82
Recovery rate (%)	47.13	61.38	41.09	63.64	79.81	59.50	93.55	92.82	80.65	57.66	76.42	60.42
RLD (cm cm ⁻³)	0.14	0.18	0.12	0.33	0.41	0.30	0.22	0.21	0.19	0.12	0.16	0.13
HMD (cm)	1.50	1.31	1.60	0.99	0.88	1.02	1.21	1.22	1.31	1.61	1.40	1.57
r_{mean} (mm)	0.248	0.329	0.359	0.232	0.298	0.280	0.251	0.336	0.318	0.305	0.391	0.337
# of roots (-)	17	38	33	37	55	111	18	19	36	15	32	31
# of 1 st laterals (-)	8	17	13	32	50	35	14	14	12	13	29	21
# of 2 nd laterals (-)	8	15	16	4	4	40	3	4	9	1	2	6
# of 3 rd laterals (-)	0	5	3	0	0	26	0	0	12	0	0	3
K_{rsc} (cm ² day ⁻¹)	1.52E-03	2.38E-03	1.87E-03	2.51E-03	3.20E-03	3.19E-03	2.49E-03	3.11E-03	2.60E-03	1.62E-03	2.50E-03	1.83E-03
K_{rsv} (cm ² day ⁻¹)	7.28E-03	1.07E-02	9.04E-03	1.20E-02	1.39E-02	1.71E-02	1.11E-02	1.21E-02	5.61E-03	9.50E-03	1.36E-02	1.01E-02
zSUF _c (cm)	-4.05	-4.16	-4.17	-5.74	-5.40	-5.80	-3.51	-3.39	-3.76	-4.88	-4.08	-4.74
zSUF _v (cm)	-3.48	-3.48	-3.31	-4.68	-3.78	-4.25	-1.95	-1.83	-2.71	-3.91	-3.13	-3.90
v_r (cm min ⁻¹)	2.21	4.86	-	2.52	5.96	-	4.51	8.03	-	3.91	7.12	-

Table A.2: Comparison of root measures for *Lupinus albus* tracings derived by MRI scans. MRI_{soil} is comprised of the four root systems grown in Kaldenkirchen soil. M denotes manual tracings derived using unaltered MRI images, M+ denotes manual tracings performed on the U-Net segmentations, A denotes tracings derived by the two-step automated workflow. Descriptions of the quantitative measures are given in Section 2.2.4.2, equations of measures and descriptions of the constant and variable simulation scenarios are given in Section A3. Note that K_{rs} and zSUF are simulated and not measured quantities (see Eq. A4 – Eq. A6).

Dataset	MRI _{soil}											
	5			6			7			8		
# of root system	5			6			7			8		
RL _{WR} (cm)	323			508			85			84		
Root system age (d)	14			15			9			8		
Reconstruction method	M	M+	A	M	M+	A	M	M+	A	M	M+	A
CNR (-)	133.26	-	-	132.58	-	-	160.80	-	-	257.54	-	-
RL (cm)	269.24	293.15	276.57	488.34	480.69	473.02	68.56	76.02	64.37	76.77	75.61	68.02
Recovery rate (%)	83.36	90.76	85.63	96.13	94.42	93.11	80.66	89.44	75.73	91.39	90.01	80.89
RLD (cm cm ⁻³)	0.59	0.64	0.61	1.07	1.06	1.04	0.15	0.17	0.14	0.17	0.17	0.15
HMD (cm)	0.73	0.70	0.72	0.54	0.55	0.55	1.45	1.38	1.50	1.37	1.38	1.46
r_{mean} (mm)	0.231	0.228	0.243	0.223	0.230	0.220	0.288	0.332	0.284	0.305	0.337	0.312
# of roots (-)	75	109	124	192	199	267	35	39	34	15	15	17
# of 1 st laterals (-)	60	59	37	45	44	39	34	37	11	13	12	13
# of 2 nd laterals (-)	14	49	64	137	146	127	0	1	18	1	2	3
# of 3 rd laterals (-)	0	0	20	9	8	73	0	0	1	0	0	0
K_{rsc} (cm ² day ⁻¹)	3.18E-03	3.42E-03	3.30E-03	6.03E-03	5.70E-03	5.50E-03	1.90E-03	2.28E-03	1.77E-03	2.23E-03	2.42E-03	2.05E-03
K_{rsv} (cm ² day ⁻¹)	1.31E-02	1.42E-02	1.25E-02	1.63E-02	1.61E-02	1.44E-02	1.33E-02	1.39E-02	8.65E-03	1.09E-02	1.15E-02	1.04E-02
zSUF _c (cm)	-9.28	-9.04	-9.36	-9.73	-9.53	-9.75	-3.35	-3.26	-3.08	-3.47	-3.46	-3.62
zSUF _v (cm)	-6.64	-6.30	-6.04	-5.38	-5.02	-5.81	-2.96	-2.92	-1.75	-2.17	-2.16	-2.59
v_r (cm min ⁻¹)	7.67	9.37	-	6.19	8.61	-	4.29	5.05	-	5.02	6.51	-

Appendix B

Table B.1: Soil hydraulic parameters. θ_r is the residual water content, θ_s is the saturated water content, α , and n are the van Genuchten parameters, K_s is the saturated soil hydraulic conductivity and λ is the van Genuchten-Mualem parameter.

Soil type	θ_r ($\text{cm}^3 \text{cm}^{-3}$)	θ_s ($\text{cm}^3 \text{cm}^{-3}$)	α (cm^{-1})	n (-)	K_s (cm d^{-1})	λ
Sand	0.045	0.43	0.15	3.0	1000	0.5
Loam	0.08	0.43	0.04	1.6	50	0.5
Clay	0.01	0.40	0.01	1.1	10	0.5

Table B.2: Different soil resolutions and their corresponding soil voxel sizes. VS_x , VS_y , and VS_z refer to the soil voxel sizes in x-, y-, and z- direction respectively. VS gives an approximated soil voxel size as used in the manuscript for simplicity.

Soil resolution	Degree of freedom	VS_x (cm)	VS_y (cm)	VS_z (cm)	VS (cm)
$40 \times 40 \times 75$	120000	0.20	0.20	0.20	0.2
$26 \times 25 \times 50$	33800	0.31	0.31	0.30	0.3
$20 \times 20 \times 38$	15200	0.40	0.40	0.39	0.4
$13 \times 13 \times 25$	4225	0.62	0.62	0.60	0.6
$10 \times 10 \times 19$	1900	0.80	0.80	0.78	0.8
$8 \times 8 \times 15$	960	1.00	1.00	1.00	0.8
$5 \times 5 \times 10$	250	1.60	1.60	1.50	1.5
$4 \times 4 \times 8$	128	2.00	2.00	1.88	2.0
$3 \times 3 \times 5$	45	2.67	2.67	3.00	3.0
$2 \times 2 \times 4$	16	4.00	4.00	3.75	4.0

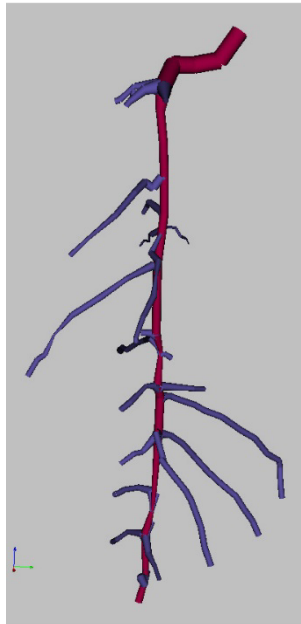


Fig. B.1: Root system architecture of a static 8-day old lupine plant. Red refers to the taproot, purple shows 1st order laterals.

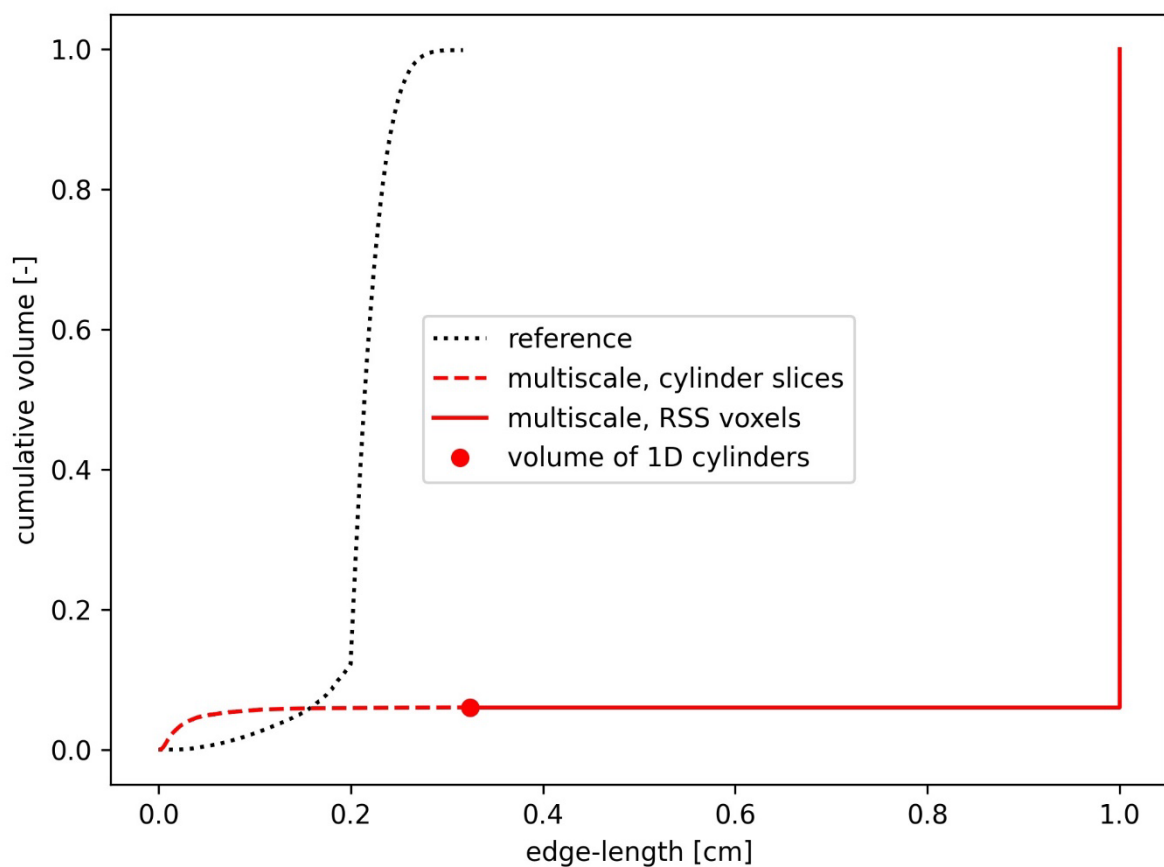


Fig. B.2: Edge-lengths of the grid elements used in the reference solution (black) and the multi-scale model (red) against cumulative volume covered by a certain edge-length.

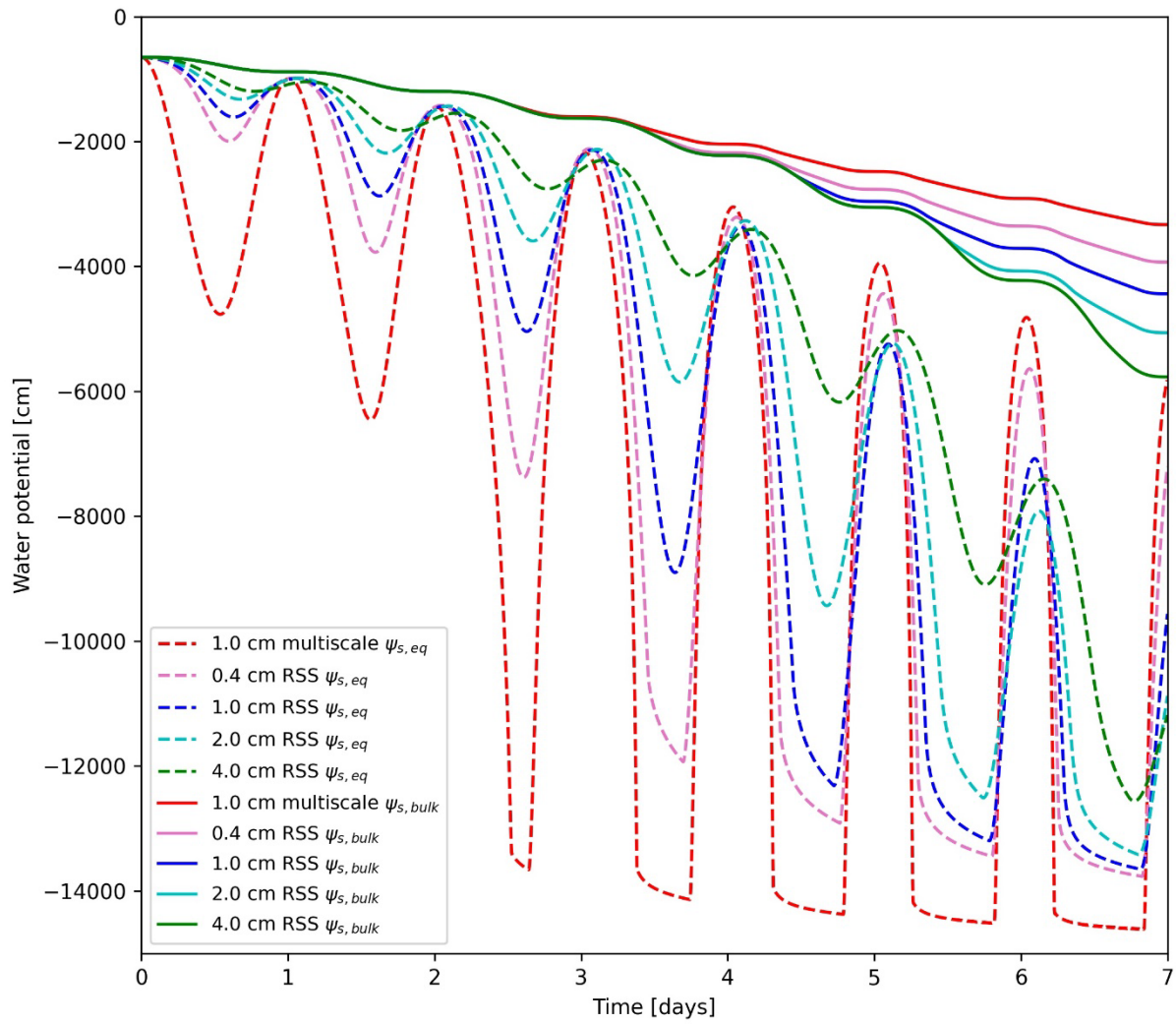


Fig. B.3: Equivalent soil water potential, $\psi_{s,eq}$, (dashed) and mean bulk soil water potential, $\psi_{s,bulk}$, (solid) for multi-scale and root system scale (RSS) model at different soil resolutions in the clay scenario at initial $\psi_{s,top} = -659.8$ cm.

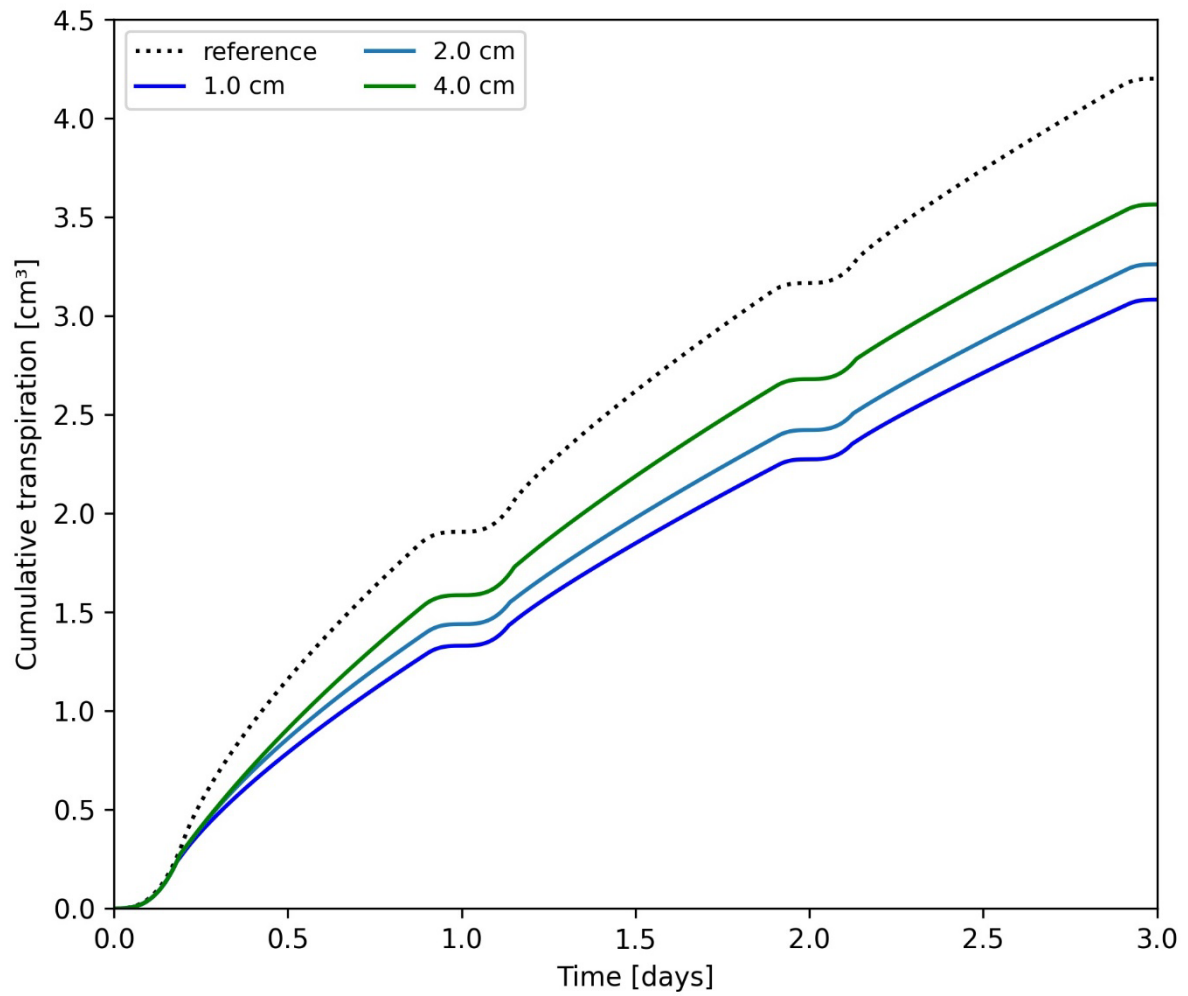


Fig. B.4: Cumulative transpiration of the reference solution (dotted) and the multi-scale model at different soil resolutions (solid) for the loamy soil scenario of benchmark C1.2 at initial $\psi_{s,top} = -659.8$ cm.

Appendix C

C1 PyGmsh Code for Discretizing a Cylindrical Container

```
import pygmsh
import meshio

geom = pygmsh.opencascade.Geometry(
    characteristic_length_min=0.003,
    characteristic_length_max=0.003,
)

# Points for a rectangle
point1 = geom.add_point([-0.012,-0.012,-0.185])
point2 = geom.add_point([0.012,-0.012,-0.185])
point3 = geom.add_point([-0.012,0.012,-0.185])
point4 = geom.add_point([0.012,0.012,-0.185])

# Connect points of rectangle
line1 = geom.add_line(point1,point2)
line2 = geom.add_line(point2,point4)
line3 = geom.add_line(point4,point3)
line4 = geom.add_line(point3,point1)

# Discretize rectangle
lines = [];
lines.append(line1); lines.append(line2); lines.append(line3); lines.append(line4);
geom.set_transfinite_lines(lines,10)
line_loop1 = geom.add_line_loop(lines)

rect = geom.add_plane_surface(line_loop1,holes=None)
geom.set_transfinite_surface(rect)
geom.add_raw_code("Mesh.RecombineAll = 1;")

# Add disc of radius r around rectangle
disk = geom.add_disk([0.0, 0.0, -0.185], 0.0281)
rect2 = geom.add_plane_surface(line_loop1,holes=None)
diskwithhole = geom.boolean_difference([disk],[rect2])

# Merge rectangle and disc
union = geom.boolean_union([diskwithhole,rect])

# Extrude 20 layers of the unified geometrie in z-direction
geom.extrude(union, translation_axis=[0.0, 0.0, 0.185], num_layers=20, recombine=True,)

mesh = pygmsh.generate_mesh(geom)
meshio.write("cylinder.vtk", mesh)
meshio.write("cylinder.msh",mesh,"gmsh2-ascii")
```

Acknowledgements

My special thanks go to my supervisors, Prof. Dr. Andrea Schnepf and Prof. Dr. Jan Vanderborght, for their continuous support and guidance throughout my Ph.D. project. You offered your invaluable knowledge, dedication, and advice to guide me during these last years. I am extremely grateful for your thoughtful and enlightening feedback, and the inspiring discussions that we had. Your patience and the motivation you offered is much appreciated.

I want to extend my gratitude to Prof. Dr. Harry Vereecken and Prof. Dr. Guillaume Lobet, who also offered me excellent advice and feedback during the last years. In addition, I want to thank Dr. Daniel Leitner for his constant support and help with the ROSI models and Dr. Magdalena Landl for her enormous help at the beginning of my project.

Furthermore, I want to thank the IBG-3 board of directors, Prof. Dr. Harry Vereecken, Prof. Dr. Jan Vanderborght and Prof. Dr. Wulf Amelung for creating such a great working environment for Ph.D. students.

I also want to thank all present and former members of the ROSI group that I have got to know over the last years. It was a delight to work with all of you. Special greetings go out to Helena, Magdalena, Deepanshu, Dirk, Daniel, Juan, Mona, Felix, Ullah, and Xiaoran.

I want to thank my friends in Jülich, who have made my stay and life here so enjoyable: Shirin, Jessi, Richard, Jini, Eddy, Magda, Micha, Helena, Pascha, Deepanshu, Dalir, and all the others I may have missed.

Finally, I want to give a special thanks to my parents. Without you, this endeavour would not have been possible. I am very grateful for your support.

Bibliography

- Alalwan, N., Abozeid, A., ElHabshy, A. A., & Alzahrani, A. (2021). Efficient 3D Deep Learning Model for Medical Image Semantic Segmentation. *Alexandria Engineering Journal*, *60*(1), 1231–1239. <https://doi.org/10.1016/j.aej.2020.10.046>
- Al-Kofahi, Y., Zaltsman, A., Graves, R., Marshall, W., & Rusu, M. (2018). A deep learning-based algorithm for 2-D cell segmentation in microscopy images. *BMC Bioinformatics*, *19*, Article 365. <https://doi.org/10.1186/s12859-018-2375-z>
- Alle, J., Gruber, R., Wörlein, N., Uhlmann, N., Claußen, J., Wittenberg, T., & Gerth, S. (2023). 3D segmentation of plant root systems using spatial pyramid pooling and locally adaptive field-of-view inference. *Frontiers in Plant Science*, *14*, Article 1120189. <https://doi.org/10.3389/fpls.2023.1120189>
- Alvarez-Borges, F. J., King, O. N. F., Madhusudhan, B. N., Connolley, T., Basham, M., & Ahmed, S. I. (2023). Comparison of Methods to Segment Variable-Contrast XCT Images of Methane-Bearing Sand Using U-Nets Trained on Single Dataset Sub-Volumes. *Methane*, *2*(1), 1–23. <https://doi.org/10.3390/methane2010001>
- Amelung, W., Blume, H.-P., Fleige, H., Horn, R., Kandeler, E., Kögel-Knabner, I., Kretzschmar, R., Stahr, K., & Wilke, B.-M. (2018). *Scheffer/Schachtschabel. Lehrbuch der Bodenkunde* (17th ed.). Springer Spektrum Berlin. <https://doi.org/10.1007/978-3-662-55871-3>
- Arkley, R. (1963). Relationships between plant growth and transpiration. *Hilgardia*, *34*(13), 559–584. <https://doi.org/10.3733/hilg.v34n13p559>
- Assouline, S. (2006a). Modeling the Relationship between Soil Bulk Density and the Hydraulic Conductivity Function. *Vadose Zone Journal*, *5*(2), 697–705. <https://doi.org/10.2136/vzj2005.0084>

- Assouline, S. (2006b). Modeling the Relationship between Soil Bulk Density and the Water Retention Curve. *Vadose Zone Journal*, 5(2), 554–563. <https://doi.org/10.2136/vzj2005.0083>
- Atkinson, J. A., Pound, M. P., Bennett, M. J., & Wells, D. M. (2019). Uncovering the hidden half of plants using new advances in root phenotyping. *Current Opinion in Biotechnology*, 55, 1–8. <https://doi.org/10.1016/j.copbio.2018.06.002>
- Atkinson, J. A., Wingen, L. U., Griffiths, M., Pound, M. P., Gaju, O., Foulkes, M. J., Le Gouis, J., Griffiths, S., Bennett, M. J., King, J., & Wells, D. M. (2015). Phenotyping pipeline reveals major seedling root growth QTL in hexaploid wheat. *Journal of Experimental Botany*, 66(8), 2283–2292. <https://doi.org/10.1093/jxb/erv006>
- Baghyalakshmi, K., Jeyaprakash, P., Ramchander, S., & Robin, M. R. and S. (2020). Two dimensional in-vitro phenotyping of root system architecture using Poly Ethylene Glycol in backcross inbred lines harboring drought tolerant QTLs of rice (*Oryza sativa* L.). *Electronic Journal of Plant Breeding*, 11(2), Article 02. <https://doi.org/10.37992/2020.1102.061>
- Bauer, F., Lärm, L., Morandage, S., Lobet, G., Vanderborght, J., Vereecken, H., & Schnepf, A. (2022). Development and Validation of a Deep Learning Based Automated Minirhizotron Image Analysis Pipeline. *Plant Phenomics*, 2022, Article 9758532. <https://doi.org/10.34133/2022/9758532>
- Baumhardt, R. L., Stewart, B. A., & Sainju, U. M. (2015). North American Soil Degradation: Processes, Practices, and Mitigating Strategies. *Sustainability*, 7(3), 2936–2960. <https://doi.org/10.3390/su7032936>
- Behnke, S. (2001). Learning Iterative Image Reconstruction in the Neural Abstraction Pyramid. *International Journal of Computational Intelligence and Applications*, 1(4), 427–438. <https://doi.org/10.1142/S1469026801000342>

- Benton, T. G., Bieg, C., Harwatt, H., Pudasaini, R., & Wellesley, L. (2021). *Food system impacts on biodiversity loss. Three levers for food system transformation in support of nature*. <https://doi.org/10.13140/RG.2.2.34045.28640>
- Bereswill, S., Gatz-Miller, H., Su, D., Tötze, C., Kardjilov, N., Oswald, S. E., & Mayer, K. U. (2023). Coupling non-invasive imaging and reactive transport modeling to investigate water and oxygen dynamics in the root zone. *Vadose Zone Journal*, 22(5), Article e20268. <https://doi.org/10.1002/vzj2.20268>
- Beudez, N., Doussan, C., Lefeuvre-Mesgouez, G., & Mesgouez, A. (2013). Influence of Three Root Spatial Arrangement on Soil Water Flow and Uptake. Results from an Explicit and an Equivalent, Upscaled, Model. *Procedia Environmental Sciences*, 19, 37–46. <https://doi.org/10.1016/j.proenv.2013.06.005>
- Biffi, S., Traldi, R., Crezee, B., Beckmann, M., Egli, L., Schmidt, D. E., Motzer, N., Okumah, M., Seppelt, R., Slabbert, E. L., Tiedeman, K., Wang, H., & Ziv, G. (2021). Aligning agri-environmental subsidies and environmental needs: A comparative analysis between the US and EU. *Environmental Research Letters*, 16(5), Article 054067. <https://doi.org/10.1088/1748-9326/abfa4e>
- Borlaug, N. (2007). Feeding a Hungry World. *Science*, 318(5849), 359–359. <https://doi.org/10.1126/science.1151062>
- Boyer, J. S. (1982). Plant Productivity and Environment. *Science*, 218(4571), 443–448. <https://doi.org/10.1126/science.218.4571.443>
- Brady, N. C., & Weil, R. R. (2016). *The nature and properties of soils* (15th ed.). Pearson Education.
- Buczko, U., Kuchenbuch, R. O., & Gerke, H. H. (2008). Evaluation of a core sampling scheme to characterize root length density of maize. *Plant and Soil*, 316, 205–215. <https://doi.org/10.1007/s11104-008-9771-5>

- Burney, J. A., Davis, S. J., & Lobell, D. B. (2010). Greenhouse gas mitigation by agricultural intensification. *Proceedings of the National Academy of Sciences*, *107*(26), 12052–12057. <https://doi.org/10.1073/pnas.0914216107>
- Cai, G., Vanderborght, J., Klotzsche, A., van der Kruk, J., Neumann, J., Hermes, N., & Vereecken, H. (2016). Construction of Minirhizotron Facilities for Investigating Root Zone Processes. *Vadose Zone Journal*, *15*(9), Article vzj2016.05.0043. <https://doi.org/10.2136/vzj2016.05.0043>
- Campbell, B., Beare, D., Bennett, E., Hall-Spencer, J., Ingram, J., Jaramillo, F., Ortiz, R., Ramankutty, N., Sayer, J., & Shindell, D. (2017). Agriculture production as a major driver of the Earth system exceeding planetary boundaries. *Ecology and Society*, *22*(4). <https://doi.org/10.5751/ES-09595-220408>
- Campbell, B. D., Grime, J. P., & Mackey, J. M. L. (1991). A trade-off between scale and precision in resource foraging. *Oecologia*, *87*(4), 532–538. <https://doi.org/10.1007/BF00320417>
- Carminati, A., Ahmed, M., Zarebanadkouki, M., Cai, G., Lovric, G., & Javaux, M. (2020). Stomatal closure prevents the drop in soil water potential around roots. *New Phytologist*, *226*(6), 1541–1543. <https://doi.org/10.1111/nph.16451>
- Carminati, A., Zarebanadkouki, M., Kroener, E., Ahmed, M., & Holz, M. (2016). Biophysical rhizosphere processes affecting root water uptake. *Annals of Botany*, *118*(4), 561–571. <https://doi.org/10.1093/aob/mcw113>
- Cassel, D. K., & Nielsen, D. R. (1986). Field Capacity and Available Water Capacity. In A. Klute (Ed.), *Methods of Soil Analysis* (pp. 901–926). John Wiley & Sons, Ltd. <https://doi.org/10.2136/sssabookser5.1.2ed.c36>
- Çiçek, Ö., Abdulkadir, A., Lienkamp, S. S., Brox, T., & Ronneberger, O. (2016). 3D U-Net: Learning Dense Volumetric Segmentation from Sparse Annotation. In S. Ourselin, L. Joskowicz, M. R. Sabuncu, G. Unal, & W. Wells (Eds.), *Medical Image Computing and*

- Computer-Assisted Intervention – MICCAI 2016* (pp. 424–432). Springer International Publishing. https://doi.org/10.1007/978-3-319-46723-8_49
- Cordell, D., Drangert, J.-O., & White, S. (2009). The story of phosphorus: Global food security and food for thought. *Global Environmental Change*, *19*(2), 292–305. <https://doi.org/10.1016/j.gloenvcha.2008.10.009>
- Cordell, D., & White, S. (2011). Peak Phosphorus: Clarifying the Key Issues of a Vigorous Debate about Long-Term Phosphorus Security. *Sustainability*, *3*(10), 2027–2049. <https://doi.org/10.3390/su3102027>
- Correa, J., Postma, J. A., Watt, M., & Wojciechowski, T. (2019). Soil compaction and the architectural plasticity of root systems. *Journal of Experimental Botany*, *70*(21), 6019–6034. <https://doi.org/10.1093/jxb/erz383>
- Couvreur, V., Vanderborght, J., & Javaux, M. (2012). A simple three-dimensional macroscopic root water uptake model based on the hydraulic architecture approach. *Hydrology and Earth System Sciences*, *16*(8), 2957–2971. <https://doi.org/10.5194/hess-16-2957-2012>
- Cowan, I. R. (1965). Transport of Water in the Soil-Plant-Atmosphere System. *Journal of Applied Ecology*, *2*(1), 221–239. <https://doi.org/10.2307/2401706>
- Daly, K. R., Tracy, S. R., Crout, N. M. J., Mairhofer, S., Pridmore, T. P., Mooney, S. J., & Roose, T. (2018). Quantification of root water uptake in soil using X-ray computed tomography and image-based modelling. *Plant, Cell & Environment*, *41*(1), 121–133. <https://doi.org/10.1111/pce.12983>
- Dawson, T. E. (1993). Hydraulic lift and water use by plants: Implications for water balance, performance and plant-plant interactions. *Oecologia*, *95*(4), 565–574. <https://doi.org/10.1007/BF00317442>
- de Ridder, M., de Jong, S., Polchar, J., & Lingemann, S. (2012). Risks and opportunities in the global phosphate rock market: Robust strategies in times of uncertainty. *The Hague Centre for Strategic Studies*. <https://hcss.nl/wp->

content/uploads/2012/12/Risks_and_Opportunities_in_the_Global_Phosphate_Rock_Market.pdf

- de Willigen, P., Heinen, M., & van Noordwijk, M. (2018). Roots Partially in Contact with Soil: Analytical Solutions and Approximation in Models of Nutrient and Water Uptake. *Vadose Zone Journal*, 17(1), Article 170060. <https://doi.org/10.2136/vzj2017.03.0060>
- Dijkstra, E. W. (1959). A Note on Two Problems in Connexion with Graphs. *Numerische Mathematik*, 1, 269–271. <https://doi.org/10.1007/BF01386390>
- Dong, C., Loy, C. C., He, K., & Tang, X. (2014). Learning a Deep Convolutional Network for Image Super-Resolution. In D. Fleet, T. Pajdla, B. Schiele, & T. Tuytelaars (Eds.), *Computer Vision – ECCV 2014* (pp. 184–199). Springer International Publishing. https://doi.org/10.1007/978-3-319-10593-2_13
- Douglas, D. H., & Peucker, T. K. (1973). Algorithms for the reduction of the number of points required to represent a digitized line or its caricature. *Cartographica: The International Journal for Geographic Information and Geovisualization*, 10(2), 112–122. <https://doi.org/10.3138/FM57-6770-U75U-7727>
- Doussan, C., Pagès, L., & Vercambre, G. (1998a). Modelling of the Hydraulic Architecture of Root Systems: An Integrated Approach to Water Absorption—Distribution of Axial and Radial Conductances in Maize. *Annals of Botany*, 81(2), 225–232. <https://doi.org/10.1006/anbo.1997.0541>
- Doussan, C., Pagès, L., & Vercambre, G. (1998b). Modelling of the Hydraulic Architecture of Root Systems: An Integrated Approach to Water Absorption—Model Description. *Annals of Botany*, 81(2), 213–223. <https://doi.org/10.1006/anbo.1997.0540>
- Doussan, C., Pierret, A., Garrigues, E., & Pagès, L. (2006). Water Uptake by Plant Roots: II – Modelling of Water Transfer in the Soil Root-system with Explicit Account of Flow within the Root System – Comparison with Experiments. *Plant and Soil*, 283, 99–117. <https://doi.org/10.1007/s11104-004-7904-z>

- Draye, X., Kim, Y., Lobet, G., & Javaux, M. (2010). Model-assisted integration of physiological and environmental constraints affecting the dynamic and spatial patterns of root water uptake from soils. *Journal of Experimental Botany*, *61*(8), 2145–2155. <https://doi.org/10.1093/jxb/erq077>
- Dunbabin, V. M., McDermott, S., & Bengough, A. G. (2006). Upscaling from Rhizosphere to Whole Root System: Modelling the Effects of Phospholipid Surfactants on Water and Nutrient Uptake. *Plant and Soil*, *283*, 57–72. <https://doi.org/10.1007/s11104-005-0866-y>
- Dunbabin, V. M., Postma, J. A., Schnepf, A., Pagès, L., Javaux, M., Wu, L., Leitner, D., Chen, Y. L., Rengel, Z., & Diggle, A. J. (2013). Modelling root–soil interactions using three–dimensional models of root growth, architecture and function. *Plant and Soil*, *372*, 93–124. <https://doi.org/10.1007/s11104-013-1769-y>
- Elser, J., & Bennett, E. (2011). A broken biogeochemical cycle. *Nature*, *478*(7367), 29–31. <https://doi.org/10.1038/478029a>
- Evenson, R. E., & Gollin, D. (2003). Assessing the Impact of the Green Revolution, 1960 to 2000. *Science*, *300*(5620), 758–762. <https://doi.org/10.1126/science.1078710>
- FAO. (2013). Climate-smart agriculture sourcebook. *Food and Agriculture Organization of the United Nations (FAO)*, Rome, Italy. <https://www.fao.org/3/i3325e/i3325e.pdf>
- FAO. (2017). The future of food and agriculture – Trends and challenges. *Food and Agriculture Organization of the United Nations (FAO)*, Rome, Italy. <https://www.fao.org/3/i6583e/i6583e.pdf>
- FAO. (2020). Land use statistics and indicators: Global, regional and country trends, 2000–2020, FAOSTAT Analytical Brief, no. 48. *Food and Agriculture Organization of the United Nations (FAO)*, Rome, Italy. <https://doi.org/10.4060/cc0963en>

- FAO. (2021). The impact of disasters and crises on agriculture and food security: 2021. *Food and Agriculture Organization of the United Nations (FAO)*, Rome, Italy. <https://doi.org/10.4060/cb3673en>
- FAO. (2022). Emissions due to agriculture. Global, regional and country trends, 2000–2018, FAOSTAT Analytical Brief, no. 18. *Food and Agriculture Organization of the United Nations (FAO)*, Rome, Italy. <https://www.fao.org/3/cb3808en/cb3808en.pdf>
- FAO, & ITPS. (2015). Status of the World's Soil Resources (SWSR)—Technical Summary. *Food and Agriculture Organization of the United Nations (FAO) and Intergovernmental Technical Panel on Soils (ITPS)*, Rome, Italy. <https://www.fao.org/3/i5126e/i5126e.pdf>
- Farooq, M., Wahid, A., Kobayashi, N., Fujita, D., & Basra, S. M. A. (2009). Plant drought stress: Effects, mechanisms and management. *Agronomy for Sustainable Development*, 29(1), 185–212. <https://doi.org/10.1051/agro:2008021>
- Fitter, A. H. (1987). An Architectural Approach to the Comparative Ecology of Plant Root Systems. *New Phytologist*, 106, 61–77. <https://doi.org/10.1111/j.1469-8137.1987.tb04683.x>
- Foley, J. A., DeFries, R., Asner, G. P., Barford, C., Bonan, G., Carpenter, S. R., Chapin, F. S., Coe, M. T., Daily, G. C., Gibbs, H. K., Helkowski, J. H., Holloway, T., Howard, E. A., Kucharik, C. J., Monfreda, C., Patz, J. A., Prentice, I. C., Ramankutty, N., & Snyder, P. K. (2005). Global Consequences of Land Use. *Science*, 309(5734), 570–574. <https://doi.org/10.1126/science.1111772>
- Fromm, H. (2019). Root Plasticity in the Pursuit of Water. *Plants*, 8(7), Article 236. <https://doi.org/10.3390/plants8070236>
- Fry, E. L., Evans, A. L., Sturrock, C. J., Bullock, J. M., & Bardgett, R. D. (2018). Root architecture governs plasticity in response to drought. *Plant and Soil*, 433, 189–200. <https://doi.org/10.1007/s11104-018-3824-1>

- Gao, W., Blaser, S. R. G. A., Schlüter, S., Shen, J., & Vetterlein, D. (2019). Effect of localised phosphorus application on root growth and soil nutrient dynamics in situ – Comparison of maize (*Zea mays*) and faba bean (*Vicia faba*) at the seedling stage. *Plant and Soil*, *441*, 469–483. <https://doi.org/10.1007/s11104-019-04138-2>
- Gates, D. M. (1968). Transpiration and Leaf Temperature. *Annual Review of Plant Physiology*, *19*, 211–238. <https://doi.org/10.1146/annurev.pp.19.060168.001235>
- Gerth, S., Claußen, J., Eggert, A., Woerlein, N., Waininger, M., Wittenberg, T., & Uhlmann, N. (2021). Semiautomated 3D Root Segmentation and Evaluation Based on X-Ray CT Imagery. *Plant Phenomics*, *2021*, 1–13. <https://doi.org/10.34133/2021/8747930>
- Geuzaine, C., & Remacle, J.-F. (2009). Gmsh: A 3-D finite element mesh generator with built-in pre- and post-processing facilities. *International Journal for Numerical Methods in Engineering*, *79*(11), 1309–1331. <https://doi.org/10.1002/nme.2579>
- Giehl, R. F. H., & von Wirén, N. (2018). Hydropatterning—How roots test the waters. *Science*, *362*(6421), 1358–1359. <https://doi.org/10.1126/science.aav9375>
- Giraud, M., Gall, S. L., Harings, M., Javaux, M., Leitner, D., Meunier, F., Rothfuss, Y., van Dusschoten, D., Vanderborght, J., Vereecken, H., Lobet, G., & Schnepf, A. (2023). CPlantBox: A fully coupled modelling platform for the water and carbon fluxes in the soil–plant–atmosphere continuum. *In Silico Plants*, *5*(2), Article diad009. <https://doi.org/10.1093/insilicoplants/diad009>
- Graefe, J., Prüfert, U., & Bitterlich, M. (2019). Extension of the Cylindrical Root Model for Water Uptake to Non-Regular Root Distributions. *Vadose Zone Journal*, *18*(1), Article 180127. <https://doi.org/10.2136/vzj2018.06.0127>
- Grime, J. P., & Mackey, J. M. L. (2002). The role of plasticity in resource capture by plants. *Evolutionary Ecology*, *16*(3), 299–307. <https://doi.org/10.1023/A:1019640813676>
- Grizzetti, B., Bouraoui, F., Billen, G., van Grinsven, H., Cardoso, A. C., Thieu, V., Garnier, J., Curtis, C., Howarth, R., & Johnes, P. (2011). Nitrogen as a threat to European water

- quality. In M. A. Sutton, C. M. Howard, J. W. Erisman, G. Billen, A. Bleeker, P. Grennfelt, H. van Grinsven, & B. Grizzetti (Eds.), *The European Nitrogen Assessment: Sources, Effects and Policy Perspective* (1st ed., pp. 379–404). Cambridge University Press. <https://doi.org/10.1017/CBO9780511976988.020>
- Gruber, B. D., Giehl, R. F. H., Friedel, S., & von Wirén, N. (2013). Plasticity of the Arabidopsis Root System under Nutrient Deficiencies. *Plant Physiology*, *163*(1), 161–179. <https://doi.org/10.1104/pp.113.218453>
- Haber-Pohlmeier, S., Bechtold, M., Stapf, S., & Pohlmeier, A. (2010). Water Flow Monitored by Tracer Transport in Natural Porous Media Using Magnetic Resonance Imaging. *Vadose Zone Journal*, *9*(4), 835–845. <https://doi.org/10.2136/vzj2009.0177>
- Hansen, B., Thorling, L., Schullehner, J., Termansen, M., & Dalgaard, T. (2017). Groundwater nitrate response to sustainable nitrogen management. *Scientific Reports*, *7*(1), Article 8566. <https://doi.org/10.1038/s41598-017-07147-2>
- He, Y., Yu, H., Liu, X., Yang, Z., Sun, W., Wang, Y., Fu, Q., Zou, Y., & Mian, A. (2021). *Deep Learning based 3D Segmentation: A Survey*. arXiv. <https://doi.org/10.48550/arXiv.2103.05423>
- Herbst, M., Tappe, W., Kummer, S., & Vereecken, H. (2016). The impact of sieving on heterotrophic respiration response to water content in loamy and sandy topsoils. *Geoderma*, *272*, 73–82. <https://doi.org/10.1016/j.geoderma.2016.03.002>
- Herder, G. D., Van Isterdael, G., Beeckman, T., & De Smet, I. (2010). The roots of a new green revolution. *Trends in Plant Science*, *15*(11), 600–607. <https://doi.org/10.1016/j.tplants.2010.08.009>
- Hodge, A. (2004). The plastic plant: Root responses to heterogeneous supplies of nutrients. *New Phytologist*, *162*(1), 9–24. <https://doi.org/10.1111/j.1469-8137.2004.01015.x>
- Horn, J., Zhao, Y., Wandel, N., Landl, M., Schnepf, A., & Behnke, S. (2021). Robust Skeletonization for Plant Root Structure Reconstruction from MRI. *25th International*

- Conference on Pattern Recognition (ICPR)*, Milan, Italy, 10689-10696.
<https://doi.org/10.1109/ICPR48806.2021.9413045>
- Javaux, M., Schröder, T., Vanderborght, J., & Vereecken, H. (2008). Use of a Three-Dimensional Detailed Modeling Approach for Predicting Root Water Uptake. *Vadose Zone Journal*, 7(3), 1079–1088. <https://doi.org/10.2136/vzj2007.0115>
- Jiang, N., Floro, E., Bray, A. L., Laws, B., Duncan, K. E., & Topp, C. N. (2019). Three-Dimensional Time-Lapse Analysis Reveals Multiscale Relationships in Maize Root Systems with Contrasting Architectures. *The Plant Cell*, 31(8), 1708–1722. <https://doi.org/10.1105/tpc.19.00015>
- Jin, D., Iyer, K. S., Chen, C., Hoffman, E. A., & Saha, P. K. (2016). A robust and efficient curve skeletonization algorithm for tree-like objects using minimum cost paths. *Pattern Recognition Letters*, 76, 32–40. <https://doi.org/10.1016/j.patrec.2015.04.002>
- Jury, W. A., & Horton, R. (2004). *Soil Physics* (6th ed.). Wiley.
- Kamnitsas, K., Ledig, C., Newcombe, V. F. J., Simpson, J. P., Kane, A. D., Menon, D. K., Rueckert, D., & Glocker, B. (2017). Efficient multi-scale 3D CNN with fully connected CRF for accurate brain lesion segmentation. *Medical Image Analysis*, 36, 61–78. <https://doi.org/10.1016/j.media.2016.10.004>
- Kassambara, A. (2020). *ggpubr: “ggplot2” Based Publication Ready Plots*. R package version 0.6.0. <https://rpkgs.datanovia.com/ggpubr/>
- Kassambara, A. (2021). *rstatix: Pipe-Friendly Framework for Basic Statistical Tests*. R package version 0.7.2. <https://rpkgs.datanovia.com/rstatix/>
- Khare, D., Selzner, T., Leitner, D., Vanderborght, J., Vereecken, H., & Schnepf, A. (2022). Root System Scale Models Significantly Overestimate Root Water Uptake at Drying Soil Conditions. *Frontiers in Plant Science*, 13, Article 798741. <https://doi.org/10.3389/fpls.2022.798741>

- Koch, A., Meunier, F., Vanderborght, J., Garré, S., Pohlmeier, A., & Javaux, M. (2019). Functional–structural root-system model validation using a soil MRI experiment. *Journal of Experimental Botany*, *70*(10), 2797–2809. <https://doi.org/10.1093/jxb/erz060>
- Koch, T. (2022). Projection-based resolved interface 1D-3D mixed-dimension method for embedded tubular network systems. *Computers & Mathematics with Applications*, *109*, 15–29. <https://doi.org/10.1016/j.camwa.2022.01.021>
- Koch, T., Gläser, D., Weishaupt, K., Ackermann, S., Beck, M., Becker, B., Burbulla, S., Class, H., Coltman, E., Emmert, S., Fetzner, T., Grüninger, C., Heck, K., Hommel, J., Kurz, T., Lipp, M., Mohammadi, F., Scherrer, S., Schneider, M., ... Flemisch, B. (2021). DuMux 3 – an open-source simulator for solving flow and transport problems in porous media with a focus on model coupling. *Computers & Mathematics with Applications*, *81*, 423–443. <https://doi.org/10.1016/j.camwa.2020.02.012>
- Koch, T., Heck, K., Schröder, N., Class, H., & Helmig, R. (2018). A New Simulation Framework for Soil–Root Interaction, Evaporation, Root Growth, and Solute Transport. *Vadose Zone Journal*, *17*(1), Article 170210. <https://doi.org/10.2136/vzj2017.12.0210>
- Koch, T., Schneider, M., Helmig, R., & Jenny, P. (2020). Modeling tissue perfusion in terms of 1d-3d embedded mixed-dimension coupled problems with distributed sources. *Journal of Computational Physics*, *410*, Article 109370. <https://doi.org/10.1016/j.jcp.2020.109370>
- Koch, T., Wu, H., & Schneider, M. (2022). Nonlinear mixed-dimension model for embedded tubular networks with application to root water uptake. *Journal of Computational Physics*, *450*, Article 110823. <https://doi.org/10.1016/j.jcp.2021.110823>
- Koebnick, N., Huber, K., Kerkhofs, E., Vanderborght, J., Javaux, M., Vereecken, H., & Vetterlein, D. (2015). Unraveling the hydrodynamics of split root water uptake experiments using CT scanned root architectures and three dimensional flow simulations. *Frontiers in Plant Science*, *6*, 370. <https://doi.org/10.3389/fpls.2015.00370>

- Koepl, T., Vidotto, E., Wohlmuth, B., & Zunino, P. (2018). Mathematical modeling, analysis and numerical approximation of second-order elliptic problems with inclusions. *Mathematical Models and Methods in Applied Sciences*, 28(05), 953–978. <https://doi.org/10.1142/S0218202518500252>
- Koestel, J. (2018). SoilJ: An ImageJ Plugin for the Semiautomatic Processing of Three-Dimensional X-ray Images of Soils. *Vadose Zone Journal*, 17(1), Article 170062. <https://doi.org/10.2136/vzj2017.03.0062>
- Kramer, P. J. (1973). Forty Years of Research on Plant Water Relations. *Proceedings of the American Philosophical Society*, 117(5), 381–387.
- Kroener, E., Zarebanadkouki, M., Kaestner, A., & Carminati, A. (2014). Nonequilibrium water dynamics in the rhizosphere: How mucilage affects water flow in soils. *Water Resources Research*, 50(8), 6479–6495. <https://doi.org/10.1002/2013WR014756>
- Lal, R. (2009). Soil degradation as a reason for inadequate human nutrition. *Food Security*, 1, 45–57. <https://doi.org/10.1007/s12571-009-0009-z>
- Lal, R., Griffin, M., Apt, J., Lave, L., & Morgan, M. G. (2004). Managing Soil Carbon. *Science*, 304(5669), 393–393. <https://doi.org/10.1126/science.1093079>
- LaLonde, R., & Bagci, U. (2018). *Capsules for Object Segmentation*. arXiv. <https://doi.org/10.48550/arXiv.1804.04241>
- Landl, M., Phalempin, M., Schlüter, S., Vetterlein, D., Vanderborght, J., Kroener, E., & Schnepf, A. (2021). Modeling the Impact of Rhizosphere Bulk Density and Mucilage Gradients on Root Water Uptake. *Frontiers in Plant Science*, 3, Article 622367. <https://doi.org/10.3389/fagro.2021.622367>
- Landl, M., Schnepf, A., Vanderborght, J., Bengough, A. G., Bauke, S. L., Lobet, G., Bol, R., & Vereecken, H. (2018). Measuring root system traits of wheat in 2D images to parameterize 3D root architecture models. *Plant and Soil*, 425, 457–477. <https://doi.org/10.1007/s11104-018-3595-8>

- Latacz-Lohmann, U., & Hodge, I. D. (2003). European agri-environmental policy for the 21st century. *Australian Journal of Agricultural and Resource Economics*, 47, 123–139. <https://doi.org/10.22004/ag.econ.116179>
- Le, C., Zha, Y., Li, Y., Sun, D., Lu, H., & Yin, B. (2010). Eutrophication of lake waters in China: Cost, causes, and control. *Environmental Management*, 45(4), 662–668. <https://doi.org/10.1007/s00267-010-9440-3>
- Leitner, D., Meunier, F., Bodner, G., Javaux, M., & Schnepf, A. (2014). Impact of contrasted maize root traits at flowering on water stress tolerance – A simulation study. *Field Crops Research*, 165, 125–137. <https://doi.org/10.1016/j.fcr.2014.05.009>
- Lequeux, H., Hermans, C., Lutts, S., & Verbruggen, N. (2010). Response to copper excess in *Arabidopsis thaliana*: Impact on the root system architecture, hormone distribution, lignin accumulation and mineral profile. *Plant Physiology and Biochemistry*, 48(8), 673–682. <https://doi.org/10.1016/j.plaphy.2010.05.005>
- Linkohr, B. I., Williamson, L. C., Fitter, A. H., & Leyser, H. M. O. (2002). Nitrate and phosphate availability and distribution have different effects on root system architecture of *Arabidopsis*. *The Plant Journal*, 29(6), 751–760. <https://doi.org/10.1046/j.1365-313x.2002.01251.x>
- Lobet, G., Couvreur, V., Meunier, F., Javaux, M., & Draye, X. (2014). Plant Water Uptake in Drying Soils. *Plant Physiology*, 164(4), 1619–1627. <https://doi.org/10.1104/pp.113.233486>
- Lobet, G., Pound, M. P., Diener, J., Pradal, C., Draye, X., Godin, C., Javaux, M., Leitner, D., Meunier, F., Nacry, P., Pridmore, T. P., & Schnepf, A. (2015). Root System Markup Language: Toward a Unified Root Architecture Description Language. *Plant Physiology*, 167(3), 617–627. <https://doi.org/10.1104/pp.114.253625>
- Lundervold, A. S., & Lundervold, A. (2019). An overview of deep learning in medical imaging focusing on MRI. *Zeitschrift Für Medizinische Physik*, 29(2), 102–127. <https://doi.org/10.1016/j.zemedi.2018.11.002>

- Lynch, J. P. (1995). Root Architecture and Plant Productivity. *Plant Physiology*, *109*(1), 7–13. <https://doi.org/10.1104/pp.109.1.7>
- Lynch, J. P. (2013). Steep, cheap and deep: An ideotype to optimize water and N acquisition by maize root systems. *Annals of Botany*, *112*(2), 347–357. <https://doi.org/10.1093/aob/mcs293>
- Lynch, J. P. (2019). Root phenotypes for improved nutrient capture: An underexploited opportunity for global agriculture. *New Phytologist*, *223*(2), 548–564. <https://doi.org/10.1111/nph.15738>
- Lynch, J. P. (2022). Harnessing root architecture to address global challenges. *The Plant Journal: For Cell and Molecular Biology*, *109*(2), 415–431. <https://doi.org/10.1111/tpj.15560>
- Mai, T. H., Schnepf, A., Vereecken, H., & Vanderborght, J. (2019). Continuum multiscale model of root water and nutrient uptake from soil with explicit consideration of the 3D root architecture and the rhizosphere gradients. *Plant and Soil*, *439*, 273–292. <https://doi.org/10.1007/s11104-018-3890-4>
- Mairhofer, S., Zappala, S., Tracy, S. R., Sturrock, C., Bennett, M., Mooney, S. J., & Pridmore, T. (2012). RooTrak: Automated recovery of three-dimensional plant root architecture in soil from x-ray microcomputed tomography images using visual tracking. *Plant Physiology*, *158*(2), 561–569. <https://doi.org/10.1104/pp.111.186221>
- Malamy, J. E. (2005). Intrinsic and environmental response pathways that regulate root system architecture. *Plant, Cell & Environment*, *28*, 67–77. <https://doi.org/10.1111/j.1365-3040.2005.01306.x>
- Mathieu, L., Lobet, G., Tocquin, P., & Périlleux, C. (2015). “Rhizoponics”: A novel hydroponic rhizotron for root system analyses on mature *Arabidopsis thaliana* plants. *Plant Methods*, *11*, Article 3. <https://doi.org/10.1186/s13007-015-0046-x>

- Mawodza, T., Burca, G., Casson, S., & Menon, M. (2020). Wheat root system architecture and soil moisture distribution in an aggregated soil using neutron computed tomography. *Geoderma*, 359, Article 113988. <https://doi.org/10.1016/j.geoderma.2019.113988>
- McKay Fletcher, D. M., Ruiz, S., Dias, T., Petroselli, C., & Roose, T. (2020). Linking root structure to functionality: The impact of root system architecture on citrate-enhanced phosphate uptake. *New Phytologist*, 227(2), 376–391. <https://doi.org/10.1111/nph.16554>
- Menzel, M. I., Oros-Peusquens, A.-M., Pohlmeier, A., Shah, N. J., Schurr, U., & Schneider, H. U. (2007). Comparing ¹H-NMR imaging and relaxation mapping of German white asparagus from five different cultivation sites. *Journal of Plant Nutrition and Soil Science*, 170(1), 24–38. <https://doi.org/10.1002/jpln.200625114>
- Metselaar, K., & De Jong van Lier, Q. (2011). Scales in single root water uptake models: A review, analysis and synthesis. *European Journal of Soil Science*, 62, 657–665. <https://doi.org/10.1111/j.1365-2389.2011.01385.x>
- Metzner, R., Eggert, A., van Dusschoten, D., Pflugfelder, D., Gerth, S., Schurr, U., Uhlmann, N., & Jahnke, S. (2015). Direct comparison of MRI and X-ray CT technologies for 3D imaging of root systems in soil: Potential and challenges for root trait quantification. *Plant Methods*, 11, Article 17. <https://doi.org/10.1186/s13007-015-0060-z>
- Metzner, R., van Dusschoten, D., Bühler, J., Schurr, U., & Jahnke, S. (2014). Belowground plant development measured with magnetic resonance imaging (MRI): Exploiting the potential for non-invasive trait quantification using sugar beet as a proxy. *Frontiers in Plant Science*, 5, Article 469. <https://doi.org/10.3389/fpls.2014.00469>
- Meunier, F., Draye, X., Vanderborght, J., Javaux, M., & Couvreur, V. (2017). A hybrid analytical-numerical method for solving water flow equations in root hydraulic architectures. *Applied Mathematical Modelling*, 52, 648–663. <https://doi.org/10.1016/j.apm.2017.08.011>

- Meunier, F., Zarebanadkouki, M., Ahmed, M. A., Carminati, A., Couvreur, V., & Javaux, M. (2018). Hydraulic conductivity of soil-grown lupine and maize unbranched roots and maize root-shoot junctions. *Journal of Plant Physiology*, *227*, 31–44. <https://doi.org/10.1016/j.jplph.2017.12.019>
- Milletari, F., Navab, N., & Ahmadi, S.-A. (2016). V-Net: Fully Convolutional Neural Networks for Volumetric Medical Image Segmentation. *2016 Fourth International Conference on 3D Vision (3DV)*, 565–571. <https://doi.org/10.1109/3DV.2016.79>
- Montgomery, D. R. (2007). Soil erosion and agricultural sustainability. *Proceedings of the National Academy of Sciences*, *104*(33), 13268–13272. <https://doi.org/10.1073/pnas.0611508104>
- Mooney, S. J., Pridmore, T. P., Helliwell, J., & Bennett, M. J. (2012). Developing X-ray Computed Tomography to non-invasively image 3-D root systems architecture in soil. *Plant and Soil*, *352*, 1–22. <https://doi.org/10.1007/s11104-011-1039-9>
- Mualem, Y. (1976). A new model for predicting the hydraulic conductivity of unsaturated porous media. *Water Resources Research*, *12*(3), 513–522. <https://doi.org/10.1029/WR012i003p00513>
- Nagel, K., Putz, A., Gilmer, F., Kathrin, H., Fischbach, A., Pfeifer, J., Marc, F., Blossfeld, S., Michaela, E., Dimaki, C., Bernd, K., Ann-Katrin, K., Anna, G., Scharr, H., Fiorani, F., & Ulrich, S. (2012). GROWSCREEN-Rhizo is a novel phenotyping robot enabling simultaneous measurements of root and shoot growth for plants grown in soil-filled rhizotrons. *Functional Plant Biology*, *39*(11), 891–905. <https://doi.org/10.1071/FP12023>
- Newman, E. I. (1969). Resistance to Water Flow in Soil and Plant. I. Soil Resistance in Relation to Amounts of Root: Theoretical Estimates. *Journal of Applied Ecology*, *6*(1), 1–12. <https://doi.org/10.2307/2401297>

- North, G. B., & Nobel, P. S. (1996). Radial hydraulic conductivity of individual root tissues of *Opuntia ficus-indica* (L.) Miller as soil moisture varies. *Annals of Botany*, 77(2), 133–142. <https://doi.org/10.1006/anbo.1996.0015>.
- Nye, P. H., & Marriott, F. H. C. (1969). A theoretical study of the distribution of substances around roots resulting from simultaneous diffusion and mass flow. *Plant and Soil*, 30, 459–472. <https://doi.org/10.1007/BF01881971>
- Osmont, K. S., Sibout, R., & Hardtke, C. S. (2007). Hidden Branches: Developments in Root System Architecture. *Annual Review of Plant Biology*, 58, 93–113. <https://doi.org/10.1146/annurev.arplant.58.032806.104006>
- Passioura, J. B. (1988). Water Transport in and to Roots. *Annual Review of Plant Physiology and Plant Molecular Biology*, 39, 245–265. <https://doi.org/10.1146/annurev.pp.39.060188.001333>
- Passot, S., Couvreur, V., Meunier, F., Draye, X., Javaux, M., Leitner, D., Pagès, L., Schnepf, A., Vanderborght, J., & Lobet, G. (2019). Connecting the dots between computational tools to analyse soil–root water relations. *Journal of Experimental Botany*, 70(9), 2345–2357. <https://doi.org/10.1093/jxb/ery361>
- Patel, R. (2013). The Long Green Revolution. *Journal of Peasant Studies*, 40(1), 1–63. <https://doi.org/10.1080/03066150.2012.719224>
- Pflugfelder, D., Kochs, J., Koller, R., Jahnke, S., Mohl, C., Pariyar, S., Fassbender, H., Nagel, K. A., Watt, M., & van Dusschoten, D. (2021). The root system architecture of wheat establishing in soil is associated with varying elongation rates of seminal roots: Quantification using 4D magnetic resonance imaging. *Journal of Experimental Botany*, 73(7), 2050–2060. <https://doi.org/10.1093/jxb/erab551>
- Pflugfelder, D., Metzner, R., Dusschoten, D., Reichel, R., Jahnke, S., & Koller, R. (2017). Non-invasive imaging of plant roots in different soils using magnetic resonance imaging (MRI). *Plant Methods*, 13, Article 102. <https://doi.org/10.1186/s13007-017-0252-9>

- Phalempin, M., Lippold, E., Vetterlein, D., & Schlüter, S. (2021). An improved method for the segmentation of roots from X-ray computed tomography 3D images: Routine v.2. *Plant Methods*, *17*, Article 39. <https://doi.org/10.1186/s13007-021-00735-4>
- Pingali, P. L. (2012). Green Revolution: Impacts, limits, and the path ahead. *Proceedings of the National Academy of Sciences*, *109*(31), 12302–12308. <https://doi.org/10.1073/pnas.0912953109>
- Plenge, E., Poot, D. H., Bernsen, M., Kotek, G., Houston, G., Wielopolski, P., van der Weerd, L., Niessen, W. J., & Meijering, E. (2012). Super-resolution methods in MRI: Can they improve the trade-off between resolution, signal-to-noise ratio, and acquisition time? *Magnetic Resonance in Medicine*, *68*(6), 1983–1993.
- Pohlmeier, A., Garré, S., & Roose, T. (2018). Noninvasive Imaging of Processes in Natural Porous Media: From Pore to Field Scale. *Vadose Zone Journal*, *17*(1), Article 180044. <https://doi.org/10.2136/vzj2018.03.0044>
- Pohlmeier, A., Haber-Pohlmeier, S., Javaux, M., & Vereecken, H. (2013). Magnetic Resonance Imaging Techniques for Visualization of Root Growth and Root Water Uptake Processes. In S. H. Anderson & J. W. Hopmans (Eds.), *Soil–Water–Root Processes: Advances in Tomography and Imaging* (pp. 137–156). John Wiley & Sons, Ltd. <https://doi.org/10.2136/sssaspecpub61.c7>
- Pohlmeier, A., Haber-Pohlmeier, S., & Stapf, S. (2009). A Fast Field Cycling Nuclear Magnetic Resonance Relaxometry Study of Natural Soils. *Vadose Zone Journal*, *8*(3), 735–742. <https://doi.org/10.2136/vzj2008.0030>
- Postma, J. A., Kuppe, C., Owen, M. R., Mellor, N., Griffiths, M., Bennett, M. J., Lynch, J. P., & Watt, M. (2017). OpenSimRoot: Widening the scope and application of root architectural models. *New Phytologist*, *215*(3), 1274–1286. <https://doi.org/10.1111/nph.14641>

- Postma, J. A., & Lynch, J. P. (2011). Root Cortical Aerenchyma Enhances the Growth of Maize on Soils with Suboptimal Availability of Nitrogen, Phosphorus, and Potassium. *Plant Physiology*, *156*(3), 1190–1201. <https://doi.org/10.1104/pp.111.175489>
- Postma, J. A., & Lynch, J. P. (2012). Complementarity in root architecture for nutrient uptake in ancient maize/bean and maize/bean/squash polycultures. *Annals of Botany*, *110*(2), 521–534. <https://doi.org/10.1093/aob/mcs082>
- R Core Team. (2022). *R: A Language and Environment for Statistical Computing*. R Foundation for Statistical Computing, Vienna, Austria. <https://www.R-project.org/>
- Rascher, U. S., Fiorani, F., Jahnke, S., Jansen, M., Kuhn, A., Matsubara, S., Martin, L., Merchant, A., Metzner, R., Müller-Linow, M., Nagel, K., Pieruschka, R., Pinto, F., Kuchendorf, C., Temperton, V., Thorpe, M., Dusschoten, D., Van Volkenburgh, E., & Schurr, U. (2011). Non-invasive approaches for phenotyping of enhanced performance traits in bean. *Functional Plant Biology*, *38*(12), 968–983. <https://doi.org/10.1071/FP11164>
- Reay, D., Davidson, E., Smith, K., Smith, P., Melillo, J., Dentener, F., & Crutzen, P. (2012). Global agriculture and nitrous oxide emissions. *Nature Climate Change*, *2*, 410–416. <https://doi.org/10.1038/nclimate1458>
- Rellán-Álvarez, R., Lobet, G., & Dinneny, J. R. (2016). Environmental Control of Root System Biology. *Annual Review of Plant Biology*, *67*(1), 619–642. <https://doi.org/10.1146/annurev-arplant-043015-111848>
- Rich, S. M., Christopher, J., Richards, R., & Watt, M. (2020). Root phenotypes of young wheat plants grown in controlled environments show inconsistent correlation with mature root traits in the field. *Journal of Experimental Botany*, *71*(16), 4751–4762. <https://doi.org/10.1093/jxb/eraa201>
- Richards, L. A. (1931). Capillary conduction of liquids through porous mediums. *Physics*, *1*(5), 318–333. <https://doi.org/10.1063/1.1745010>

- Rodriguez-Dominguez, C. M., & Brodribb, T. J. (2020). Declining root water transport drives stomatal closure in olive under moderate water stress. *New Phytologist*, 225, 126–134. <https://doi.org/10.1111/nph.16177>
- Ronneberger, O., Fischer, P., & Brox, T. (2015). *U-Net: Convolutional Networks for Biomedical Image Segmentation*. arXiv. <https://doi.org/10.48550/arXiv.1505.04597>
- Roose, T., & Fowler, A. (2004). A mathematical model for water and nutrient uptake by plant root systems. *Journal of Theoretical Biology*, 228(2), 173–184. <https://doi.org/10.1016/j.jtbi.2003.12.013>
- Roose, T., Fowler, A. C., & Darrah, P. R. (2001). A mathematical model of plant nutrient uptake. *Journal of Mathematical Biology*, 42(4), 347–360. <https://doi.org/10.1007/s002850000075>
- RStudio Team. (2022). *RStudio: Integrated Development Environment for R*. RStudio, Inc., Boston, MA. <http://www.rstudio.com/>
- Rudolph-Mohr, N., Bereswill, S., Tötze, C., Kardjilov, N., & Oswald, S. E. (2021). Neutron computed laminography yields 3D root system architecture and complements investigations of spatiotemporal rhizosphere patterns. *Plant and Soil*, 469, 489–501. <https://doi.org/10.1007/s11104-021-05120-7>
- Schindelin, J., Arganda-Carreras, I., Frise, E., Kaynig, V., Longair, M., Pietzsch, T., Preibisch, S., Rueden, C., Saalfeld, S., Schmid, B., Tinevez, J.-Y., White, D., Hartenstein, V., Eliceiri, K., Tomancak, P., & Cardona, A. (2012). Fiji: An Open-Source Platform for Biological-Image Analysis. *Nature Methods*, 9, 676–682. <https://doi.org/10.1038/nmeth.2019>
- Schlömer, N. (2022). *pygmsh: A Python frontend for Gmsh (v7.1.15)*. <https://doi.org/10.5281/zenodo.5886856>

- Schmidhuber, J., & Tubiello, F. N. (2007). Global food security under climate change. *Proceedings of the National Academy of Sciences*, *104*(50), 19703–19708. <https://doi.org/10.1073/pnas.0701976104>
- Schneider, H. M., & Lynch, J. P. (2020). Should Root Plasticity Be a Crop Breeding Target? *Frontiers in Plant Science*, *11*, Article 546. <https://doi.org/10.3389/fpls.2020.00546>
- Schnepf, A., Black, C. K., Couvreur, V., Delory, B. M., Doussan, C., Heymans, A., Javaux, M., Khare, D., Koch, A., Koch, T., Kuppe, C. W., Landl, M., Leitner, D., Lobet, G., Meunier, F., Postma, J. A., Schäfer, E. D., Selzner, T., Vanderborght, J., & Vereecken, H. (2023). Collaborative benchmarking of functional-structural root architecture models: Quantitative comparison of simulated root water uptake. *In Silico Plants*, *5*(1), Article diad005. <https://doi.org/10.1093/insilicoplants/diad005>
- Schnepf, A., Black, C. K., Couvreur, V., Delory, B. M., Doussan, C., Koch, A., Koch, T., Javaux, M., Landl, M., Leitner, D., Lobet, G., Mai, T. H., Meunier, F., Petrich, L., Postma, J. A., Priesack, E., Schmidt, V., Vanderborght, J., Vereecken, H., & Weber, M. (2020). Call for Participation: Collaborative Benchmarking of Functional-Structural Root Architecture Models. The Case of Root Water Uptake. *Frontiers in Plant Science*, *11*, Article 316. <https://doi.org/10.3389/fpls.2020.00316>
- Schnepf, A., Huber, K., Landl, M., Meunier, F., Petrich, L., & Schmidt, V. (2018a). Statistical Characterization of the Root System Architecture Model CRootBox. *Vadose Zone Journal*, *17*(1), Article 170212. <https://doi.org/10.2136/vzj2017.12.0212>
- Schnepf, A., Leitner, D., Landl, M., Lobet, G., Mai, T. H., Morandage, S., Sheng, C., Zörner, M., Vanderborght, J., & Vereecken, H. (2018b). CRootBox: A structural–functional modelling framework for root systems. *Annals of Botany*, *121*(5), 1033–1053. <https://doi.org/10.1093/aob/mcx221>
- Schröder, T., Javaux, M., Vanderborght, J., Körfgen, B., & Vereecken, H. (2008). Effect of Local Soil Hydraulic Conductivity Drop Using a Three-Dimensional Root Water

- Uptake Model. *Vadose Zone Journal*, 7(3), 1089–1098. <https://doi.org/10.2136/vzj2007.0114>
- Schröder, T., Javaux, M., Vanderborght, J., Körfgen, B., & Vereecken, H. (2009a). Implementation of a Microscopic Soil–Root Hydraulic Conductivity Drop Function in a Three-Dimensional Soil–Root Architecture Water Transfer Model. *Vadose Zone Journal*, 8(3), 783–792. <https://doi.org/10.2136/vzj2008.0116>
- Schröder, T., Tang, L., Javaux, M., Vanderborght, J., Körfgen, B., & Vereecken, H. (2009b). A grid refinement approach for a three-dimensional soil-root water transfer model. *Water Resources Research*, 45(10), Article W10412. <https://doi.org/10.1029/2009WR007873>
- Schulz, H., Postma, J. A., van Dusschoten, D., Scharr, H., & Behnke, S. (2013). Plant Root System Analysis from MRI Images. In G. Csurka, M. Kraus, R. S. Laramée, P. Richard, & J. Braz (Eds.), *Computer Vision, Imaging and Computer Graphics. Theory and Application. Communications in Computer and Information Science* (pp. 411–425). Springer, Berlin, Heidelberg. https://doi.org/10.1007/978-3-642-38241-3_28
- Selzner, T., Horn, J., Landl, M., Pohlmeier, A., Helmrich, D., Huber, K., Vanderborght, J., Vereecken, H., Behnke, S., & Schnepf, A. (2023). 3D U-Net Segmentation Improves Root System Reconstruction from 3D MRI Images in Automated and Manual Virtual Reality Work Flows. *Plant Phenomics*, 5, Article 0076. <https://doi.org/10.34133/plantphenomics.0076>
- Smith, A. G., Petersen, J., Selvan, R., & Rasmussen, C. R. (2020). Segmentation of roots in soil with U-Net. *Plant Methods*, 16, Article 13. <https://doi.org/10.1186/s13007-020-0563-0>
- Smith, A. G., Petersen, J., Terrones-Campos, C., Berthelsen, A. K., Forbes, N. J., Darkner, S., Specht, L., & Vogelius, I. R. (2022). RootPainter3D: Interactive-machine-learning enables rapid and accurate contouring for radiotherapy. *Medical Physics*, 49(1), 461–473. <https://doi.org/10.1002/mp.15353>

- Soltaninejad, M., Sturrock, C. J., Griffiths, M., Pridmore, T. P., & Pound, M. P. (2020). Three Dimensional Root CT Segmentation Using Multi-Resolution Encoder-Decoder Networks. *IEEE Transactions on Image Processing*, *29*, 6667–6679. <https://doi.org/10.1109/TIP.2020.2992893>
- Stingaciu, L., Schulz, H., Pohlmeier, A., Behnke, S., Zilken, H., Javaux, M., & Vereecken, H. (2013). In Situ Root System Architecture Extraction from Magnetic Resonance Imaging for Water Uptake Modeling. *Vadose Zone Journal*, *12*(1), Article vzj2012.0019. <https://doi.org/10.2136/vzj2012.0019>
- Taiz, L., & Zeiger, E. (2010). *Plant physiology and development* (5th ed.). Sinauer Associates.
- Teramoto, S., Takayasu, S., Kitomi, Y., Arai-Sanoh, Y., Tanabata, T., & Uga, Y. (2020). High-throughput three-dimensional visualization of root system architecture of rice using X-ray computed tomography. *Plant Methods*, *16*, Article 66. <https://doi.org/10.1186/s13007-020-00612-6>
- Tilman, D., Balzer, C., Hill, J., & Befort, B. L. (2011). Global food demand and the sustainable intensification of agriculture. *Proceedings of the National Academy of Sciences*, *108*(50), 20260–20264. <https://doi.org/10.1073/pnas.1116437108>
- Tötze, C., Kardjilov, N., Hilger, A., Rudolph-Mohr, N., Manke, I., & Oswald, S. E. (2021). Three-dimensional in vivo analysis of water uptake and translocation in maize roots by fast neutron tomography. *Scientific Reports*, *11*, Article 10578. <https://doi.org/10.1038/s41598-021-90062-4>
- Trachsel, S., Kaeppler, S. M., Brown, K. M., & Lynch, J. P. (2011). Shovelomics: High throughput phenotyping of maize (*Zea mays* L.) root architecture in the field. *Plant and Soil*, *341*, 75–87. <https://doi.org/10.1007/s11104-010-0623-8>
- Tracy, S. R., Black, C. R., Roberts, J. A., Sturrock, C., Mairhofer, S., Craigan, J., & Mooney, S. J. (2012). Quantifying the impact of soil compaction on root system architecture in tomato (*Solanum lycopersicum*) by X-ray micro-computed tomography. *Annals of Botany*, *110*(2), 511–519. <https://doi.org/10.1093/aob/mcs031>

- UN. (2015). *Transforming our world: The 2030 Agenda for Sustainable Development*. <https://wedocs.unep.org/xmlui/handle/20.500.11822/9814>
- Uzman, A. O., Horn, J., & Behnke, S. (2019). Learning Super-resolution 3D Segmentation of Plant Root MRI Images from Few Examples. *27th European Symposium on Artificial Neural Networks, Computational Intelligence and Machine Learning (ESANN)*, Bruges, Belgium. <https://doi.org/10.48550/arXiv.1903.06855>
- Vaccari, D. A. (2009). Phosphorus: A Looming Crisis. *Scientific American*, *300*(6), 54–59. <https://doi.org/10.1038/scientificamerican0609-54>
- van Dusschoten, D., Metzner, R., Kochs, J., Postma, J. A., Pflugfelder, D., Bühler, J., Schurr, U., & Jahnke, S. (2016). Quantitative 3D Analysis of Plant Roots Growing in Soil Using Magnetic Resonance Imaging. *Plant Physiology*, *170*(3), 1176–1188. <https://doi.org/10.1104/pp.15.01388>
- van Genuchten, M. T. (1980). A Closed-form Equation for Predicting the Hydraulic Conductivity of Unsaturated Soils. *Soil Science Society of America Journal*, *44*(5), 892–898. <https://doi.org/10.2136/sssaj1980.03615995004400050002x>
- Vicente-Serrano, S. M., McVicar, T. R., Miralles, D. G., Yang, Y., & Tomas-Burguera, M. (2020). Unraveling the influence of atmospheric evaporative demand on drought and its response to climate change. *WIREs Climate Change*, *11*(2), Article e632. <https://doi.org/10.1002/wcc.632>
- Ward, M. H., Jones, R. R., Brender, J. D., de Kok, T. M., Weyer, P. J., Nolan, B. T., Villanueva, C. M., & van Breda, S. G. (2018). Drinking Water Nitrate and Human Health: An Updated Review. *International Journal of Environmental Research and Public Health*, *15*(7), Article 1557. <https://doi.org/10.3390/ijerph15071557>
- Wei, G., Schlüter, S., Blaser, S., Shen, J., & Vetterlein, D. (2019). A shape-based method for automatic and rapid segmentation of roots in soil from X-ray computed tomography images: Routine. *Plant and Soil*, *441*, 643–655. <https://doi.org/10.1007/s11104-019-04053-6>

- Zappala, S., Mairhofer, S., Tracy, S., Sturrock, C. J., Bennett, M., Pridmore, T., & Mooney, S. J. (2013). Quantifying the effect of soil moisture content on segmenting root system architecture in X-ray computed tomography images. *Plant and Soil*, *370*, 35–45. <https://doi.org/10.1007/s11104-013-1596-1>
- Zarebanadkouki, M., Kim, Y. X., & Carminati, A. (2013). Where do roots take up water? Neutron radiography of water flow into the roots of transpiring plants growing in soil. *New Phytologist*, *199*(4), 1034–1044. <https://doi.org/10.1111/nph.12330>
- Zarebanadkouki, M., Meunier, F., Couvreur, V., Cesar, J., Javaux, M., & Carminati, A. (2016). Estimation of the hydraulic conductivities of lupine roots by inverse modelling of high-resolution measurements of root water uptake. *Annals of Botany*, *118*(4), 853–864. <https://doi.org/10.1093/aob/mcw154>
- Zhao, Y., Schnepf, A., Landl, M., Wandel, N., & Behnke, S. (2020). Segmentation of Plant Root MRI Images With 3D U-Net. *27th European Symposium on Artificial Neural Networks, Computational Intelligence and Machine Learning (ESANN)*, Bruges, Belgium. <https://arxiv.org/abs/2002.09317>
- Zhou, X.-R., Schnepf, A., Vanderborght, J., Leitner, D., Lacoïnte, A., Vereecken, H., & Lobet, G. (2020). CPlantBox, a whole-plant modelling framework for the simulation of water- and carbon-related processes. *In Silico Plants*, *2*(1), Article diaa001. <https://doi.org/10.1093/insilicoplants/diaa001>